Numerical Modeling of the Effects of a Free Surface on the Operating Characteristics of Marine Hydrokinetic Turbines

Samantha Jane Adamski

A thesis submitted in partial fulfillment
of the requirements for the degree of

Master of Science in Mechanical Engineering

University of Washington

2013

Committee:

Alberto Aliseda

Brian Polagye

James J. Riley

Program Authorized to Offer Degree:

Mechanical Engineering

University of Washington

Abstract

Numerical Modeling of the Effects of a Free Surface on the Operating Characteristics of Marine Hydrokinetic Turbines

Samantha Jane Adamski

:

Marine Hydrokinetic (MHK) turbines are a growing area of research in the renewable energy field because tidal currents are a highly predictable clean energy source. The presence of a free surface may influence the flow around the turbine and in the wake, critically affecting turbine performance and environmental effects through modification of the wake physical variables. The characteristic Froude number that control these processes is still a matter of controversy, with the channel depth, the turbine's hub depth, the blade tip depth and the turbine diameter as potential candidates for a length scale. We use a Reynolds Averaged Navier Stokes (RANS) simulation with a Blade Element Theory (BET) model of the turbine and with a Volume of Fluid model, which is used to track the free surface dynamics, to understand the physics of the wake-free surface interactions. Pressure and flow rate boundary conditions for a channel's inlet, outlet and air side have been tested in an effort to determine the optimum set of simulation conditions for MHK turbines in rivers or shallow estuaries. Stability and accuracy in terms of power extraction and kinetic and potential energy budgets are considered. The goal of this research is to determine, quantitatively in non-dimensional parameter space, the limit between negligible and significant free surface effects on MHK turbine analysis.

TABLE OF CONTENTS

LIST OF FIGURES

LIST OF TABLES

ACKNOWLEDGMENTS

I am very grateful to my advisor, Professor Alberto Aliseda. He provided excellent guidance and unyielding encouragement throughout all of my endeavors at the University of Washington. I am also very thankful to Professor Brian Polagye and Professor James Riley for teaching me about tidal energy and turbulent flows. They provided me with invaluable knowledge in pursuit of my research goals. This work would not have been possible without support from the Department of Energy through the Northwest National Marine Renewable Energy Center as well as the faculty and staff members of the University of Washington Mechanical Engineering Department. I am also sincerely grateful for the love and support my husband has provided throughout my time at the University of Washington. Last but not least, I would like to thank my family and friends for their unwaivering support and for always encouraging me to challenge myself.

Chapter 1

INTRODUCTION

1.1 Energy Requirements

The availability and cost of energy is a concern for many people in the world today. The United States' average energy expenditure per capita in 2009 was $3,460, this figure includes all energy expenditures by residential, commercial, industrial, and transportation sectors [4]. Furthermore, the United States consumed 99.27 quadrillion Btu of energy in 2008 [5]. Both of these numbers are growing.

In 2011, 82% of the energy consumed by the U.S. was from fossil fuels [6]. However, the reserves of fossil fuels are being depleted and there is no accurate way to determine how much remains. Fossil fuels are also known to have harmful effects on the environment. For example, they release greenhouse gases, such as Carbon Dioxide, into the air when they are consumed to produce energy. Hence, there is a large demand for clean renewable energy sources. And since people are already paying a significant amount of money for energy, any alternative energy source must also be able to compete financially with current sources of energy.

There are many alternatives to fossil fuels currently in use today, such as wind power, solar power, hydro-electric power, and nuclear power. Unfortunately, some of these alternatives can also have a negative impact on the environment and others do not provided a predictable amount of energy. The dams required for hydro-electric power often result in significant changes to the river where the dam is located. These changes affect the habitat for many of the species indigenous to the river. Nuclear power creates spent fuel rods which require special disposal due to their high levels of

radioactivity. Even though wind and solar energy may not have a significant impact on the environment, they do not provide a predictable energy source because they rely on the weather, which is constantly changing, to produce power. Tides on the other hand are much more predictable.

1.2 Tidal Energy

1.2.1 Tidal Physics

Oceans cover over 70% of the earth's surface and contain a large amount of thermal, kinetic, chemical, and biological energy [7]. Tidal currents, for example, contain kinetic energy. The energy in tidal flows comes directly from the gravitational interaction of the moon and the sun with earth's oceans [8]. The gravitational force is equal to

$$F = G\frac{m_1 m_2}{r^2} \tag{1.1}$$

where F is the gravitational force between the two different masses, m_1 and m_2, r is the distance between the center of the two masses, and G is the gravitational constant, which is equal to $6.67 \times 10^{-11}\frac{Nm^2}{kg^2}$. Even though the sun's mass is much larger than that of the moon, the close proximity of the moon to the earth makes the moon's gravitational force stronger, accounting for 70% of tidal behavior [9]. The gravitational pull of the sun helps dictate the magnitude of the high and low tides created by the moon. If the sun, moon, and Earth are aligned, the gravitation forces act in the same direction, this is called spring tide and it has a tidal range that is greater than the average tidal range, see Figure 1.1 [9]. If the sun, moon, and Earth create a right angle, the gravitational forces from the sun and the moon act perpendicularly to each other, decreasing the magnitude of the tidal range such that it is less than the average, this is called neap tide, see Figure 1.1.

Due to the predictability of celestial mechanics, the gravitational forces as well as

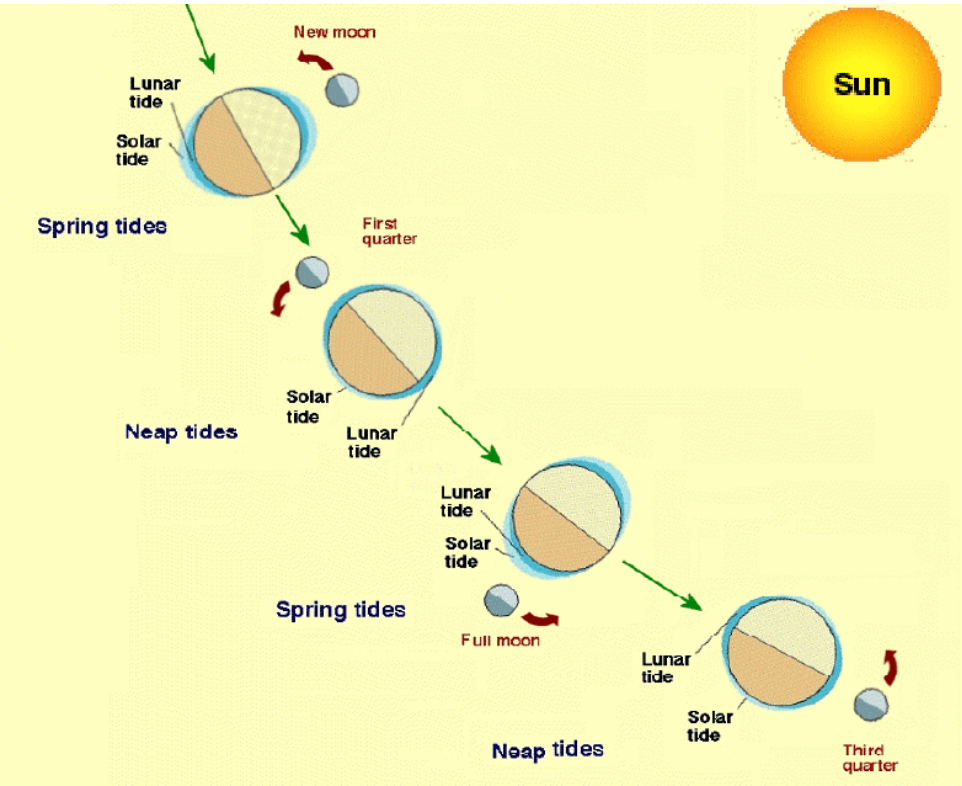

Figure 1.1: Moon Phases Causing Spring and Neap Tides [10]

the tides are also predictable. The magnitude of the tidal elevation and the speed of the tidal current in a geographical region depend heavily on the bathymetry of the sea floor. In some locations the coastal and seabed conditions result in a large tidal range ideal for tidal barrages and in other locations the coastal and seabed conditions result in an acceleration of the tidal flow creating a fast moving, bi-directional current, perfect for Marine Hydrokinetic (MHK) turbines[11].

1.2.2 Tidal Barrages

The rise and fall of the tides has been used to generate energy for hundreds of years. For over 900 years the Eling Tide Mill, in the United Kingdoms, has been using tidal power to mill wheat and produce flour. The currently operating tidal barrages use

the same basic principle as the Eling Tide Mill. By storing water behind a dam at high tide the tidal barrage creates a head difference as the water recedes to the low tide level. The water stored behind the dam is then released through hydroelectric turbines (a water wheel in the case of the flour mill) extracting energy from the flowing water, see Figure 1.2 [10]. The largest energy-producing tidal barrage is a 240 MW tidal barrage in France, on the La Rance River estuary [10]. Currently there are only three sites using tidal barrages due to the high capital cost and the environmental impacts associated with this technology [8]. It has been suggested that extracting energy from the kinetic energy of the flow instead of the tidal head loss could potentially have significantly less environmental impact [12].

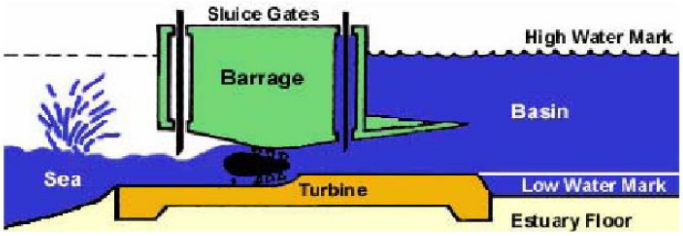

Figure 1.2: Tidal Barrage [7]

1.2.3 Marine Hydrokinetic Turbines

The principle behind MHK Turbines is to convert the kinetic energy in tidal currents into mechanical energy by driving a generator to produce power [7]. There are two primary types of MHK turbines, axial flow (also known as horizontal axis) turbines and cross flow (also known as vertical axis) turbines, see Figure 1.3. The axis of rotation for a horizontal axis turbine is parallel to the direction of the free stream flow whereas the axis of rotation for a vertical axis turbine is perpendicular to the direction of the free stream flow.

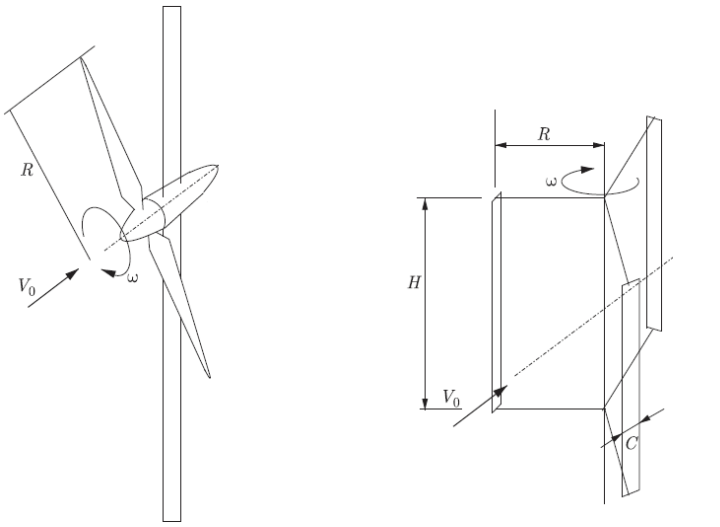

Figure 1.3: Horizontal Axis versus Vertical Axis Turbines [12]

The wind energy industry has determined through years of research that horizontal axis turbines are the most effective mechanism for extracting energy from the wind at large scale because the turbines can self-start and have a better efficiency than cross flow turbines [12]. Many of the same theories and models developed for horizontal axis wind turbines can be applied to modeling horizontal axis MHK turbines.

In the marine renewable energy industry there is no consensus on the leading technology for utility scale energy extraction. While the higher efficiency of horizontal axis turbine still gives them an advantage, there are however, several problems faced by horizontal axis turbines that present an opportunity for cross flow turbines to compete in the MHK field:

- The high tip speed ratios required for high efficiency can cause cavitation to occur

- Multiple turbines cannot share the same electrical converter [12]

- In order to extract the maximum amount of power from a bi-direction tidal flow the turbine either needs to have symmetric blades, leading to lower efficiency, or the turbine must be able to rotate about a vertical axis so that the turbine is always aligned with the flow

Even though vertical axis turbines have been shown to be suboptimal for utility scale wind turbines, the differences between wind and tidal currents make vertical axis turbines a plausible option for the tidal energy field. In tidal currents, the flow will always be perpendicular to the axis of rotation for vertical axis turbines allowing them to operate with flow from any direction. Another benefit of using a vertical axis turbine is they are well suited for use in turbine farms because they can be placed relatively close to one another and if stacked vertically in a tower they only required one generator [12]. There are several different blade designs for vertical axis turbines. The two major designs are the classic Darrieus Turbine seen in Figure 1.3b and the helical blade shaped turbine seen in Figure 1.4. The Darrieus Turbine suffers from variable loading, whereas the helical shaped blades lead to an almost constant loading, which can significantly extend the life of the turbine [12].

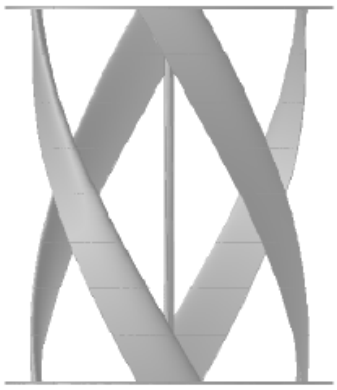

Figure 1.4: Helical blade shaped turbine [9]

1.2.4 Current Deployments

Some MHK turbines currently in use today are the Seagen, the Open-Centre Turbine, the HS300, and the Turbine Generator Unit.

The Seagen is a 1.2 MW horizontal axis turbine developed by Marine Current Turbines Ltd based in the United Kingdom. A Seagen is currently operating in an estuary in Northern Ireland and is connected to the grid. It has two 16 meter diameter horizontal axis turbines that are connected by arms to a support pile, see Figure 1.5. Each turbine has its own power train. The support piling projects above the surface of the water so that the rotors and power trains can be raised out of the water for maintenance and repairs [7]. On January 18th 2009, the device successfully operated at full power for the first time [7].

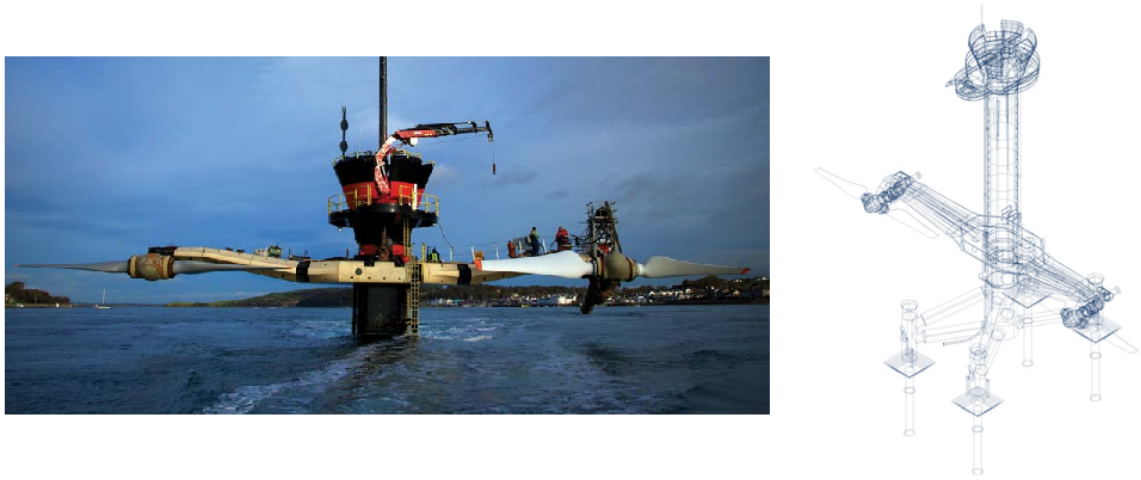

Figure 1.5: Seagen developed by Marine Current Turbine Ltd. [13]

The Open-Centre Turbine was developed by Open-Hydro Ltd, based in Ireland. The test turbine designed by Open-Hydro consists of a 6 meter diameter rotor, a stator, a duct, and a generator [14]. In 2006, an Open-Centre Turbine was installed at the European Marine Energy Centre (EMEC). It used a twin-piled support structure that

allowed the turbine to be raised and lowered for testing purposes, see Figure 1.6a. The commercial deployments of the turbine will be mounted to the seafloor and will not have any surface penetration, see Figure 1.6b.

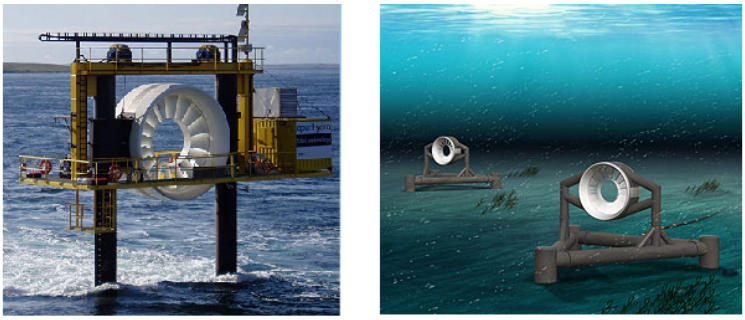

a) EMECs twin-piled test structure

b) Seabed mounted Open Centre Turbine

Figure 1.6: Open Centre Turbine developed by Open-Hydro Ltd. [15]

The HS300 was developed by Andritz Hydro Hammerfest, based in Norway. It is a three bladed horizontal axis turbine. The HS300 is a 300kW prototype that has been tested at a depth of 50 meters in Finnmark, Norway. The turbine successfully completed a full cycle which included deployment, operation, retrieval, maintenance and redeployment. The pre-commercial demonstrator, the HS1000, is a scaled up version of the HS300 and is rated for 1 MW. It is currently deployed at the EMEC tidal test site, where it has successfully provided power to the grid [16]. Andritz Hydro Hammerfest is planning to install an array of turbines in the Sound of Islay, see Figure 1.7

Ocean Renewable Power Company (ORPC) has developed the "Turbine Generator Unit" (TGU). The TGU is a modular cross flow turbine, see Figure 1.8. These cross flow turbines use the same principle as vertical axis turbines, where flow is perpendicular to the axis of rotation. The axis of rotation for TGU's, however, is parallel to the seabed instead of vertical. The turbines are secured to the bottom

Figure 1.7: An artist's rendition of the HS300 and HS1000 developed by Andritz Hydro Hammerfest [16]

of the seafloor using a bottom support frame. In 2008, ORPC tested the TGU in Cobscook Bay, Maine and it was a technical success. In 2010, they tested a pre-commercial model of the TGU [17] and in 2012 installed the first commercial TideGen system at the same location.

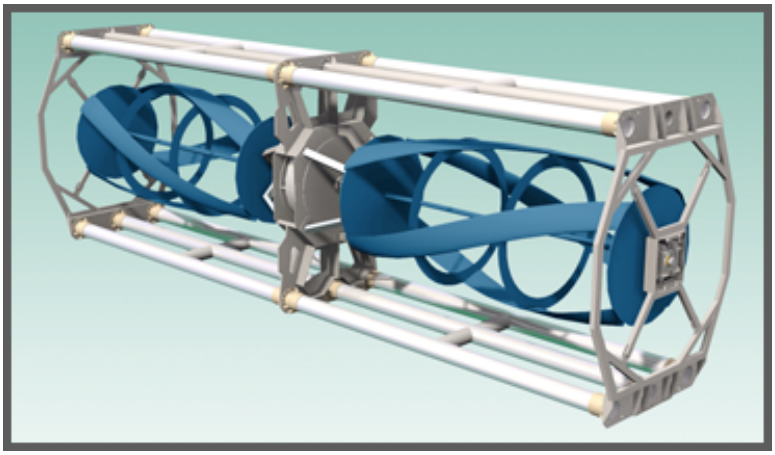

Figure 1.8: Tidal Generating Unit developed by Ocean Renewable Power Company [17]

1.3 Wind Energy Versus Tidal Energy

In many ways, MHK turbines and wind turbines behave very similarly. Thus, many of the same methods used to model wind turbines can be applied to MHK turbines. Some of these methods, e.g. the Actuator Disc Model, the Blade Element Model, and the Single Reference Frame model, are discussed in detail in Section 2.2. There are several key differences between wind energy and tidal energy that must be taken into consideration when modeling MHK turbines. One such difference, which is the focus of this thesis, is the presence of a free surface because the fluid domain from which MHK turbines extract energy is bounded by the interface between water and air.

1.3.1 Importance of the Free Surface

The free surface produces a significant difference between wind energy and tidal energy because the flow can no longer be assumed to be unconfined. The confinement associated with the presence of the free surface and the sea floor introduces a new parameter, the blockage ratio, that can increase the maximum power extracted from the flow, relative to an unconfined turbine. The blockage ratio is defined as the swept area of the turbine divided by the cross sectional area of the flow.

Besides the free surface's direct effect on turbine performance through the blockage ratio, the presence of the turbine also affects the free surface level, which can lead to indirect effects on turbine performance and wake characteristics. The vertical placement of a MHK turbine, which will affect free surface fluctuations, depends greatly on the method used for installation. For example, a turbine supported by a floating barge will most likely be close to the free surface whereas a turbine installed on a gravity foundation will be close to the bottom of a channel [18]. Another factor used in determining the vertical placement of a MHK turbine is the velocity gradient in tidal channels. Turbines are believed to operate most efficiently near the free surface because the maximum velocity typically occurs near the surface in tidal channels [19].

Adding a free surface into the numerical simulations of MHK turbines will complicate the modeling and add computational cost. In some situations, the free surface fluctuations may significantly affect the flow, in others it may be acceptable to ignore the presence of the free surface because the effects are negligible. Thus, it is important to determine when it is necessary to include the free surface in numerical modeling of MHK turbines.

It is essential to understand the parameters that control flow around MHK turbines in the presence of a free surface and to develop the non-dimensional parameters that control the coupled turbine-free surface dynamics, in order to determine when it is necessary to model the free surface since MHK turbines can have different diameters, operate at different flow speeds, and at different depths. The non-dimensional number typically applied to open channel flows is the Froude Number.

1.3.2 Froude Number

The Froude number is named after William Froude, a naval Architect who developed the similarity concept for free surface flows [20]. The Froude number is typically defined as

$$Fr = \frac{U}{\sqrt{gl}} \tag{1.2}$$

where U is the flow speed, g is gravitational acceleration, and l is a characteristic length scale. The depth of the water is most commonly used as the characteristic length scale for open channel flows. The Froude number is a ratio of the speed of the flow, U, to the speed of gravity waves, $\sqrt{gl}$. If the Froude number is small, gravity waves propagate on the free surface both upstream and downstream. If, on the other hand the Froude number is greater than one, then surface gravity waves cannot propagate upstream against U (supercritical flow) and surface fluctuations can only travel downstream (in a clear parallel with supersonic flow where pressure

waves cannot travel faster than the flow and therefore only propagate downstream). For the flows studied in this thesis the Froude number is always much less than 1, as discussed in Section 5.2.

The Froude number can be used to compare different flows in the same manner as the Reynolds number. The Froude number allows free surface flows, with different speeds and characteristic lengths, to be compared using a non-dimensional number in order to characterize similarities in free surface behavior between different flows. The challenge with applying the Froude number to flows with MHK turbines is defining the right characteristic length scale. The most commonly used length scale is the channel's height (as is done in hydraulic engineering) which has been done by Myers [21], Whelan [3], and Bahaj [22]. This length scale does not completely describe the effects of a MHK turbine on the free surface profile. For example, a turbine placed near the free surface in a very deep channel will interact differently with the free surface than a turbine placed in the middle or bottom of that same channel. Therefore, in this thesis, other possible length scales such as the distance from the center of the turbine to the free surface, the distance from the tip of the turbine to the free surface, and the turbine diameter will be examined.

1.4 Thesis Outline

Chapter 2, Literature Review, provides an overview of the current research available for MHK turbines, specifically focusing on the operation of MHK turbines in confined flows. Chapter 3, Methodology, describes the methodology and theory used in the thesis. Chapter 4, Numerical Modeling, describes the generic numerical simulations and model settings used in this thesis. Chapter 5, Results and Analysis, discusses the results obtained through the numerical simulations. Chapter 6, Summary, Conclusions and Future Work, provides a summary of this thesis and highlights some of the important conclusions.

Chapter 2

LITERATURE REVIEW

2.1 Energy Potential

It is essential to determine desirable site characteristics before considering the installation of MHK turbines in a given location. Most importantly, it needs to be determined whether there is an amount of available kinetic energy in tidal flows at those sites to make MHK turbines a viable energy source.

Every body of water is subject to the gravitational forces that result in the tides. However, the amplitude of the tidal fluctuations and the magnitude of the tidal current depend on the local bathymetry. In areas where the flow is spatially constrained like between islands, around headlands, and estuarine-type inlets, there can be large tidal variation and fast moving tidal currents resulting in high energy concentrations [23]. Many locations all around the world have been identified as containing suitable tidal currents for power generation by MHK turbines. The important characteristics for MHK turbine sites are fast moving tidal currents and a bi-directional flow. Frequently, locations that meet both of these requirements have high levels of turbulent kinetic energy. MHK turbines can suffer from rapid fatigue failure caused by the unsteady loading resulting from high turbulence levels. Therefore, a detailed understanding of the turbulent induced unsteady loading and a careful design process that takes this engineering challenge into account is critical for the success of MHK turbines in the harsh environment associated with the best resource sites. The restriction of maintenance in an underwater environment may make the robustness of the design even more critical for MHK turbines than it is already in wind turbines.

It is also important to determine the maximum power that can be extracted from

the flow. For wind energy, which deals with an unconstrained incompressible flow, the maximum coefficient of power is equal to 0.593 [24] [25]. This is known as Betz limit and was derived using a stream-tube analysis of the flow around a turbine. The coefficient of power is defined as

$$C_p = \frac{Power}{\frac{1}{2}\rho U_\infty^3 A_d} \tag{2.1}$$

where $Power$ is the power generated by the turbine, ρ is the density of the fluid, U_∞ is the free stream velocity, and A_d is the area of the turbine. This approach is commonly referred to as the Linear Momentum Theory - Actuator Disc Model [25]. The derivation of the Actuator Disc Model is described in detail in Section 3.3.

For tidal energy, even though the current flow speed is typically slower than in wind, the relatively high density of water results in an energy density of tidal currents that makes it recoverable within engineering and economic parameters under certain conditions [23]. Therefore, in locations where currents are bi-directional and velocities exceed 2 m/s, a sufficient amount of energy can be extracted to make tidal energy a viable method of power generation.

In unconstrained flows, or flows with a very small blockage ratio, a MHK turbine will behave similarly to a wind turbine and the Betz Limit can still be applied. However, in many cases, the bathymetry of the potential tidal energy sites and the presence of the free surface constrain the flow and the Betz Limit no longer applies [1], making power coefficients above 59% or even above 100% possible. Several different methods have been derived to determine the available power and maximum coefficient of power in such cases. According to Garrett [1]:

$$P_{max} = \frac{16}{27}(1-\epsilon)^{-2}\frac{1}{2}\rho A_d U_\infty^3 \tag{2.2}$$

where ϵ is the blockage ratio, which is defined as the area of the turbine (A_d) divided by the cross sectional area of the flow, ρ is the fluid density, and U_∞ is the free stream

velocity. There is an extra efficiency multiplier of $(1-\epsilon)^{-2}$ resulting from the flow being constrained. This extra efficiency term goes to one as the blockage ratio goes to zero, reproducing Betz limit.

Garrett′s analysis above, [1], only accounted for the increased blockage ratio because it represents a one-dimensional analysis between two rigid surfaces. The analysis did not address the issue of a change in free surface height resulting from the energy extracted by the MHK turbine potentially affecting the overall energy budget.

Whelan [3] used a similar analysis but accounted for both the blockage ratio and the change in free surface height due to the pressure drop across the turbine related to the energy extracted by the turbine. The extraction of energy (potential and kinetic) is related to the change in pressure as follows:

$$P_{ext} = U_t \cdot \Delta P \cdot A_d \tag{2.3}$$

where ΔP is the change in pressure across the turbine and U_t is the velocity at the turbine. This analysis, [3], uses conservation of mass, conservation of momentum in the stream wise direction, and conservation of energy to develop the theory. The derivation provides an equation for the coefficient of power that is a function of the Froude Number, the blockage ratio, and the axial induction factor. The expression for the axial induction factor is given in Equation 3.31. Given those same values, the change in height of the free surface non-dimensionalized by the initial channel height can also be calculated. Figure 2.1 shows the coefficient of power (C_p) for a given value of the channel's Froude Number ($Fr = 0.22$) at different axial induction factors and blockage ratios. It should be noted that a high blockage ratio can lead to a decrease in the free stream velocity subsequently lowering the maximum power available but not the coefficient of power.

In Whelan et al.'s results, the control volume used did not include the region where wake mixing occurs. Polagye [26] performed a similar analysis but included the mixing region. In this analysis, like in Whelan et al.'s, the power extracted depends on the

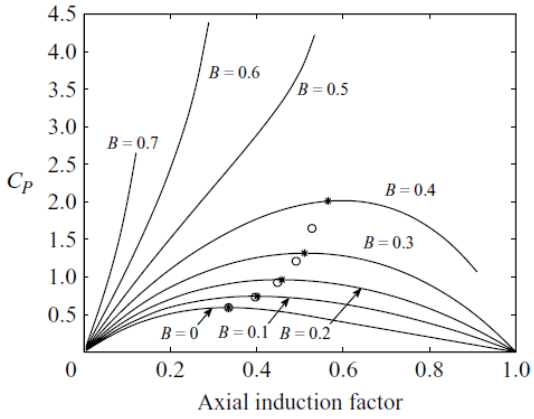

Figure 2.1: Coefficient of Power versus Axial Induction Factor for Fr=0.22 (-*-) and Fr=0 (-o-) [3]

channel's Froude number, the blockage ratio, and the ratio between the inlet velocity and the velocity downstream of the turbine. A relationship is also derived between the power extracted and the power dissipated in the flow. When that relationship was applied to flows with low Froude numbers and blockage ratios, results were similar to Garrett's [1]. Figure 2.2 shows the relationship between the Froude number, the blockage ratio, and the power coefficient. It also shows the relationship between the power extracted and the power dissipated under different flow conditions.

2.2 Turbine Modeling

Due to the challenges of deploying MHK turbines in strong tidal currents, there have been very few full scale experimental tests performed on MHK turbines and none are in the public domain. As a result, much of the analysis in the open literature to date has been performed using scale models and numerical simulations. Numerical simulations can be a very effective and relatively inexpensive method of analyzing MHK turbine dynamics and performance, but they require validation to ensure they

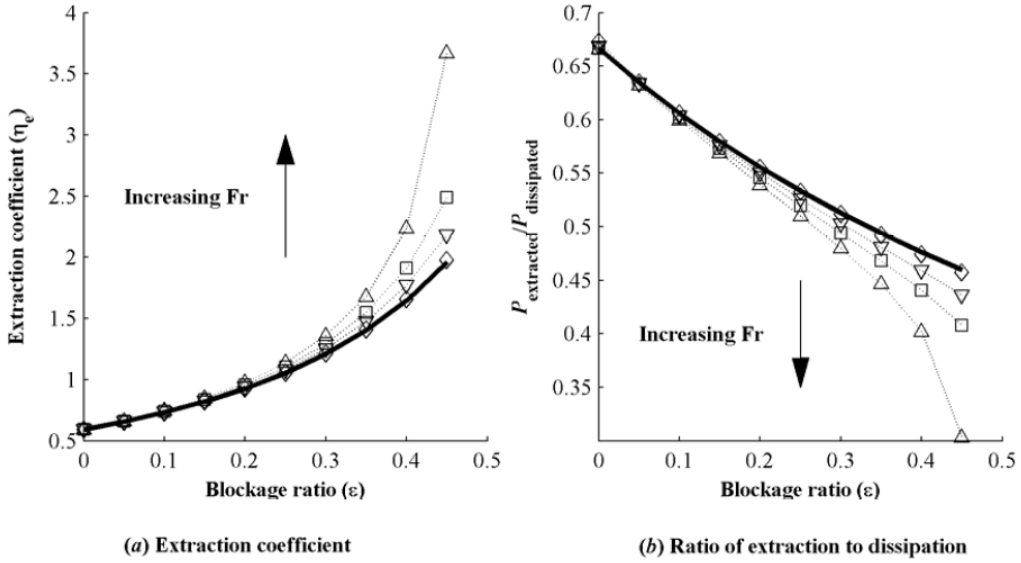

Figure 2.2: Measures of turbine performance at various blockage ratios and Froude numbers for a turbine at the theoretical maximum efficiency. ♢ Fr ≈ 0.05, ▽ Fr ≈ 0.15, □ Fr ≈ 0.2, △ Fr ≈ 0.25, Solid line: results from Garrett [1]. [26]

are truly capturing the physics of the flow.

There are several different methods of modeling MHK turbines, with varying degrees of accuracy. The three numerical models discussed in this thesis are: the Single Reference Frame (SRF) model, the Actuator Disc Model (ADM), and the Blade Element Model (BEM).

2.2.1 Single Reference Frame (SRF) Model

A SRF model models the flow around a turbine blade in a moving reference frame. In a stationary reference frame the flow around a turbine is unsteady because the blades are moving. By using a reference frame that moves with the same rotational speed as the turbine the problem becomes steady, saving computational time. When using a rotating reference frame, the Coriolis and Centripetal accelerations must be added to

the momentum equation [27]. The SRF model is capable of capturing the boundary layer that develops along the surface of the blade, as well as flow separation, requiring a very fine mesh near the blade. This results in a relatively large computational grid and long computational runtimes. For example, when modeling the NREL phase VI turbine, the ADM and BEM only required 1.65 million mesh elements, whereas, the SRF model required 5.1 million mesh elements and it took about 24 times longer to converge [27]. For that reason, it can be beneficial to use a simpler model that does not include the blade geometry.

2.2.2 Actuator Disc Model (ADM)

ADM is based on one dimensional stream tube analysis of the flow. In this analysis the turbine is represented by a body force that is applied to the flow, see Figure 2.3 [25]. The force is applied uniformly over the swept area of the turbine. The derivation of the ADM is provided in Section 3.3. In numerical simulations and lab experiments, the turbine is represented by a porous media in the shape of a disc, referred to as an actuator disc, which applies a force to the flow similar to the thrust force of a turbine [28].

An actuator disc causes a constant resistance to a flow field that imposes the thrust force on the flow [29]. The magnitude of force is a function of the resistant coefficient of the porous media and the incoming flow speed. The porosity of the disc can be changed in order to change the resistant coefficient and subsequently the thrust force [29]. It should be noted that different materials (or materials with different pore sizes) even with the same porosity can produce different thrusts and different wake deficits due to the flow characteristics through the pores [23].

The ADM is a simplistic model that has relatively short computational times when compared to the BEM and the SRF model [27]. The shorter computational time is partially due to the fact that the flow can be considered steady-state because the turbine is modeled as a disc instead of rotating blades [29]. The short time is also a

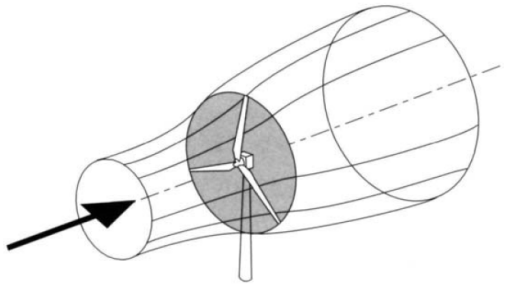

Figure 2.3: Energy Extracting Stream-Tube of a Wind Turbine [25]

result of the mesh resolution. The boundary layer and flow separation on the blades are not being modeled. Furthermore, because of the disc's simplicity, some of the flow physics are not captured. For example, porous discs used experimentally do not extract energy, but instead the disc turns kinetic energy into small scale turbulence that dissipates quickly. Vortex shedding is also different for a porous disc than for a turbine, and the disc does not induce any swirl [28].

In numerical simulations, the actuator disc is implemented by creating a zone in the fluid domain with the same cross sectional area as the turbine rotor and defining it as a porous zone. The porous zone is represented by a source term in the momentum equation [30].

2.2.3 Blade Element Model (BEM)

The ADM has been shown to not accurately model the near wake behavior of a MHK turbine and has been shown to under predict the velocity deficit in the far wake [27]. Thus, it may be beneficial to use a model that captures more of the physics of the turbine. Two such models that have been applied to MHK turbines as well as wind turbines are: the Blade Element Model (BEM) and the Blade Element Momentum Theory (BEMT) Model. BEM applies Blade Element Theory (BET) and the BEMT model combines BET with Linear Momentum Theory (LMT), see Figure 4.5 [31].

Linear Momentum Theory is used to calculate the axial and circumferential induction factors and BET is used to calculate the lift and drag forces on different sections of the rotor blade. The thrust and power are integrated over the entire blade, [31]. These models are discussed in more detail in Section 3.2.1. Turnock [32], Batten [33], and Javaherchi [27] have applied the BEMT model and the BEM to MHK turbines.

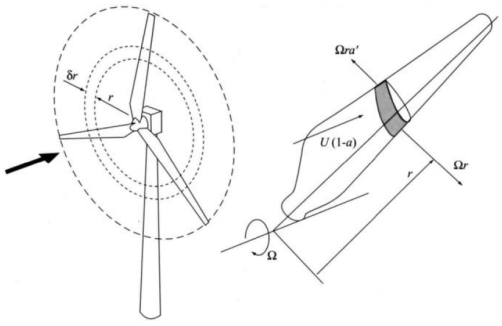

Figure 2.4: Blade Element Momentum Theory [25]

Turnock [32] validated the results from CWIND, an in-house BEMT code, with experimental data from Bahaj [34] [35]. Then CWIND was used to validate a newly developed code that coupled the Reynolds Averaged Navier Stokes Equations with BEMT. The RANS/BEMT code was used to study array optimization for MHK turbines. The power production was found to be dependent on the lateral and longitudinal spacing of the turbines such that small lateral spacing and large longitudinal spacing provided the optimum arrangement [32].

Bahaj [31] validated two numerical codes based on BEMT, which were modifications of wind energy codes, against experimental data and showed their applicability for analyzing new MHK turbine technologies. These codes were incapable of modeling confinement effects, so a blockage correction was applied in order to predict actual performance. It should be noted that one code overestimated power and the other code underestimated thrust. This may have been the result of inaccurate blockage

corrections. The lift and drag coefficients required for the blade element models were determined using Xfoil, a 2-D potential flow airfoil performance code.

Javaherchi [27] performed numerical simulations using the SRF model, the Actuator Disc Model, and an implementation of the BEM, the Virtual Blade Model (VBM). The NREL Phase VI wind turbine was first simulated using the three different models. The results from these simulations were validated against public results. Once the simulation models were partially validated on HAWT experimental results, the same methodology was applied to MHK turbines. He showed that VBM, when applied to MHK turbines, was generally in good agreement with the more accurate SRF model. Some of the differences between the two models were: the VBM did not resolve all of the details directly downstream of the turbine, and the tip vortices were not properly captured. The SRF model showed that the wake became axi-symmetric a short distance downstream of the turbine (1-2 D). This would enable a simpler model to be applied for studies only requiring information on the far wake. Javaherchi showed that ADM failed to capture the flow physics directly behind the turbine as well as any tip vortex shedding. In addition, it was shown that the velocity deficit for the ADM in the near wake was significantly different than the wake deficit of the SRF model and the VBM [27]. Javaherchi concluded the VBM was the best choice to use in future studies of the behavior of the far wake.

2.3 Free Surface Effects on MHK Turbines

In many ways, tidal energy is similar to wind energy and the same modeling techniques can be applied to both. However, there are several key differences. Wind turbines convert kinetic energy off the bottom of the atmospheric boundary layer and, since wind turbines only take a very small portion of the total energy and the pressure wake recovers, the flow can be treated as unconstrained [19]. Tidal energy, on the other hand, converts potential energy into usable power. Decreasing the potential energy in the channel lowers the channel depth at the outlet, which causes the flow to

accelerate in order to conserve mass, hence for tidal energy, the kinetic energy in the flow is increased. In some regions where MHK turbines can potentially be installed, the depth of the turbine is on the same scale as the turbine diameter which can affect the power produced. The wake structure may be influenced by the proximity of the turbine to the free surface or sea floor because the presence of a boundary can lead to flow acceleration above and below the turbine [23].

According to Myers [23], the upper 15 meters of a waterway experience the effects of wave generated turbulence, and the bottom one-third of the waterway has high levels of turbulent fluctuations, resulting from the influence of the bottom boundary layer. This makes the middle third of the water column the most suitable for MHK turbine installations, see Figure 2.5. Many waterways such as rivers or estuaries where MHK turbines maybe placed, however, are not deep enough to avoid the upper 15 meters of the water column. Therefore, the turbine may experience the effects of the free surface presence.

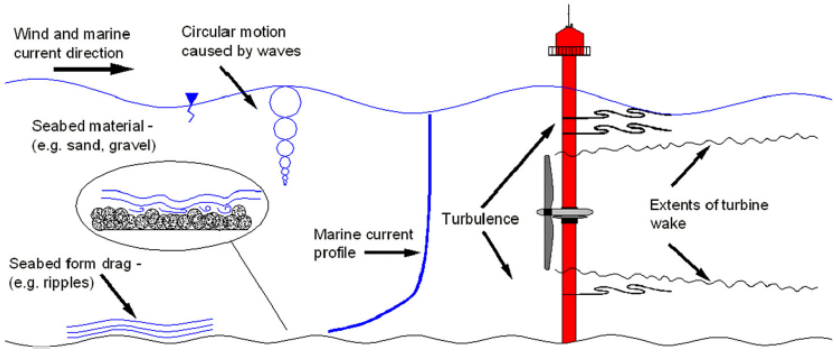

Figure 2.5: Some factors that affect turbine performance and wake structure [22]

2.3.1 Experiments Conducted with a Free Surface

Producing a small scale model of a horizontal axis turbine is very difficult because it is impossible to maintain all of the important non-dimensional numbers, such as the

Reynolds number, Tip Speed Ratio, Coefficient of Thrust, Coefficient of Power, and some form of the Froude number, without significantly changing the downstream flow [23]. Therefore, it is sometimes necessary to use an alternative method for modeling a turbine. Myers [23], used a porous disc as a reasonable substitute for an actual turbine because the structure of the near wake has a small effect on the far wake properties. The porous disc creates a thrust which can be adjusted by changing the porosity of the disc, and the area of the disc can be the same as the swept area of the turbine. These factors help to maintain some flow properties.

Scaling of open channel flow itself involves maintaining two important non-dimensional numbers, the Reynolds number and the Froude number. Scaling of both of these numbers experimentally is not possible. For bounded flows, the Froude number is important because of the close proximity of the free surface where the gravitational effects cannot be ignored [23], and the Reynolds number is important because of the proximity of the seabed where viscous forces cannot be ignored [21]. Most experiments maintain Froude number similarity while ensuring the experiments' Reynolds number is in the same turbulent regime as the full-scale turbine [21].

Myers [21] performed several experiments where the vertical position of a porous disc was varied to determine how the vertical position affects the turbine wake. In the experiments, the disc was centered at 0.33d, 0.5d, 0.66d, and 0.75d where d is the depth of the channel. The turbine's diameter was 0.25d. When the disc was centered at 0.66d and 0.75d it produced very similar velocity deficits to the disc at 0.5d [21], see Figure 2.6. By examining the wake, it can be seen that with a constrained flow the axi-symmetric wake assumption, which is sometime applied for wind turbines, is no longer valid [23]. Myers did not comment on the free surface fluctuations.

Sun [19] also performed experiments involving a free surface. A mesh disc was used to represent the turbine, considering the thrust force as the main factor in wake development [19]. The experiment was performed in the field instead of a flume to simulate realistic operating conditions. According to the velocity profiles measured

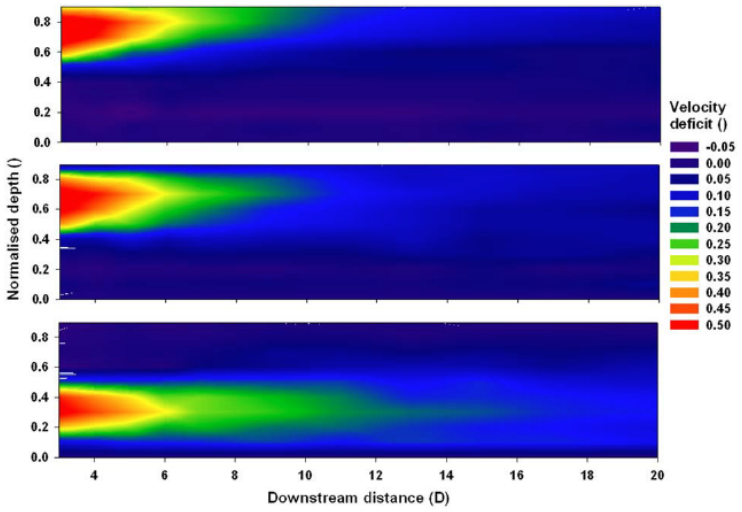

Figure 2.6: Center plane velocity deficits for varying disc submersion depths. Disc centered at 0.75d (top), 0.66d (center), and 0.33d (bottom) [23].

in the wake, a Gaussian-like distribution was found radially and the velocity deficit gradually recovers as expected.

2.3.2 Approximations used for accounting for the presence of a free surface

There are several different methods of modeling a free surface depending on the level of complexity in the modeling and simulation involved. Turnock [32], MacLeod [36], and Hall [9] used a shear free boundary condition to represent the free surface. This requires that the drop in free surface height resulting from the turbine is small enough that its effects on the flow are negligible [9]. Approximating the free surface with a shear free boundary can be justified by the following analysis.

At a free surface interface the shear in the air equals the shear in the water.

$$\mu_{air}\frac{\partial V_{air}}{\partial z}|_{z=interface} = \mu_{water}\frac{\partial V_{water}}{\partial z}|_{z=interface} \tag{2.4}$$

Where μ is the fluid viscosity, V is the velocity, and z is the vertical direction. Since

the $\mu_{air} \ll \mu_{water}$

$$\frac{\mu_{air}}{\mu_{water}} \frac{\partial V_{air}}{\partial z}|_{z=interface} = \frac{\partial V_{water}}{\partial z}|_{z=interface} \approx 0 \tag{2.5}$$

Implying, the shear is approximately zero and the boundary can be assumed to be shear free but this does not account for any surface fluctuations that may occur.

Myers' numerical model [21] took a different approach. The vertical and horizontal wake expansions were decoupled so the vertical wake expansion could have boundaries applied. Then, the two separate wakes were solved and their solutions combined to obtain the full wake. The shear-layer Navier Stokes equation for axi-symmetric flows and an eddy-viscosity turbulence model, requiring a length scale and a velocity scale, were used to calculate the Reynolds Stresses. The wake width was used as the length scale and the centerline velocity deficit was used as the velocity scale [21]. The wake width and centerline velocity deficit were derived from semi-empirical equations in order to provide a Gaussian velocity profile [21]. When the solution was decoupled, the horizontal wake portion could be treated as axi-symmetric and unconstrained. The vertical portion of the wake had to be treated differently because of the effects of the bounding surfaces. To account for the limited expansion caused by the bounding surfaces, the vertical wake width was restricted [21]. This approach allowed the axi-symmetric assumption to be used on the vertical wake minimizing computational expenses. The upper and lower regions of the vertical wake could also behave differently depending on the proximity to the bounding surfaces, thus, the model could be further decoupled to separate the upper and lower vertical shear layers. The individual shear layers were first solved separately, before combining their solutions to obtain the solution for the full wake [21]. The results provided good agreement with experimental data, but there were some discrepancies near the bounding surfaces.

2.3.3 Modeling the Free Surface

Harrison [29], Sun [19][18], and Consul [37] studied the effect of simulating free surface fluctuations in the computational modeling of MHK turbines. According to Harrison, modeling the free surface is the most suitable option to capture the possible flow deceleration near the surface of an open channel resulting from secondary currents caused by the channel wall [29]. Figure 2.7 shows this deceleration near the free surface recorded experimentally. Harrison, Sun, and Consul used a multiphase model in their numerical simulations to model the two different fluids: water and air. In all cases, the multiphase model applied to their simulations was the Volume of Fluid Method, described in Section 3.5.1.

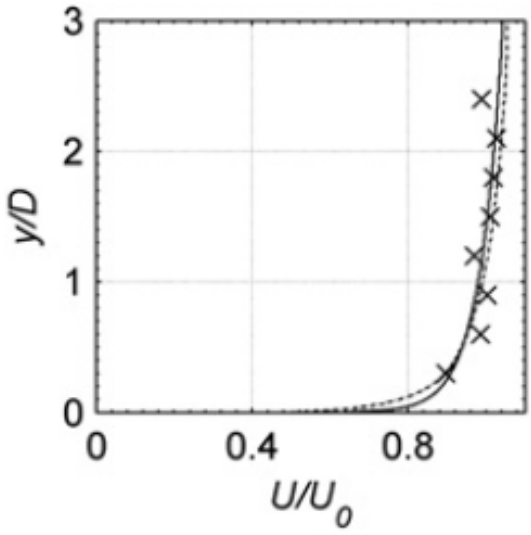

Figure 2.7: Modeled and measured normalized velocity profiles at the centerline of the channel. D is the turbine diameter, y is the vertical location, U_o is the velocity of the flow in the free stream, and U is the local time-averaged flow velocity. The solid line is the boundary layer model for the velocity profile which was used as the inlet boundary condition. The dashed line was the modeled velocity profile at 15 turbine diameters downstream. The crosses represent the experimental data. [29]

Sun [18] used a porous media region to represent the actuator disc model approximation of a MHK turbine in numerical simulations. The mesh was refined in the region near the free surface to capture any free surface fluctuations. The boundary conditions used in these simulations were as follows: a mass flow rate inlet, a pressure outlet set using a User Defined Function (UDF), a symmetry boundary on the top of the domain, and a no slip wall on the bottom of the domain [19][18]. The actuator disc provided a blockage ratio of 17% and the disc was originally centered at half the water depth, see Figure 2.8. The vertical position of the turbine in the channel was then varied in order to determine the effects of the free surface on the wake of the turbine. The turbine was placed at a depth of 1d, 1.5d, and 2d, where d is the characteristic length of the turbine and the depth was the distance from the center of the turbine to the free surface. The simulations showed that the distance downstream of the turbine where the wake expanded to reach the free surface was related to the vertical position of the turbine. When the turbine was closer to the free surface, the wake expanded to the free surface in a shorter distance than when the turbine was placed deeper in the channel. It was also concluded that the wake recovered faster when the turbine was closer to the free surface, as seen in Figure 2.9 [18].

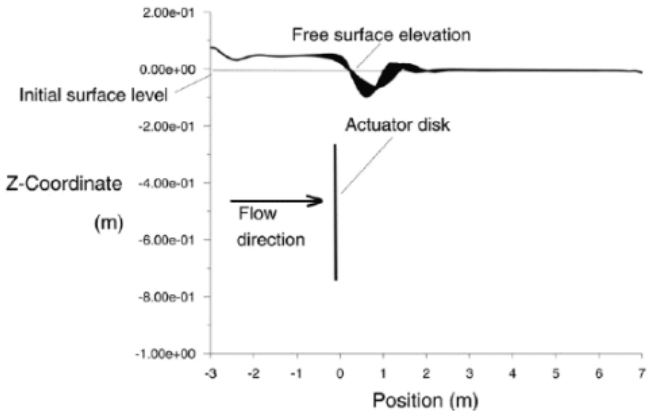

Figure 2.8: Free surface profile at channel centerline [18]

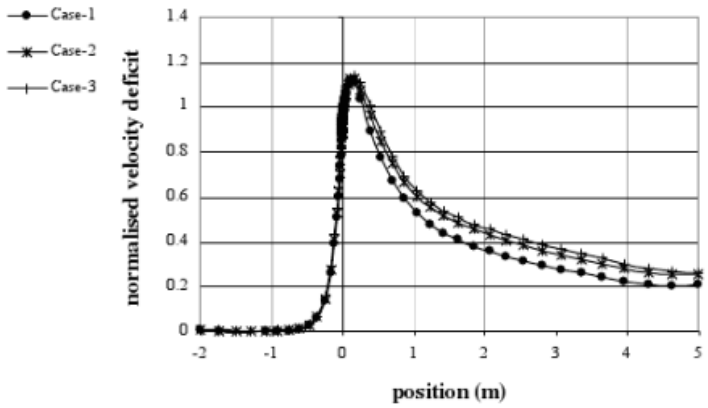

Figure 2.9: Normalized centerline mean velocity deficit, Case 1 Depth=1d, Case 2 Depth =1.5d, Case 3 Depth=2d, where d is the characteristic length of the turbine and the depth was the distance from the center of the turbine to the free surface [18].

Harrison [29] also used ADM to model a MHK turbine with a free surface. This simulation uses the $k-\omega$ turbulence model because the $k-\omega$ model performs better in the boundary layer than the traditional $k-\epsilon$ turbulence model . A user-specified velocity profile for the inlet boundary condition that was fitted to a boundary layer profile recorded experimentally was used to force the flow. The drop in elevation of the free surface caused by the energy dissipated by the actuator disc was calculated and used to assign a hydrostatic pressure profile for the outlet boundary condition. The model was unable to capture the deceleration near the surface of the flow because of limitations in their simulations concerning resolution of secondary flows. This inaccurate modeling affected the velocity in the upper region of flow such that the model produced a higher velocity than recorded in the experiments.

In the same work, Harrison [29] adjusted the porous disc's coefficient of thrust to determine its effects on the flow. The coefficient of thrust increased while the minimum centerline velocity decreased. This results in a shorter near-wake region because the top and bottom shear layers merge closer to the disc. The model of the far wake

accurately predicted the trends of the experimental data. The level of agreement, however, varied with the vertical location of the actuator disc. The model deviated increasingly from the experimental data when it was closer to the free surface.

Consul [37] modeled a cross flow turbine in an open channel. He performed two different sets of simulations. One set used a shear free boundary to represent the free surface, referred to as rigid lid simulation. The other set of simulations allowed for deformation of the free surface by applying the Volume of Fluid multiphase model. The turbine used for the simulations was a three bladed Darrieus turbine. The simulations were performed in a two-dimensional plane perpendicular to the axis of rotation. The geometry of the blade's airfoil was modeled to resolve the flow past the blades, and the blades were rotated using a sliding mesh. Three different blockage ratios were examined, 50%, 25%, and 12.5%. Consul observed that the coefficient of power (C_p) increased with an increase in blockage ratio, and the Tip Speed Ratio (λ) that corresponds to the maximum C_p increased with the increase in blockage ratio, see Figure 2.10.

Consul also examined the effects of the shear free boundary approximation on the flow. He concluded that at low blockage ratios the C_p was approximately the same for both the rigid lid simulations and the VOF simulations. At high blockage ratios, e.g. 50%, however, the C_p for the VOF simulation was 6.7% greater than the rigid lid simulation [37]. The influence of the Froude number on the performance of the turbine was also discussed. The length scale used for the Froude number was the channel depth. For simulations with a blockage ratio of 50% the C_p depended on the upstream Froude number, matching the prediction of Whelan [3], see Figure 2.11. The change in height of the free surface also varied with the upstream Froude number. This issue of choice of non-dimensional parameters will be discussed in Section 5.2 of this thesis.

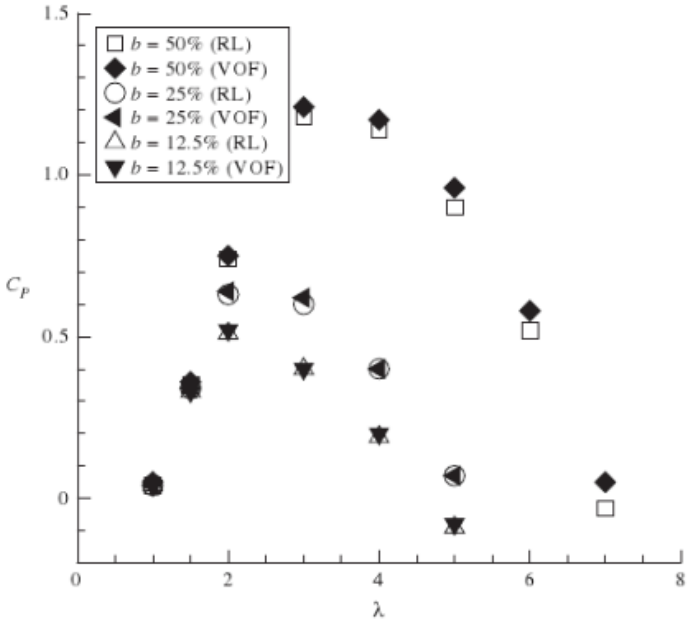

Figure 2.10: Dependency of turbine power coefficient, C_p, on blockage and free-surface model (RL, rigid lid; VOF, volume of fluid) [37].

2.4 Motivation for the Work Performed in this Thesis

There has been a limited amount of research studying the effects of a free surface on the operating characteristics of MHK turbines. The studies discussed previously, with the exception of Consul's paper [37] which focused on a two-dimensional analysis of a cross flow turbine, focused on the effect of the confining surfaces on the wake characteristics. These studies do not address the power extracted by the turbine or the free surface fluctuations that result from the turbine. Those are the primary issues addressed in this thesis.

In most potential MHK turbine locations, the blockage ratio will be low enough, and the free surface distance to the turbine will be large enough, that the presence of a free surface will not affect the turbine performance or the fluctuations in free

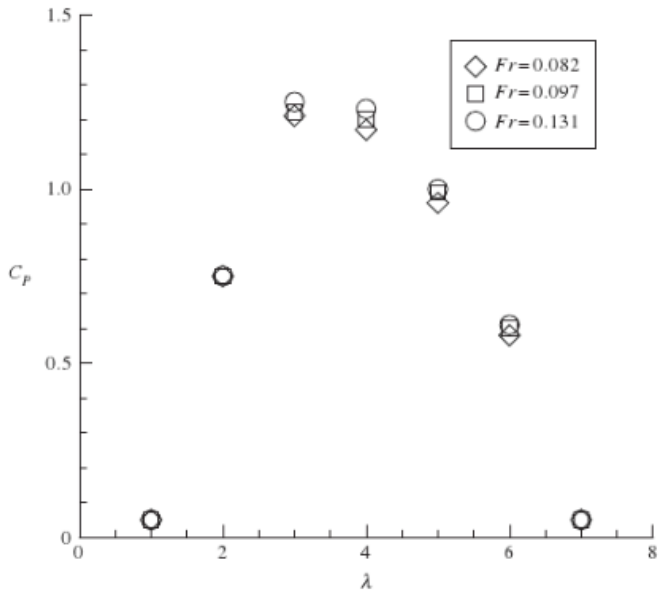

Figure 2.11: Power coefficient, C_p, for various Fr, for a flow with a blockage ratio of 50% [37].

surface height. However, there are a number of key issues that make the study of effects of the blockage ratio and the turbine depth on the operating characteristics of MHK turbines relevant. As discussed previously, performing full scale testing of MHK turbines is very challenging, so significant research work has been performed using scale models in flumes. In flume experiments, the blockage ratio is typically much higher, and the free surface much closer to the turbine rotor, than what will be seen in the field. Thus, it is important to determine if the coefficient of power found experimentally has been affected by the unnaturally high blockage ratio or free surface effects. Furthermore, there are some bodies of water, such as rivers, channels, and estuaries, where the blockage ratio can potentially be high enough, or the free surface distance to the turbine low enough, to affect the flow. In this situations, it is important to determine the limiting values for the parameters that control free surface

effects so that the MHK turbine installation can avoid or plan for those influences in a quantitative manner.

Chapter 3

METHODOLOGY

3.1 Numerical Modeling Theory

The non-linearity and turbulent nature of fluid flows of interest in Marine Hydrokinetic Energy prevent all but the simplest of these fluid mechanics problems from having closed form solutions. A powerful alternative, along with experimentation, is to solved them numerically. Computational Fluid Dynamics (CFD) has become, over the last four decades, a significant source of physical understanding and engineering modeling to complement mathematical exact solutions and laboratory and field experiments.

The CFD software used for this thesis is ANSYS Fluent, version 14.0. Fluent is a Finite Volume Solver. The numerical algorithm used in a Finite Volume Solver "consists of the following steps:

- Integration of the governing equations of fluid flow over all the (finite) control volumes of the domain.
- Discretization - conversion of the resulting integral equations into a system of algebraic equations.
- Solution of the algebraic equations by an iterative method." [38]

3.1.1 Governing Equations

The problem domain is broken up into smaller volumes called elements. Fluent applies user specified boundary conditions and initial conditions to the domain in order

to solve the governing equations for the mean flow variables in each fluid element. The governing flow equations used are the Reynolds Averaged Navier Stokes (RANS) equations. The RANS equations are derived by substituting the Reynolds Decomposition for turbulent fluid variables, velocity and pressure for incompressible flows, into the conservation of mass and momentum equations, then time-averaging the equations. The Reynolds Decomposition of the velocity and pressure expresses the instantaneous values of those variables and their derivatives as the sum of a mean, "expected", value and the fluctuating value:

$$u_i = \overline{u_i} + u_i' \tag{3.1}$$

$$p = \overline{p} + p' \tag{3.2}$$

where $\overline{u}$ is the mean flow velocity, $\overline{p}$ is the mean pressure, u' is the fluctuating velocity, and p' is the fluctuating pressure. The resulting RANS equations, written in tensor notation, are laid out in Equations 3.3 and 3.4:

$$\frac{\partial \rho}{\partial t} + \frac{\partial}{\partial x_i}(\rho \overline{u}_i) = 0 \tag{3.3}$$

$$\frac{\partial}{\partial t}(\rho \overline{u}_i) + \frac{\partial}{\partial x_i}(\rho \overline{u}_i \overline{u}_j) = -\frac{\partial \overline{p}}{\partial x_i} + \frac{\partial}{\partial x_j}\left[\mu\left(\frac{\partial \overline{u}_i}{\partial x_j} + \frac{\partial \overline{u}_j}{\partial x_i}\right)\right] + \frac{\partial}{\partial x_j}(-\rho\overline{u_i' u_j'}) + S_i \tag{3.4}$$

The RANS equations contain many of the same terms found in the instantaneous conservation of mass and momentum equations, such as a temporal acceleration term, the convective acceleration term, a pressure gradient term, the viscous stress gradient term, and a source term, S_i [38]. The RANS equations are formulated with the mean velocity and mean pressure as the key unknowns, instead of the instantaneous velocity and instantaneous pressure in the Navier Stokes equation. The RANS equations, however, have an additional term containing the fluctuating velocities. This additional term, $-\rho\overline{u_i' u_j'}$, is traditionally referred to as the Reynolds Stress term, and it represents the effects of turbulence transport on the mean flow. This term, which

potentially represent nine independent unknowns separate from the mean velocity components and pressure must be expressed in terms of those key variables, in order to make the RANS equations a mathematically sound problem (four equations and four unknowns). This important aspect of the RANS equations and their methods of solution for turbulent flows is classically referred to as the closure problem.

3.1.2 Turbulence Modeling

The closure problem described in the previous paragraph presents a requirement to model the Reynolds stresses as a function of other resolved variables in the problem. This has given rise to a wide variety of turbulence modeling approaches, compatible with the basic premise of the RANS equation, to close the problem in a manageable systems of equations that can be solved computationally. One commonly used approach is the Boussinesq Hypothesis, which states that the Reynolds stresses are proportional to the mean shear in the flow (and have zero trace to be compatible with the incompressibility condition):

$$-\rho\overline{u_i'u_j'} = \mu_t\left(\frac{\partial\overline{u_i}}{\partial x_j} + \frac{\partial\overline{u_j}}{\partial x_i}\right) - \frac{2}{3}\rho k\delta_{ij} \tag{3.5}$$

where k is the turbulent kinetic energy, μ_t is the turbulent viscosity, and δ_{ij} is the Dirac Delta, from [38]. Through dimensional analysis, it can be shown that the turbulence viscosity term could be written as:

$$\mu_t = C\rho v l \tag{3.6}$$

where C is a coefficient, ρ is the density, v is a velocity scale, and l is a length scale [38]. Many different models have been developed to solve for the turbulent viscosity by defining different length and velocity scales. The models all have varying degrees of accuracy. For the most part, the more accurate the model, the longer the CFD simulation takes to reach a solution. The method used in this thesis is called the

$k-\epsilon$ turbulence model. The $k-\epsilon$ model was chosen because it is a commonly used, robust turbulence model. Since the model used to represent the turbine's effects on the flow does not have a solid boundary and the effects of the channel bottom are not of primary importance to the research performed here, the mesh in that region was not refined in a way to resolve the boundary layer, so a turbulence model like the $k-\omega$ turbulence model or Spalart-Allmaras turbulence model, that more accurately models flow near a solid surface, were not required. The length scale and velocity scale for the $k-\epsilon$ model are

$$v = k^{1/2} \tag{3.7}$$

$$l = \frac{k^{3/2}}{\epsilon} \tag{3.8}$$

where k is the turbulent kinetic energy and ϵ is the turbulent dissipation rate. Such that

$$\mu_t = \rho C_\mu \frac{k^2}{\epsilon} \tag{3.9}$$

where C_μ is a dimensionless constant normally taken to be $C_\mu = 0.09$. Thus, k and ϵ must be calculated to obtain the turbulent viscosity. The turbulent kinetic energy is equal to

$$k = \frac{1}{2}\overline{u_i'^2} \tag{3.10}$$

and the turbulent dissipation rate is equal to

$$\epsilon = 2\nu\overline{(s_{ij}' \cdot s_{ij}')} \tag{3.11}$$

$$s_{ij}' = \frac{1}{2}\left(\frac{\partial u_i'}{\partial x_j} + \frac{\partial u_j'}{\partial x_i}\right) \tag{3.12}$$

k and ϵ depend on the fluctuating part of the velocity and their respective transport equations depend on fluctuating velocity and pressure terms. Therefore, neither equation can be solved for directly with only the mean flow terms. In order to solve for k and ϵ, the fluctuating terms in their transport equations must be modeled using mean flow quantities and coefficients. This is done for the turbulent kinetic energy transport equation by dividing the terms into a temporal rate of change term, a convection term, a diffusion term, a production term based on the mean shear and a destruction term based on the turbulent dissipation rate, [38]

$$\frac{\partial(\rho k)}{\partial t} + \frac{\partial}{\partial x_i}(\rho k \bar{u}_i) = \frac{\partial}{\partial x_i}\left(\frac{\mu_t}{\sigma_k}\frac{\partial k}{\partial x_i}\right) + 2\mu_t S_{ij} \cdot S_{ij} - \rho\epsilon \tag{3.13}$$

where σ_k is the turbulent Prandtl number for kinetic energy, typically taken to be $\sigma_k = 1$, and S_{ij} is the mean strain rate

$$S_{ij} = \frac{1}{2}\left(\frac{\partial \bar{u}_i}{\partial x_j} + \frac{\partial \bar{u}_j}{\partial x_i}\right). \tag{3.14}$$

The equation for the turbulent dissipation rate used as part of the $k-\epsilon$ model is purely empirical. ϵ is commonly viewed as the rate of energy transfer from large scales to small scales through the turbulent cascade. As such it can be determined entirely by the large and inertial scale motions, and not the dissipative range. The exact equation for ϵ would contains multiple dissipative range processes but that would un-necessarily complicate the calculation, therefore the equation for ϵ used in the $k-\epsilon$ model is based on larger scale motion and as a result is empirical. It has a similar structure to the turbulent kinetic energy transport equation: a temporal rate of change term, a convection term, a diffusion term, a production term and a destruction term [38].

$$\frac{\partial \rho\epsilon}{\partial t} + \frac{\partial}{\partial x_i}(\rho\epsilon \bar{u}_i) = \frac{\partial}{\partial x_i}\left(\frac{\mu_t}{\sigma_\epsilon}\frac{\partial \epsilon}{\partial x_i}\right) + C_{\epsilon 1}\frac{\epsilon}{k}2\mu_t S_{ij} \cdot S_{ij} - C_{\epsilon 2}\rho\frac{\epsilon^2}{k} \tag{3.15}$$

where $C_{\epsilon 1}$ is an empirical model constant, normally taken to be $C_{\epsilon 1} = 1.44$, $C_{\epsilon 2}$

is another empirical model constant, normally taken to be $C_{\epsilon 2} = 1.92$, and σ_ϵ is the turbulent Prandtl number for the dissipation rate, normally approximated as a constant with value $\sigma_\epsilon = 1.3$ [39]. For the purpose of this thesis, none of the modeling constants were changed.

3.2 Blade Element Theory (BET)

The model used to represent the presence of a MHK turbine in the flow is based on the Blade Element Theory (BET). In BET, an aerodynamic body, in this case the turbine blades, is discretized into spanwise elements of width δr at position r, see Figure 3.1. The lift (δL) and drag (δD) forces on each blade element are calculated using its relative velocity to the ambient flow (w) and the coefficients of lift (C_L) and drag (C_D) for its airfoil (or hydrofoil) shape. C_L and C_D are generally functions of the Reynolds Number (Re), and the Angle of Attack (α) [25, 27].

$$\delta L = \frac{1}{2}\rho w^2 c C_L(\alpha, Re)\delta r \tag{3.16}$$

$$\delta D = \frac{1}{2}\rho w^2 c C_d(\alpha, Re)\delta r \tag{3.17}$$

The relative velocity, w, is the resultant of the axial velocity of the ambient fluid (at the turbine) and the rotational velocity of the blade:

$$w = \sqrt{V_{stream}^2 + (\omega r)^2}. \tag{3.18}$$

The Angle of Attack is the angle between the blade element chord and the incoming, relative, current velocity. From the elemental forces, the axial induction factor (a) and tangential flow induction factor (a') for each blade element can be calculated. The torque and power can then be determined using the induction factors [25].

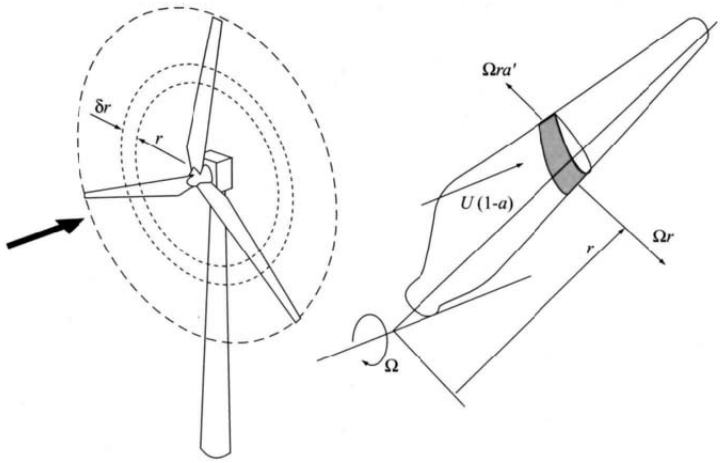

Figure 3.1: A Blade Element sweeps a ring of the rotor disc, producing a mean force on the fluid that passes through it. The BET calculates that force applied on the fluid and introduces it into the Navier Stokes equations as a body force (source) [25].

3.2.1 Virtual Blade Model

The Virtual Blade Model (VBM) is ANSYS Fluent's implementation of BET. The VBM model uses BET to develop source terms for the momentum equation that are applied to the Rotor Region. The Rotor Region is a cylindrical disc in the fluid domain that represents the area swept by the turbine rotor. The required user inputs for the virtual blade model are: the blade geometry, angular velocity, and a look-up table containing values of C_L and C_D for different values of angle of attack, α, and Reynolds number. The blade geometry includes the number of blades, the radius of the blades, the total pitch, the chord length of each blade section, and the twist of each blade section. The look-up table for C_L and C_D depend on the airfoil used at each radial position on the blade and can be developed experimentally, using 2-D simulations like X-foil, or a 3-D model such as the SRF model. VBM uses the computed incoming velocity and the provided angular velocity to calculate α and Re.

The code uses those values and the user supplied look-up tables to obtain the local C_L and C_D for each rotor section. The forces on each section are computed using the following equation:

$$f_{L,D} = C_{L,D}(\alpha, Re)c(r/R)\frac{\rho w^2}{2} \tag{3.19}$$

where $f_{L,D}$ is the force on a blade element, c is the chord length of the blade element, and w is the relative velocity of the fluid to the blade [2]. The force is averaged over an entire revolution to smooth the forces applied on the flow across the entire rotor disc, instead of applying them at the instantaneous location of the blades. The force on each cell is calculated as:

$$F_{L,D_{cell}} = N_b\frac{\delta r \cdot r\delta\theta}{2\pi}f_{L,D} \tag{3.20}$$

where N_b is the number of blades, r is the radial position, and θ is the azimuthal coordinate[2]. The source term that is applied to each cell in the rotor region is

$$\vec{S}_{cell} = -\frac{\vec{F}_{cell}}{V_{cell}} \tag{3.21}$$

where V_{cell} is the volume of the cell [2]. The source term is added into the conservation of momentum equation applied to the rotor region. Then, the conservation of mass and momentum equation are solved for the velocity and the pressure. This process is repeated until the solution converges. See Section 4.3.2 for a description of numerical simulation convergence.

3.3 Actuator Disc Model

The Virtual Blade Model is used to model the turbine blades, but it does not accurately model the turbine's hub. The hub produces drag that will affect the flow but does not produce lift, something the VBM fails to capture [40]. The Actuator Disc

Model (ADM) was used previously by Gosset [40] to model the hub. This method produced accurate results and was applied for the same purpose in this thesis.

ADM uses Actuator Disc Theory, also known as Linear Momentum Theory, to model the flow field around an aerodynamic object that produces a discontinuity in the pressure, but not the velocity. The theory uses one-dimensional streamtube analysis of the flow field. The object (the turbine hub in the case of this thesis) is modeled as a permeable surface (or porous media) of the same area, known as an Actuator Disc. The permeable surface allows fluid to pass through the disc but creates a pressure difference across the disc. The force on the fluid caused by the pressure difference is representative of the drag force produced by the hub. The pressure difference across the disc, and subsequently the drag, can be modified by changing the permeability of the disc.

The permeability constant of the Actuator Disc that is used to represent the hub of the turbine is required as an input to the model. This value can be determined by performing control volume analysis on the flow around the turbine hub, as follows.

The necessary assumptions for this analysis are; one-dimensional steady state, incompressible flow. The pressure far downstream in the wake is approximately equal to the free stream pressure upstream of the actuator disc. The control volume is assumed to be a stream tube that encompasses the hub. It starts far upstream of the device where the flow has not been affected by the turbine and ends far downstream of the device where the velocity of the fluid is uniform in the streamwise direction, see Figure 3.2.

The equation for conservation of mass in a control volume is

$$\frac{\partial}{\partial t}\int_{C.V.} \rho dV + \int_{C.S.} \rho \vec{u} \cdot \vec{n} dA = 0 \tag{3.22}$$

where $C.V.$ is the control volume, $C.S.$ is the control surfaces (boundaries), ρ is the density, $\vec{u}$ is the velocity vector, V is the volume, A is the area, and $\vec{n}$ is the normal vector. When the ADM assumptions are applied to the equation it simplifies to

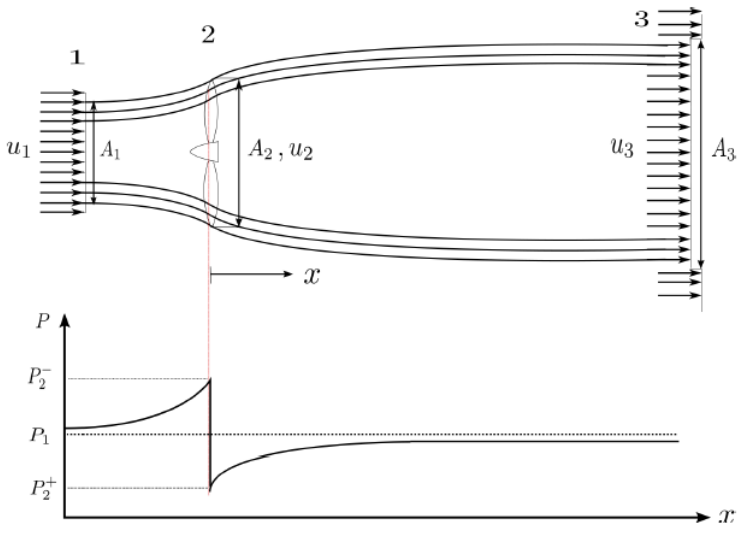

Figure 3.2: Actuator Disc Model of a turbine using a stream tube analysis [27].

$$u_1 A_1 = u_2 A_2 = u_3 A_3 \tag{3.23}$$

where u represents the velocity, A represents the cross sectional area of the stream tube at a specific location, the subscript 1 refers to a region far upstream of the Actuator Disc, the subscript 2 refers to the disc, and the subscript 3 refers to the far wake.

The conservation of momentum equation for a control volume is

$$\frac{\partial}{\partial t}\int_{C.V.} \rho\vec{u}dV + \int_{C.S.} \rho\vec{u}(\vec{u}\cdot\vec{n})dA = \int_{C.S.} -P\vec{n}dA + \int_{C.S.} \bar{\bar{\tau}}\cdot\vec{n}dA + \int_{C.V.} \rho\vec{g}dV \tag{3.24}$$

where P is the pressure, $\bar{\bar{\tau}}$ is the shear stress tensor, and $\vec{g}$ is the gravitational acceleration vector. When the ADM assumptions are applied, the equation simplifies to

$$\rho {u_3}^2 A_3 - \rho {u_1}^2 A_1 = A_2(p_2^+ - p_2^-) = F_A \tag{3.25}$$

where F_A is the force the actuator disc applies to the flow, p_2^- is the pressure on the front of the disc (upstream side), and p_2^+ is the pressure on the back of the disc (downstream side).

Since the flow is steady and incompressible, there are no frictional losses, and the flow is along a streamline, Bernoulli's Equation can be applied upstream and downstream of the actuator disc[20].

$$\frac{p_i}{\rho} + \frac{1}{2}{u_i}^2 + gz_i = constant \tag{3.26}$$

where g is gravitational acceleration, z is the vertical position, and the index i represents any position along the streamline. The following equations were derived by assuming there is no elevation change along the stream tube and applying Bernoulli's Equation to the upstream side of the actuator disc and the downstream side of the actuator disc.

$$p_1 + \frac{1}{2}\rho{u_1}^2 = p_2^- + \frac{1}{2}\rho u_2^2 \tag{3.27}$$

$$p_3 + \frac{1}{2}\rho{u_3}^2 = p_2^+ + \frac{1}{2}\rho u_2^2 \tag{3.28}$$

By subtracting Equation 3.28 from 3.27, applying the assumption that $p_1 \approx p_3$, and multiplying both sides by A_2, the equations become

$$\frac{1}{2}\rho A_2({u_1}^2 - {u_3}^2) = A_2(p_2^- - p_2^+) = -F_A \tag{3.29}$$

Next, Equations 3.25 and 3.29 are added, and Equation 3.23 is applied, resulting in

$$u_2 = \frac{1}{2}(u_1 + u_3). \tag{3.30}$$

At this point in the derivation it is helpful to define a new variable that represents the reduction of flow velocity caused by the actuator disc. This variable is called the Axial Induction Factor, defined as

$$a = \frac{u_1 - u_2}{u_1} \tag{3.31}$$

such that

$$\frac{u_2}{u_1} = 1 - a \tag{3.32}$$

$$\frac{u_3}{u_1} = 1 - 2a. \tag{3.33}$$

The power loss to the flowing fluid caused by the pressure drop across the actuator disc represents the power extracted at the disc (dissipated as a result of the hub) and it can be calculated as:

$$P = |F_A|u_2 = \frac{1}{2}\rho A_2({u_1}^2 - {u_3}^2)u_2 = \frac{1}{2}\rho u_1^3 A_2[4a(1-a)^2]. \tag{3.34}$$

The efficiency (η) of the actuator disc can be calculated by comparing P to the total available power in the flow, P_{total}

$$P_{total} = \frac{1}{2}\rho {u_1}^3 A_2 \tag{3.35}$$

$$\eta = 4a(1-a)^2. \tag{3.36}$$

The Porous Media Model in Fluent can be used to implement the ADM. The Porous Media Model adds a momentum source term into the governing momentum equation. The source term consists of a porous viscous loss term and a porous inertial loss term:

$$S = -\left(\frac{\mu}{\alpha}u_2 + C_2\frac{1}{2}\rho {u_2}^2\right) \tag{3.37}$$

where S is the source term, ρ is the density, α is the media permeability, and C_2 is the inertial resistance factor. The coefficients of $\frac{1}{\alpha}$ and C_2 are required inputs to the Porous Media Model. The relationship between the pressure drop across the porous media and the source term is

$$\Delta p = -S\Delta m \tag{3.38}$$

where Δm is equal to the thickness of the disc. The pressure drop calculated by Actuator Disc theory is

$$\Delta p = \frac{1}{2}\rho({u_1}^2 - {u_3}^2) \tag{3.39}$$

and by applying the definition of the axial induction factor it can be rewritten as

$$\Delta p = \frac{1}{2}\rho {u_2}^2 \frac{4a}{(1-a)}. \tag{3.40}$$

By equating the two expressions for Δp, Equations 3.38 and 3.40, it can be seen that

$$\Delta p = \frac{1}{2}\rho {u_2}^2 \frac{4a}{(1-a)} = \left(\frac{\mu}{\alpha}u_2 + C_2\frac{1}{2}\rho {u_2}^2\right)\Delta m. \tag{3.41}$$

The coefficients in front of the u_2 terms and the ${u_2}^2$ terms are compared, leading to the following set of equations

$$\frac{1}{\alpha} = 0 \tag{3.42}$$

$$C_2 = \frac{1}{\Delta m}\frac{4a}{(1-a)}. \tag{3.43}$$

The coefficients required for the Porous Media Model can be determined for any given value of the induction factor, a. Thus, the model requires a value of the induction factor, a, as an input.

The hub of a turbine obstructs the flow and results in power dissipation that can be associated to the drag on the hub. If the power dissipated by the hub is treated similarly to the power extracted by a turbine (P), a value of a can be calculated based on the amount of power that is expected to be dissipated in the wake of the hub. A relatively small amount of power is dissipated by the turbine's hub so the efficiency is assumed to be small, around 20%. A value of 20% efficiency provides a value of the

axial induction factor of $a = 0.055$. For $\Delta m = 0.035m$ the inertial resistance factor is $C_2 = 6.65159$. Using $C_2 = 6.65159$ and $1/\alpha = 0$, the Porous Media Model is applied to model the hub in the MHK turbine simulations in this thesis.

3.4 Open Channel Flow Theory

Open channel flow is perhaps the oldest subdiscipline within fluid mechanics, going back to irrigation canals in egyptian and roman times. It focuses on the motion of a liquid flowing under atmospheric pressure due to differences in elevation (potential energy). The flow is characterized by the height of the liquid (typically water) surface that is exposed to atmospheric pressure, see Figure 3.3. In open channel flow problems, the basic force balance is between friction on the (bottom and side) walls and differences in gravitational potential (or the hydrostatic pressure gradient induced by it) [20]. The frictional force is a result of a no slip boundary condition at the interface between the water and the channel walls. This no slip condition leads to a velocity gradient and subsequently a shear stress at the boundaries. The total frictional force on the fluid is equal to the shear stress multiplied by the total area of the solid boundaries. The hydrostatic pressure difference is created by the gravity and the difference in free surface height from the inlet to the outlet. Assuming that the channel has a constant cross section, the difference in height will have an associated difference in velocity between the inlet and the outlet: as the free surface height decreases, the cross section of the flow decreases and the velocity has to increase proportionally. This is necessary to conserve mass.

The important assumptions for a control volume analysis of open channel flow problems are:

- the free surface is a streamline
- the bottom has a no slip boundary condition

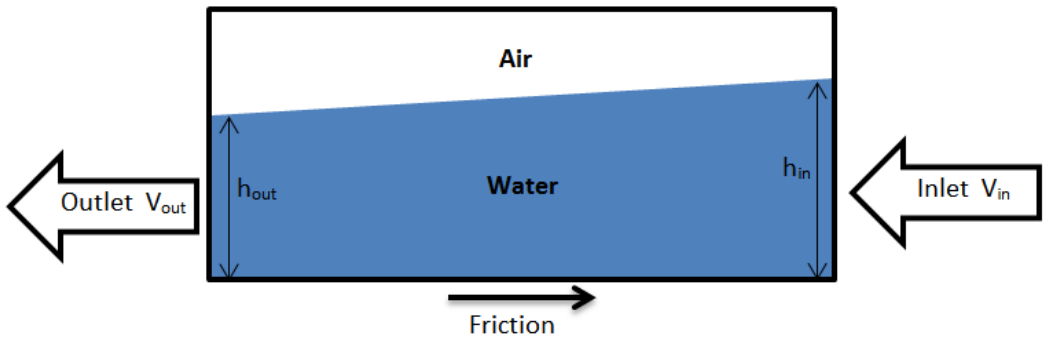

Figure 3.3: Schematic for open channel flow

- water is incompressible
- the flow is steady state
- constant channel width (cross section)

The sides of the domain can either be treated as a no-slip boundary if they represent the channel walls or they can be treated as symmetry planes if the water-way extends much further than the sides of the domain. For the purpose of this thesis, the sides are modeled as symmetry planes.

A control volume analysis is helpful to understand the dynamics and energetics of open channel flows. The general control volume equation for conservation of mass is given above, in Eq. 3.22. Through the application of the boundary conditions and simplifying assumptions previously made for open channel flow problems, this equation simplifies down to

$$u_{in}h_{in} = u_{out}h_{out}. \tag{3.44}$$

The control volume equation for the conservation of momentum laid out in Eq. 3.24 simplifies to the following for open channel flows:

$$\rho b u_{in} h_{in}(u_{in} - u_{out}) = \frac{\rho b g h_{in}^2}{2}\left(\left[\frac{u_{in}}{u_{out}}\right]^2 - 1\right) + A\tau_w \tag{3.45}$$

where A is the wetted area (the interface between the water and the channel walls), b is the channel width, and τ_w is the wall shear stress that is caused by the velocity gradient created by the no slip condition at the channel walls. The velocity profile for turbulent open channel flow is complex, with no exact solution for the mean velocity [20]. Calculating the shear stress exactly from derivatives of the velocity profile in the direction normal to the wall is ambiguous and prone to errors, so the shear stress is calculated using an empirical friction factor, f. This friction factor can be obtained from the classical Moody's diagram, or computed from an approximate expression, the Haaland Equation, that matches the experimental measurements in Moody's diagram and can be solved more readily without looking up in the chart.

$$f = \left(1.8 log \frac{Re_d}{6.9}\right)^{-2} \tag{3.46}$$

where Re_d is the Reynolds number based on the hydraulic diameter, D_h,

$$Re_d = \frac{\rho D_h u_{in}}{\mu} \tag{3.47}$$

$$D_h = \frac{4A_c}{P_w} \tag{3.48}$$

where μ is the viscosity, A_c is the cross sectional area of the channel, and P_w is the wetted perimeter. The wall shear stress, τ_w, is related to the friction factor by the following relationship

$$\tau_w = \frac{1}{2}\rho u_{in}^2 \frac{f}{4}. \tag{3.49}$$

If the inlet conditions, u_{in} and h_{in}, are known, Equation 3.45 only has one known, u_{out}, which can be solved for. Then, h_{out} can be calculated using Equation 3.44.

Equation 3.45 can be modified to account for the presence of a turbine. This is done by adding a thrust force into the calculation. The thrust force represents the pressure difference across the turbine and the frictional forces on the turbine.

$$\rho b u_{in} h_{in}(u_{in} - u_{out}) = \frac{\rho b g h_{in}^2}{2}\left(\left[\frac{u_{in}}{u_{out}}\right]^2 - 1\right) + A\tau_w + Thrust \tag{3.50}$$

Using the known inlet conditions, this theory can be used to compute the free surface elevation drop and compare it with the value predicted by numerical simulations for a given thrust value.

3.5 Numerical Modeling of Open Channel Flows

Modeling the effects of a free surface on the performance of an MHK turbine requires the combination of two separate models, a model for the turbine and a multiphase model for the free surface. The theory behind modeling a turbine was already discussed in Sections 3.2.1 and 3.3.

Prior to combining the two models, it is important to describe in detail the methodology used to model the free surface deformation without a turbine. The stability and accuracy of the free surface model was studied in a simple open channel flow, without the complexity added by the presence of a turbine. The issues that arose in the spatial discretization, convergence and accuracy of the free surface deformation could thus be resolved by comparison with simple channel flow solutions, in the absence of the MHK turbine.

There are several options for multiphase models that track the free surface location: Euler-Euler Approach, Volume of Fluid (VOF) model, Mixture Model, and the Eulerian-Lagragian Model. In the Euler-Euler Approach and the Mixture Model, the different phases are assumed to be interpenetrating continua and are primarily used for phases that are mixed together, like gas bubbles in a liquid or liquid droplets in a gas flow [41]. The Eulerian-Lagragian Model solves a set of momentum and continuity

equations for each phase, or for each discrete mass of a phase immersed in the other, continuous phase, making it the most complex and time consuming multiphase model [41]. The Volume of Fluid model tracks the average location of the interface between two phase, without tracking discrete fluid elements (as in the Eulerian-Lagragian). It is commonly used primarily for slug flows, stratified flows, and free-surface flows, where the complexity of the phase distribution is too high for the E-L model and the free surface location can be describe effectively by an average position without the specifics of the local deformation within a grid cell. Since the Volume of Fluid model was less computationally expensive than the Eulerian-Lagrangian Model, and tracks the fluid interfaces with adequate accuracy for the purpose of this study (surface tension is not important and only the average free surface location plays a role in the energetics of the open-channel flow), it was used for modeling MHK- free surface interactions in this thesis.

3.5.1 Volume of Fluid Theory

The Volume of Fluid (VOF) model was developed by C. W. Hirt and B. D. Nichols [42]. They postulated that problems involving free boundaries that underwent large deformations would be solved more easily using an Eulerian method than a Lagrangian method. They used the local volume fraction, Φ, to represent the fractional volume of a cell occupied by a specific fluid. The evolution of the variable is tracked in the numerical grid.

This method to implemented in ANSYS Fluent, introducing a variable for each phases' volume fraction, α_q , where q represents the index of each phase present in the flow. The volume fraction is calculated using a volume fraction continuity equation:

$$\frac{1}{\rho_q}\left[\frac{\partial}{\partial t}(\alpha_q\rho_q) + \bigtriangledown\cdot(\alpha_q\rho_q\vec{v_q}) = S_{\alpha_q} + \sum_{p=1}^{n}\dot{m}_{pq} - \dot{m}_{qp}\right] \tag{3.51}$$

where ρ_q is the density of the qth fluid, $\vec{v_q}$ is the velocity of the qth fluid, S_{α_q} is a

mass source term, $\dot{m}_{qp}$ is the mass transfer from fluid q to fluid p and $\dot{m}_{pq}$ is the mass transfer from fluid p to fluid q [41]. For open channel flows this equation can be simplified greatly because there is no mass source, no mass transfer between fluids, and the flow is incompressible. In this case, the continuity equation for the phase q simplifies down to [42]:

$$\frac{\partial}{\partial t}(\alpha_q \rho_q) + \bigtriangledown \cdot (\alpha_q \rho_q \vec{v_q}) = 0. \tag{3.52}$$

A single momentum equation is solved for the problem and the resulting velocity is applied to all phases within a grid cell.

$$\frac{\partial}{\partial t}(\rho \vec{v}) + \bigtriangledown \cdot (\rho \vec{v} \vec{v}) = - \bigtriangledown p + \bigtriangledown \cdot [\mu(\bigtriangledown \vec{v} + \bigtriangledown \vec{v}^T)] + \rho \vec{g} + \vec{F} \tag{3.53}$$

where p is the pressure, μ is the viscosity, g is gravitational acceleration, and F are external forces. The material properties of the fluid inside each cell are calculated using the local value of the volume fraction and the material properties of each individual fluid,

$$\rho = \sum \alpha_q \rho_q \tag{3.54}$$

$$\mu = \sum \alpha_q \mu_q. \tag{3.55}$$

3.5.2 Initial Conditions

Open channel flow problems require a very specific set of initial conditions and boundary conditions that if chosen incorrectly, will produce unphysical results. The VOF model is very sensitive to the initial conditions used to initialize the problem [43]. For example, the volume fraction of water must be set as 1 in the portion of the domain that will likely be occupied by water. This is accomplished by marking the region of water in the Region Adaption dialog box and setting the volume fraction of water in that region as 1, see Figures 3.4 and 3.5. If this is not done, the water will simply

enter the domain from the inlet and cascade to the bottom of the channel, because there is no hydrostatic pressure present throughout the domain to maintain the water height at the inlet, creating instabilities.

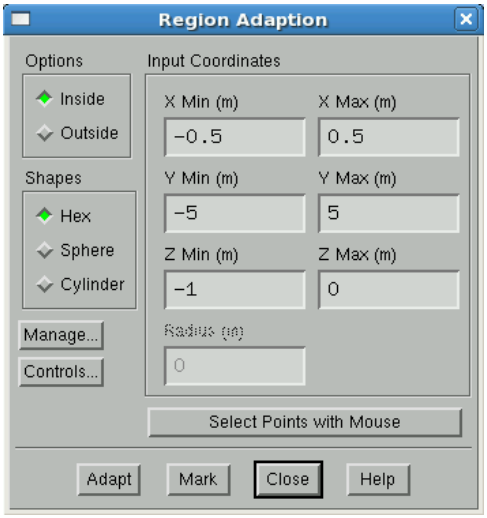

Figure 3.4: The Region Adaption dialog box is used to specify the initial water region

3.5.3 Boundary Conditions

There are several different boundary conditions that can be used for the top, inlet, and outlet of an open channel flow domain.

The Volume of Fluid implementation in Fluent has an open channel flow option that allows the user to select boundary conditions specifically designed for open channel flow simulations. In order to use those boundary conditions, the water inlet and the air inlet must be combined into one multiphase inlet, and the water outlet and air outlet must be combined into one multiphase outlet. Once this is done, the inlet conditions available for the open channel flow option are a mass flow rate inlet and a pressure inlet. The mass flow rate inlet requires the user to specify the mass flow rate of air, the mass flow rate of water, the channel's bottom height, and the free surface

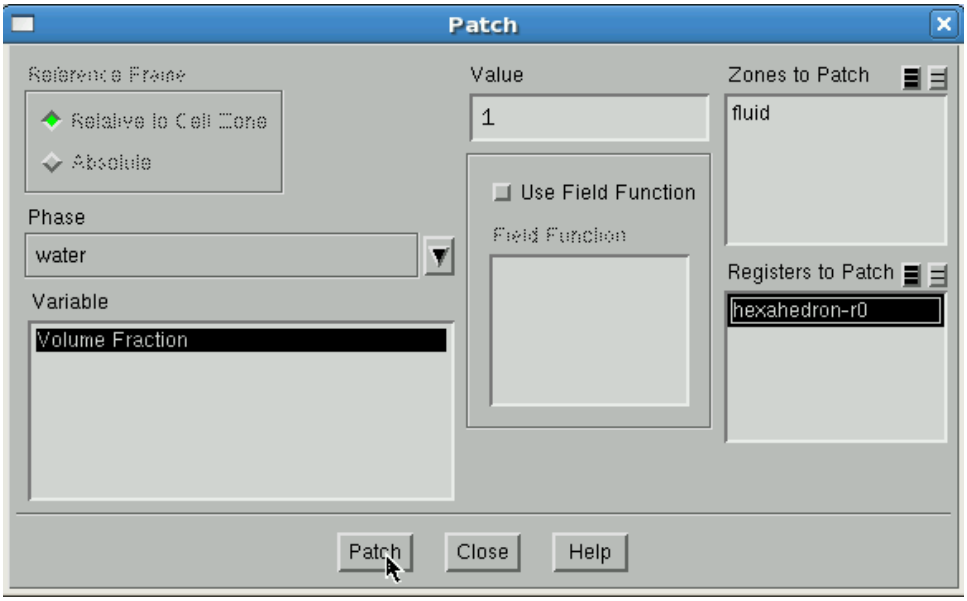

Figure 3.5: Patch Dialog box is used to assign the volume fraction of water as 1 in a specified region

height. For the pressure inlet, the user must specify the velocity of the water, the channel's bottom height, and the free surface height, see Figure 3.6.

The mass flow rate boundary condition brakes the inlet into two separate mass flow rate inlets, one for water and one for air, using the free surface as the boundary between the two. The water portion of the inlet applies the mass flow rate of water specified by the user, and the air portion of the inlet applies the mass flow rate of air specified by the user. The free surface height at the inlet is allowed to change as the simulation progresses to ensure mass and momentum are conserved. Therefore, the free surface height that the user specifies is only used as an initial guess.

The pressure inlet boundary condition is more complicated. The user must specify the bottom height, the free surface height, and the velocity at the inlet. These values are used to calculate the total pressure p_o at the inlet. The total pressure can be broken into two parts, the dynamic pressure q, and the static pressure p_s, where

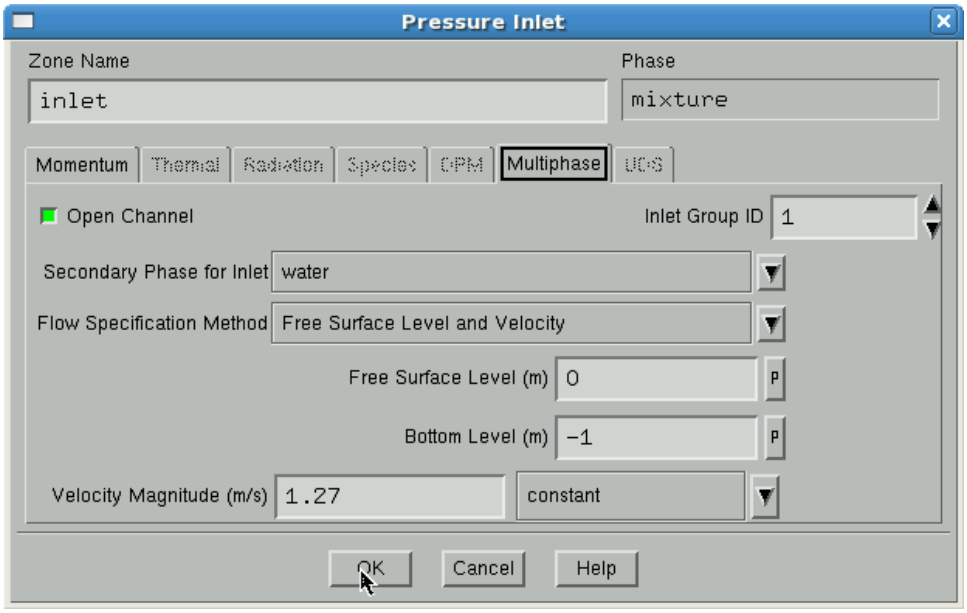

Figure 3.6: Dialog Box for Open Channel Flow option Pressure Inlet

$$p_o = q + p_s \tag{3.56}$$

$$q = \frac{\rho - \rho_0}{2} V^2 \tag{3.57}$$

$$p_s = (\rho - \rho_0)|\vec{g}|((\hat{g} \cdot \vec{b}) + y_{local}) \tag{3.58}$$

ρ is the density of the mixture in a cell, ρ_0 is the reference density (which is the density of the lightest fluid), V is the velocity magnitude, $\vec{g}$ is the gravity vector, $\hat{g}$ is the unit vector of gravity, $\vec{b}$ is the position vector of the centroid of a cell with respect to a reference location, and y_{local} is the vertical distance from the free surface to the reference location. This creates a hydrostatic pressure profile at the inlet for the water. The speed of the water is set in the dialog box seen in Figure 3.6. Similar to the mass flow rate boundary condition, the free surface level is allowed to change in order to conserve mass and momentum.

Another inlet condition was manually created. The intent was to prescribe a velocity

to the water but not to the air. This was done by splitting the inlet into two separate inlets, one specifically for water, and one specifically for air. A mass flow inlet for the water inlet and a pressure inlet for the air inlet were then assigned. One issue that arises with this boundary condition is the free surface height at the inlet is not allowed to fluctuate.

The options considered for the outlet boundary condition were different variations of a pressure outlet. For pressure outlets, the open channel flow option for the VOF model provides two different methods for specifying pressure. One is by prescribing the bottom height and the free surface height at the outlet in a similar fashion to what was done in the pressure inlet boundary condition. The other is using the pressure from a neighboring cell as the pressure at the boundary. A third method for pressure specification was also applied, writing a User Defined Function (UDF) to prescribe a hydrostatic pressure profile at the outlet. This method was successfully used in a similar previous study [18].

For the top boundary, a pressure inlet, pressure outlet, or symmetry boundary can be applied.

Given the significant uncertainty in exact meaning of certain values and variables used in the boundary conditions implemented for VOF and open channel flow, different simulations were conducted using combinations of these inlet and outlet conditions. This provided control over what were the exact constraints imposed by the boundary conditions used in the "production" runs in this thesis. The general findings of those simulations were;

- The mass flow rate inlet and pressure inlet open channel flow boundary conditions allowed for fluctuations in the free surface height. This provided an accurate free surface elevation change when paired with certain outlet conditions, but the velocity profiles in air were unphysical.

- In simulations with two separate inlets, one for air and one for water, the free

surface height at the inlet was fixed, so the free surface did not have a constant downward slope as would be expected by theory. However, since the air inlet was a pressure inlet (not assigned a velocity or mass flow rate) the velocity in the air most accurately represented what would be expected physically.

- When using a UDF for the outlet pressure specification method, the outlet free surface height was fixed and regardless of the inlet boundary condition, the inlet free surface height was also fixed, therefore no equilibrium could be reached to balance the momentum lost to friction on the bottom of the channel. This produced inaccurate modeling of the free surface.

- Simulations that used the neighboring cell for the pressure specification method exhibited convergence problems. The neighboring cell boundary condition allowed fluctuations in the free surface height at the outlet. When combined with an open channel flow inlet condition, the entire free surface height would change, such that it no longer represented the flow being modeled.

- Simulations using the free surface height and the bottom height in the pressure specification method for the pressure outlet fixed the free surface height at the outlet. When combined with the open channel flow inlet conditions, this boundary condition produced a free surface with a constant slope that was fixed at the outlet, similar to what is expected of open channel flows.

- When the symmetry boundary condition was applied to the top boundary, the air moved at a constant velocity throughout the entire domain, which is not physical. However, it has negligible effects on the free surface behavior and the turbine's performance.

- When the pressure inlet and pressure outlet boundary conditions were applied to the top boundary and paired with certain velocity inlet and outlet boundary

conditions, they provided a velocity gradient in the air similar to what would be expected for an open channel flow. The air had the same velocity as the water at the free surface, and the velocity decayed further away from the free surface. However, the inlet and outlet velocity boundary conditions required to produce that velocity gradient in the air did not accurately model the free surface behavior.

Since the purpose of this study is to determine how a free surface affects MHK turbine behavior, it was decided that proper modeling of the free surface was more important than proper modeling of the air's velocity profile, because the air's velocity far above the free surface has negligible effects on the turbine performance.

It was concluded that the most appropriate boundary conditions for simulating open channel flows were symmetry for the top, Pressure Inlet with the Open Channel Flow Option for the inlet, and Pressure Outlet with the Open Channel Flow Option for the outlet. The pressure specification method for the outlet was the free surface height and the bottom height. The symmetry boundary condition was selected for the top boundary because when combined with certain velocity inlet and outlet conditions, it accurately modeled the change in the free surface height. Also, the symmetry boundary condition produced better convergence in a simulation of a 10 meter long test channel, see Table 3.1. Even though the air mass flow rate boundary condition performed well, it was not desirable to guess the mass flow rate of the air, so the pressure inlet was selected.

Table 3.1: Convergence for different boundary conditions applied to the top of the domain

Air-side Top Boundary Condition	Number of Iterations	Convergence
Symmetry	4563	$1.0e-07$
Pressure Inlet	4563	$1.0e-03$
Pressure Outlet	4563	$1.0e-03$

Chapter 4

NUMERICAL MODELING

4.1 Meshing

The process to setup the numerical simulations that provides us the insight into the flow dynamics studied in this thesis, starts with defining the flow domain and creating a spatial discretization in which the equations of motion can be numerically solved. The domain is divided into smaller volumes called cells or elements, such that the flow variables take discrete values inside the cells, or at the surfaces between the cells (in case of fluxes). The flow domain used for in this thesis can be seen in Figure 4.1, including the location of the free surface and of the MHK turbine. The CFD simulations take the governing differential equations, convert them to equations in differences (with discrete instead of continuous variables) and solve them in the small control volumes that are the grid cells.

The accuracy of the solution is related to the number of mesh cells. Normally, it is a direct relationship, more cells lead to a more accurate solution. However, an increase in the number of cells also increases the computational time. The key to an efficient and accurate numerical discretization of the flow domain is to balance the need for higher spatial resolution in regions with large variations in the fluid variables (high gradients) with lower resolution in regions where the fluid variables are evolving smoothly (low values of the gradients). In the numerical simulations used in this thesis, there were always two regions of the flow that required a fine mesh: the turbine wake, and the free surface, see Figure 4.2. The most delicate step in the preprocessing of the numerical simulations is to generate a high quality mesh, with sufficient resolution (high grid count) in the regions were the flow solution requires

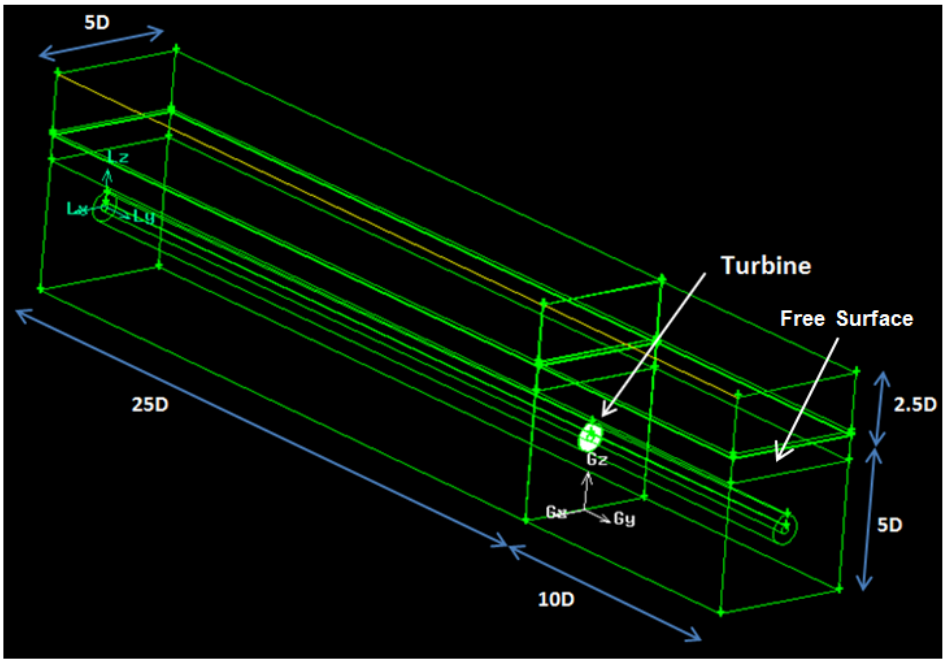

Figure 4.1: Domain used for modeling free surface effects on an MHK turbine where D is the diameter of the turbine.

them, and a smooth transition between the fine mesh regions and the coarse mesh in the rest of the domain [38].

The turbine wake required grid refinement because of the large variations that the flow experiences as it crosses the turbine rotor swept disc, and then as it returns to a state of equilibrium with the free stream flow. The free surface required a very fine mesh to capture the free surface fluctuations that occur as the flow accelerates as it moves around the turbine disc and interacts with the free surface. The VOF uses a diffuse interface, with the free surface location computed across a small number of grid cells. If the numerical thickness of the free surface, the region where the liquid volume fraction, Φ, evolves from 1 (pure liquid) to 0 (pure gas), is too large, numerical instabilities ensue and the representation of the free surface ($\Phi = 0.5$) does not behave in a physical manner (among other problems, mass is not conserved). For

all the simulations in this thesis (Reynolds number= 5×10^5 - 2×10^6), the results of which are presented in Section 5.1, the cell size near the free surface in the plane normal to the flow had to be less than 0.1m to accurately predict the decay in free surface height due to the friction on the channel floor. If the mesh size was larger, the free surface would not behave as theory predicted and mass was not conserved, see Figure 4.3.

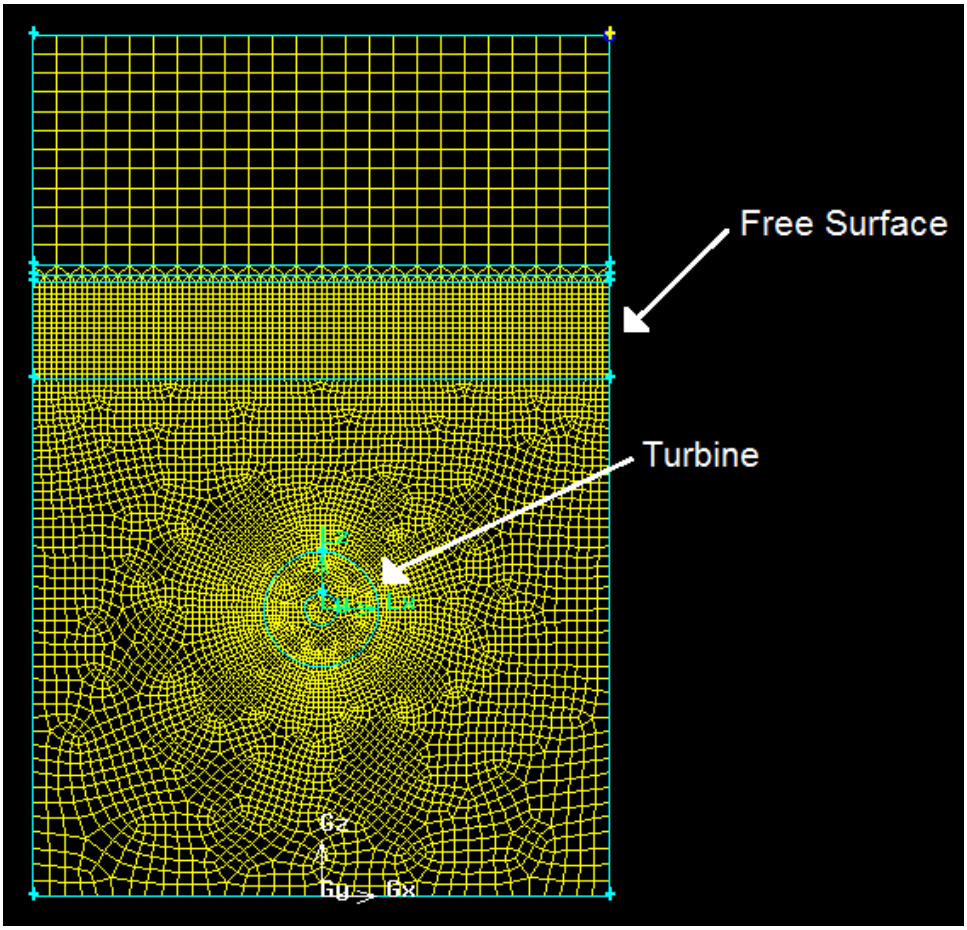

Figure 4.2: The mesh of the domain on a plane normal to the flow direction

A fine structured rectangular mesh was the preferred meshing scheme near the free surface. This allowed for the resolution of small variations in the free surface height.

The region of the domain comprising of air was not subject to large flow variations, so a coarse mesh was used to help minimize the number of cells in the simulation. An unstructured triangular pave mesh was used to transition from the coarse mesh on the air side to the fine mesh at the free surface. The unstructured mesh in the transitional region had a skewness below 0.24. Skewness is a measure of mesh quality that ranges between 0 and 1. Generally it is good practice to keep the maximum skewness for any element in a mesh below 0.8. The meshes used in numerical simulations described in this thesis all had skewness values below 0.55.

The boundary layer that developed at the bottom of the channel could not realistically captured in this simulation, and the results did not depend on the velocity gradient in that part of the domain being realistic, therefore a coarse mesh was used to reduce the size of the computations, in memory and CPU requirements, reserving the computing power available to where it had the most impact on the physics studied. An unstructured mesh was used in the transition region between the turbine, where the mesh was quite fine, and the bottom, where it was coarse. A sizing function was applied to control the cell growth in the mesh, between the turbine disc and the bottom wall.

4.2 Numerical Settings

There were numerous simulations performed in the course of this thesis. The following is a description of the methodology used for the numerical modeling. Several of the values such as inlet velocity, turbine rotational speed, turbine vertical position, and turbulence length scales, were varied based on the size of the turbine, the depth and width of the channel, etc., to investigate the effect of different non-dimensional parameters, such as the Tip Speed Ratio, the Reynolds number, the turbine depth to diameter ratio, the blockage ratio, etc. We used a Pressure-Based, Steady State Solver with an Absolute Velocity Formulation as settings in all simulations. The solution was run to convergence at approximately 5×10^{-6}, see Section 4.3.2.

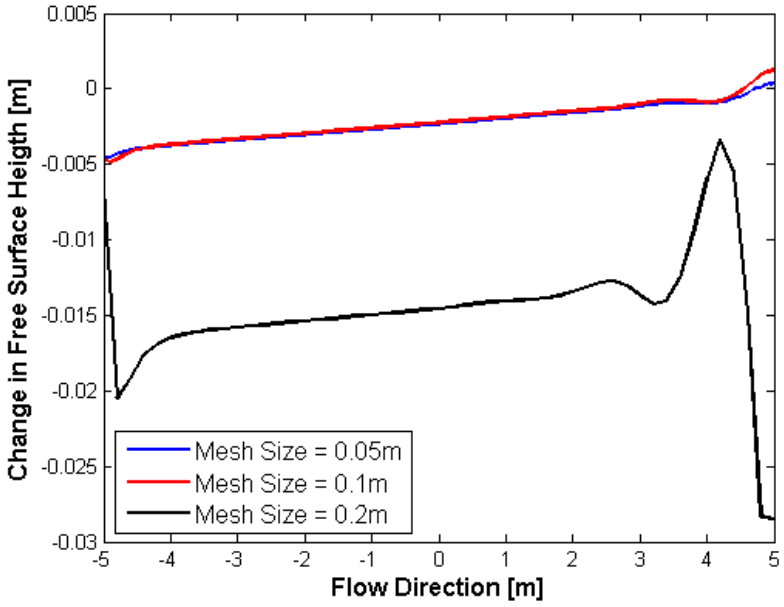

Figure 4.3: Spurious free surface fluctuations near the domain inlet and outlet, for differing mesh sizes. The channel was 10m long, 1m deep, and 1m wide, and flow was from right to left. The flow velocity was 1.25m/s.

4.2.1 Numerical Models

The modeling of the interaction of MHK turbines with the water free surface requires selection of a turbulence model to provide mathematical closure for the RANS equation, a multiphase flow model to characterize the free surface deformation and its effect on the MHK turbines, and a model to represent the energy extraction and drag force induced by the MHK turbines on the flow.

As previously discussed in Section 3.1.2, the Reynolds stresses must be modeled to simulate turbulent flows through the RANS equations. The turbulence model selected for the simulations in this thesis was the $k-\epsilon$ turbulence model. Although there are several adjustable coefficients in the $k-\epsilon$ turbulence model, the default values suggested by the CFD commercial software used (ANSYS Fluent, Cannonsburg,

PA) were used. It is possible that those coefficients can be fine-tuned for the specific conditions in MHK turbine flows, but that would require detailed laboratory experiments, at a scale representative of the turbulence in this application ($Re \approx 10^6 - 10^7$), which is currently unavailable in the open literature. While more refined coefficients may modify some of the results in this thesis quantitatively, typically by a few percentage points, the qualitative results that characterize the physics of these flows will remain relevant.

The dialog box shown in Figure 4.4 presents the input for the numerical implementation of the multiphase model selected for use in this thesis, the Volume of Fluid (VOF) model. Section 3.5 includes the results from preliminary simulations run for the purpose of understanding the features of the VOF model and how to best use them for the investigation of MHK turbine-free surface interactions. The setting selected for the model can be seen in Table 4.1.

Table 4.1: Volume of Fluid Settings

Number of Phases	2
Scheme	Implicit
Body Force Formulation	Implicit Body Force
Options	Open Channel Flow

The turbine model selected was the Virtual Blade Model (VBM). For a full explanation of VBM refer to Section 3.2.1 and reference [2]. The dialog box for VBM can be seen in Figure 4.5. The setting for the dialog box can be seen in Table 4.2. The turbine modeled was the DOE Reference Model 1 [44]. It is two-bladed rotor and operates at an optimal tip speed ratio (TSR) of 7.

$$TSR = \frac{\omega R}{U} \tag{4.1}$$

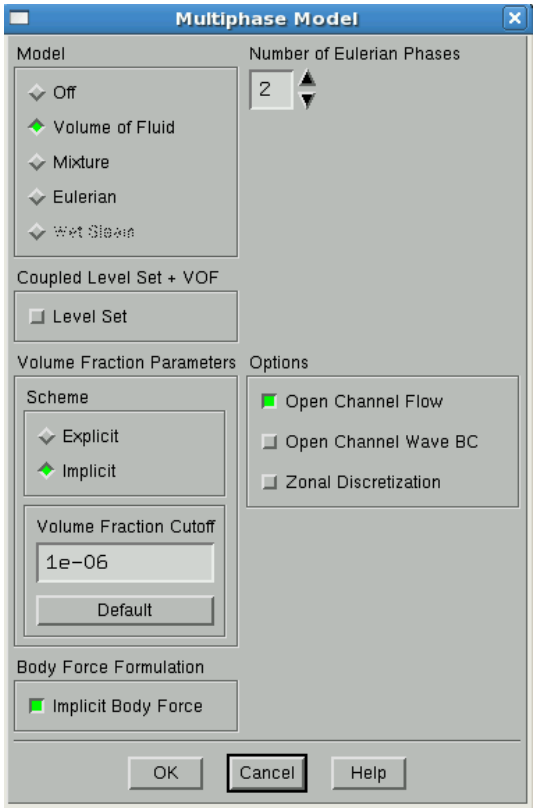

Figure 4.4: Volume of Fluid Dialog Box

where ω is the angular velocity in $[rads/s]$, R is the turbine radius, and U is the incident velocity. The TSR used for the numerical model was 6.33. This matched the TSR used in previous numerical models of the DOE Reference Model 1 performed by Tessier and Tomasini [45] at the University of Washington. The simulations discussed in this thesis were performed at an approximate scale of 20:1. The spatial resolution required to accurately represent the dynamics of the free surface was too fine to represent a full scale physical domain typical of a utility scale turbine. Thus, the simulations in this thesis (V=1-2 m/s, D=0.5-1 m, turbine depth=0.75 m-2.5 m) represent a small scale power generation turbine or a scaled-down utility turbine in a large scale flume.

Table 4.2: VBM Settings

Number of Blades	2
Rotor Radius [m]	0.5 or 0.25
Rotor Speed [rpm]	214 (Radius = 0.5m), 298 (Radius = 0.25m)
Tip Effect	96%
Pitch Angle [deg]	0
Bank Angle [deg]	90
Collective Pitch [deg]	0
Rotor Disc Origin X [m]	0
Rotor Disc Origin Y [m]	0
Rotor Disc Origin Z [m]	depends on hub depth

The tip effect accounts for the three dimensional nature of the flow near the tip of the blade. VBM calculates the lift and drag forces assuming two dimensional flow, which does not properly model the region near the tip. A tip effect of 96% means that for all sections of the blade covering, up to and including, 96% of the span of the blade, VBM calculates the lift and drag forces with the lift and drag coefficients from the look-up tables. For the remaining section or sections of the blade closest to the tip, only drag forces are calculated. This assumes that minimal lift is generated by the three dimensional flow near the tip.

The vertical position of the Rotor Disc Origin, or $Z(m)$, depends on the depth of the turbine. This was varied for different simulations to investigate the effect of the depth-to-rotor-diameter ratio. The Rotor Speed was varied to maintain constant TSR for different turbine diameters. The Rotor Speed for a turbine operating in a free stream velocity of 1.25 m/s was 214 rpm for the 0.5 m radius turbine, or 298 rpm for the 0.25 m radius turbine. Blade Flapping was neglected and all of the values remained

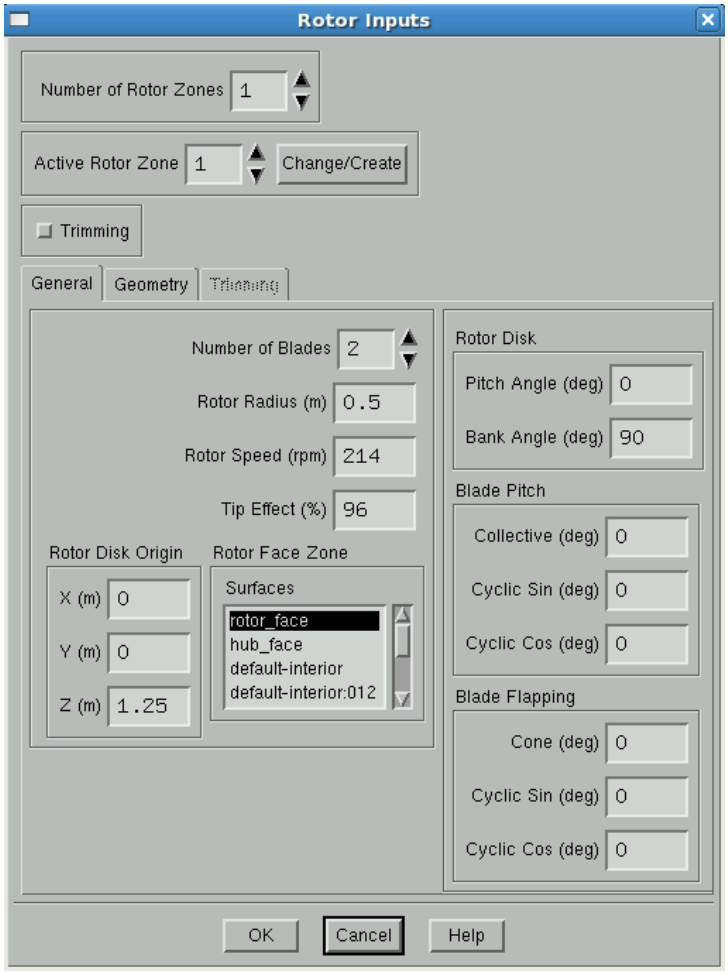

Figure 4.5: Virtual Blade Model Dialog Box

zero since the rotor blades were considered rigid. The Rotor Disc Bank Angle and the Pitch Angle describes the rotors alignment relative to the coordinate system, see Figure 4.6. Since the flow was in the -Y direction the Rotor Disc Pitch Angle was 0° and the Rotor Disc Bank Angle was 90°.

VBM requires some of the blade's geometry as an input to the model, Table 4.3 shows the necessary data. The blade was divided into 20 blade sections (or blade elements) which correspond to the Section Numbers. A look-up table for C_L and C_D as a function of the angle of attack and Reynolds number, was also provided for each

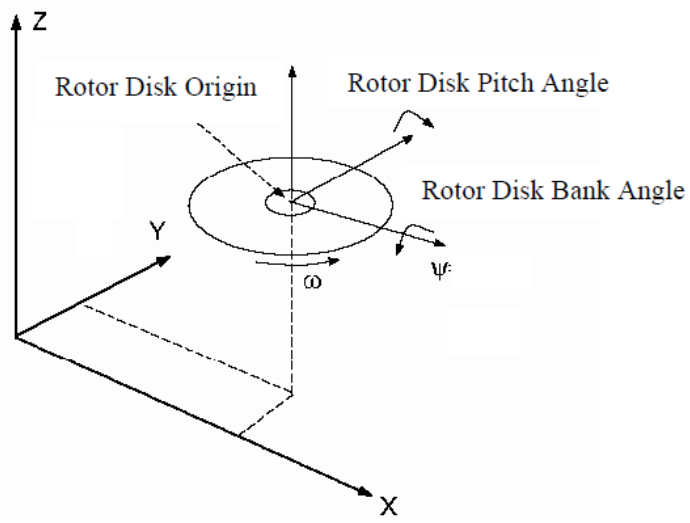

Figure 4.6: Rotor Disc Alignment Definition [2]

blade element. This table was created using the results of a SRF model of the DOE Reference Model 1 [45]

4.2.2 Cell Conditions

Two phases were used in the simulations presented in this thesis. The lightest fluid, Air, was required to be assigned as the primary phase and water was assigned as the secondary phase [43]. The settings for the model used were: a gravitational acceleration of $-9.81m/s$ in the z-direction, an operating density of $1.225kg/m^3$, and a reference pressure location of about one diameter distance above the free surface. The operating density is the density of the lightest fluid, and is required for open channel flow problems because it is used as the reference density in the Open Channel Flow Boundary Conditions, see Equations 3.57 and 3.58. The reference pressure is taken to be atmospheric pressure so the reference pressure location must be in a location with atmospheric pressure, i.e. the air.

The cell condition assigned to the hub region was a porous zone as discussed is Section

Table 4.3: Required Geometry Inputs for VBM where D is the Turbine Diameter

Section Number	Radius(r/R)	Chord(m)	Twist(deg)
1	0.280	0.085D	12.86
2	0.295	0.083D	11.54
3	0.325	0.081D	10.44
4	0.355	0.079D	9.50
5	0.385	0.077D	8.71
6	0.415	0.075D	8.02
7	0.445	0.073D	7.43
8	0.475	0.070D	6.91
9	0.505	0.068D	6.45
10	0.535	0.066D	6.04
11	0.565	0.064D	5.68
12	0.595	0.062D	5.35
13	0.655	0.057D	4.77
14	0.715	0.053D	4.26
15	0.775	0.048D	3.80
16	0.835	0.044D	3.35
17	0.895	0.039D	2.90
18	0.925	0.036D	2.67
19	0.955	0.034D	2.43
20	0.985	0.031D	2.18

3.3. The dialog box can be seen in Figure 4.7. The cell condition for the rotor was a source term. The source term represents the force of the turbine on the fluid. The force was calculated by VBM.

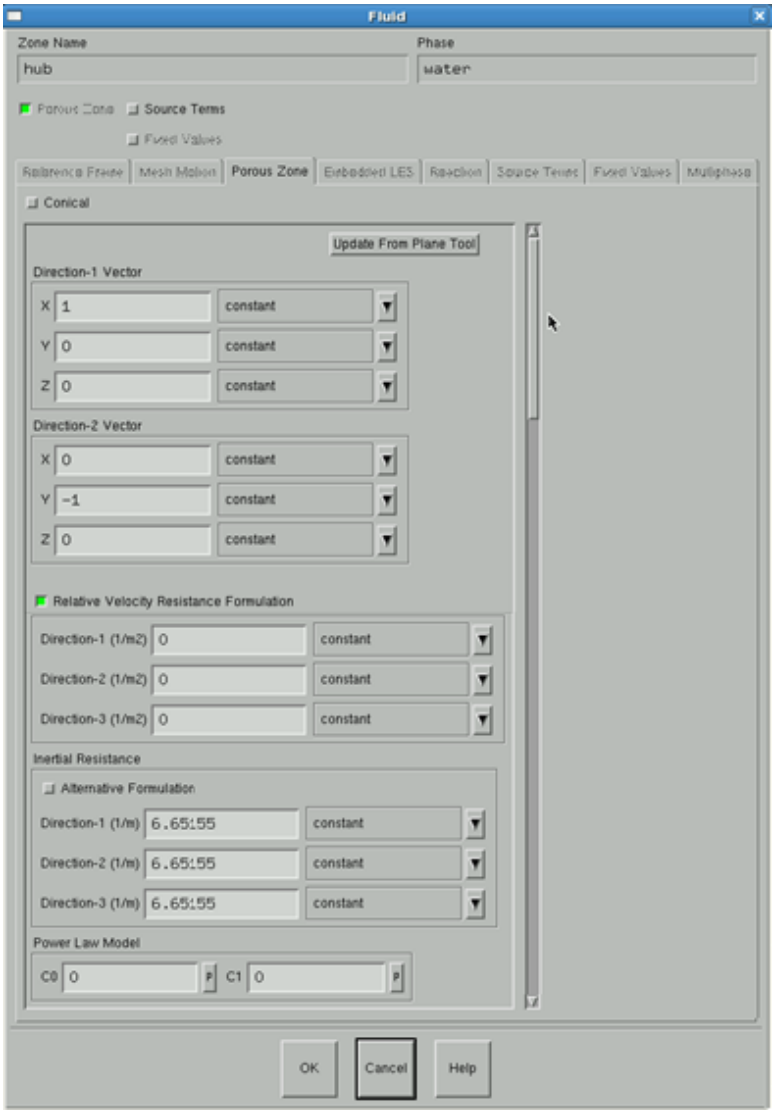

Figure 4.7: Porous Zone Dialog Box

4.2.3 Boundary Conditions

The boundary conditions used for the simulations in this thesis can be seen in Table 4.4, where D is the turbine diameter. The justification for the selection of these boundary conditions is provided by Section 3.5.3.

Table 4.4: Boundary Conditions

Sides	**Symmetry**	
Top	**Symmetry**	
Outlet	**Pressure Outlet**	
	Free Surface Height	3D, 4D, or 5D
	Turbulent Length Scale	D/10 [m]
	Turbulent Intensity	1 %
Inlet	**Pressure Inlet**	
	Free Surface Height	3D, 4D, or 5D
	Turbulent Length Scale	D/10 [m]
	Turbulent Intensity	5%
	Velocity	1.25, 1.77 [m/s]
Bottom	**No Slip Wall**	

The Turbulent Length Scale, l, used in the inlet and outlet conditions is a physical quantity related to the size of the larger eddies present in the flow [30]. The value for l is representative of the properties of the turbulence in the flow being modeled.
For open channel flow problems l is commonly taken to be

$$l = 0.07 D_h \tag{4.2}$$

where D_h is the hydraulic diameter, Equation 3.48 [46]. The wetted perimeter, P_w, was calculated two ways for the open channel flows studied in this thesis. The first

way was to set P_w as the width of the bottom of the channel with the sides modeled as symmetry boundaries. The second way was to set P_w equal to the height of the sides of the channel plus the width of the bottom, which was the length exposed to water. Given these two definitions for P_w and the different channel depths used in the simulations, l can have a minimum value of 0.446D or a maximum value of 1.4D where D is the diameter of the turbine.

Previous simulations of MHK turbine flows conducted in our laboratory used the chord length of the turbine for the turbulent length scale so that it accurately matched experimental data [27]. The chord length for the DOE Reference Model 1 is 0.085D. It was therefore important to determine which turbulent length scale would most accurately model the physics of an MHK turbine in an open channel. Several different simulations were conducted with different turbulent length scales ranging from 0.05D to 1D. The velocity profiles in the region near the turbine and the coefficient of power for the turbine in each simulation were examined, see Figure 4.8 and Table 4.5.

Table 4.5: Coefficient of Power for Different Turbulent Length Scales

Turbulent Length Scale	Coefficient of Power
1D	0.474
0.5D	0.441
0.1D	0.403
0.05D	0.392

The turbine performance, C_p values, obtained for the different turbulent length scales prescribed at the boundaries were compatible with the range of C_p values calculated by Tessier and Tomasini [45] for the full size turbine, in the absence of a free surface. The velocity profiles for the full size turbine [45] showed flow speeds directly downstream of the hub of the turbine close to the freestream value, suggesting that the correct value of

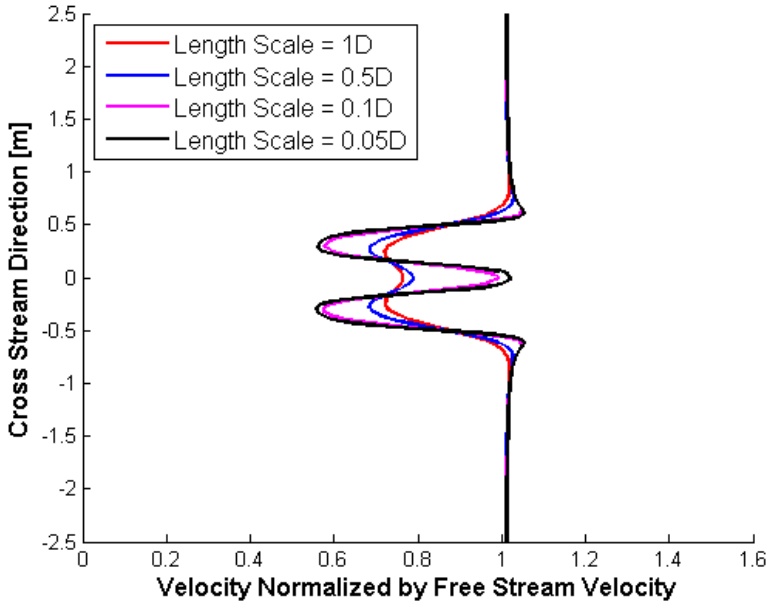

Figure 4.8: The velocity profiles at 1/4D downstream of the turbine for different turbulent length scales.

the turbulent length scale in the simulations in this thesis should be $0.05D - 0.1D$. To further support this conclusion, the change in available power between the inlet and a section three diameters downstream of the turbine was calculated for each simulation using the respective velocity profiles. This change in power is a combination of the power extracted by the turbine and the mean kinetic energy converted to turbulent kinetic energy by the turbine, see Table 4.6. In the case of the larger turbulent length scale, it appeared that none of the mean kinetic energy was transferred to turbulence, which is unphysical. In the case of the smaller turbulent length scales, an appreciable amount of the mean kinetic energy was converted into turbulence. Therefore, the use of the smaller range for the turbulent length scale prescribed at the boundaries seemed more accurate.

To decide between the two small length scales, the turbulent kinetic energy (k) and

Table 4.6: The power extracted by the turbine computed by VBM compared to the change in power calculated by applying conservation of energy to a control volume around the turbine

Turbulent Length Scale	Power Extracted [w]	Power Loss [w]
1D	326.7	319.9
0.05D	270.2	358.8

the turbulent dissipation rate (ϵ) were examined. The values for k and ϵ relate to the turbulent intensity, I, and the turbulent length scale, l, as follows:

$$k = \frac{3}{2}(u_{avg}I)^2 \tag{4.3}$$

$$\epsilon = C_\mu{}^{3/4}\frac{k^{3/2}}{l} \tag{4.4}$$

where u_{avg} is the mean flow velocity, and C_μ is a modeling constant. k is not affected by the l, and ϵ is inversely proportional to l. The length scale of 0.1D was chosen because it minimized the dissipation rate allowing the inlet turbulence to persist further down the channel, as should happen in a real application where the turbulence is in statistically stationary state: the turbulent production at the bottom wall and from large scale rotation and topographic effects balances the dissipation at the smallest scales.

A value of the turbulent intensity of 5% was selected for the inlet boundary condition matching previous work with the DOE reference model 1 done at the UW [45] and at NREL [44]. However, values of turbulence intensity up to 10% have been measured at two potential MHK turbine sites in the Puget Sound, [47]. Simulations performed with values of turbulence intensity of 5% and 10% showed a difference in power produced was approximately 2%. Thus, it was determined that fixing the value of

turbulence intensity at 5% for all simulations in this thesis would eliminate a source of uncertainty while maintaining the parameter range well grounded at realistic values for the ultimate application.

The $k-\epsilon$ turbulence model requires the user to specify the turbulent length scale and the turbulent intensity for reverse flow through an outlet. In the simulations of this thesis there was no reverse flow, however since the values were required, the length scale for the outlet was assigned the same length scale as the inlet, and the turbulent intensity was assigned as 1%. A turbulent intensity of 1% was the approximate turbulent intensity near the outlet in the numerical simulations.

4.2.4 Solution Methods

Table 4.7 shows the Solution Methods and Solution Controls used in this thesis. Several of the standard Solution Control Values were changed to aid in the convergence of the solution as suggested by Section 29.3.2.1 of the ANSYS 14.0 User's Guide [48].

4.3 Solution

4.3.1 Solution Initialization

Problems solved using VOF require a relatively accurate solution initialization in order to obtain convergence. This was done by using the Standard Initialization Method with the initialization variables computed from the Inlet. Once the solution was initialized, a region of water was patched into the domain, see Section 3.5.2 for details. Table 4.8 provides the necessary inputs for the region, where D is the diameter of the turbine.

4.3.2 Convergence

The CFD solver used in the simulations presented in this thesis follows an iterative process. The convergence of the iterative process can be monitored using residuals.

Table 4.7: Solution Methods and Solution Controls

Turbulent Model	Standard k-ϵ
Pressure-Velocity Coupling	SIMPLE
Discretization of Gradient	Green-Gauss Node Based
Discretization of Pressure	PRESTO!
Discretization of Momentum	Second Order Upwind
Volume Fraction	QUICK
Discretization of Turbulent Kinetic Energy	Second Order Upwind
Discretization of Dissipation Rate	Second Order Upwind
Pressure Under-relaxation Factor	0.3
Density Under-relaxation Factor	1
Body Forces Under-relaxation Factor	1
Momentum Under-relaxation Factor	0.5
Volume Fraction Under-relaxation Factor	0.5
Turbulent Kinetic Energy Under-relaxation Factor	0.5
Turbulent Dissipation Rate Under-relaxation Factor	0.5
Turbulent Viscosity Under-relaxation Factor	1

The residuals are measures of the imbalance between the two sides of each conservation equation. As the solution converges the left hand side of a conservation equation should approximate the exact same value as the right hand side of that equation. Due to computer round off error, the residuals may approach zero but never reach it. Once the solution has converged to where the residuals are the same order of magnitude as the round-off error, the residuals will "level-out" [48] and the simulation is said to be converged to "machine zero".

It is not always necessary to converge to where the residuals reach the machine error.

Table 4.8: Region Adaption Input

X Min (m)	-2.5D, -3.125D, -4.17D
X Max (m)	2.5D, 3.125D, 4.17D
Y Min (m)	-25D
Y Max (m)	10D
Z Min (m)	0
Z Max (m)	5D, 4D, 3D

For example, the properties of interest for a MHK turbine, in a domain without a free surface, converge well at residual levels of approximately 1×10^{-3}, see Figure 4.9. Therefore, continuing the simulation until the residuals converge to machine error would not improve the accuracy of the results and would, therefore, be a waste of computational time. It is important to realize that not all simulations converge at the same residual level, and not all properties converge to the same level. When modeling MHK turbines in a flow close to the free surface, the turbine power converged when the residuals were below 1×10^{-3} while the free surface vertical position did not converge until the residuals were below 5×10^{-6}, see Figures 4.10, 4.11, and 4.12. For the purposes of this thesis, simulations without a free surface were considered converged when the residuals were less than 1×10^{-3} and simulations with a free surface were considered converged when the residuals were less than 5×10^{-6}.

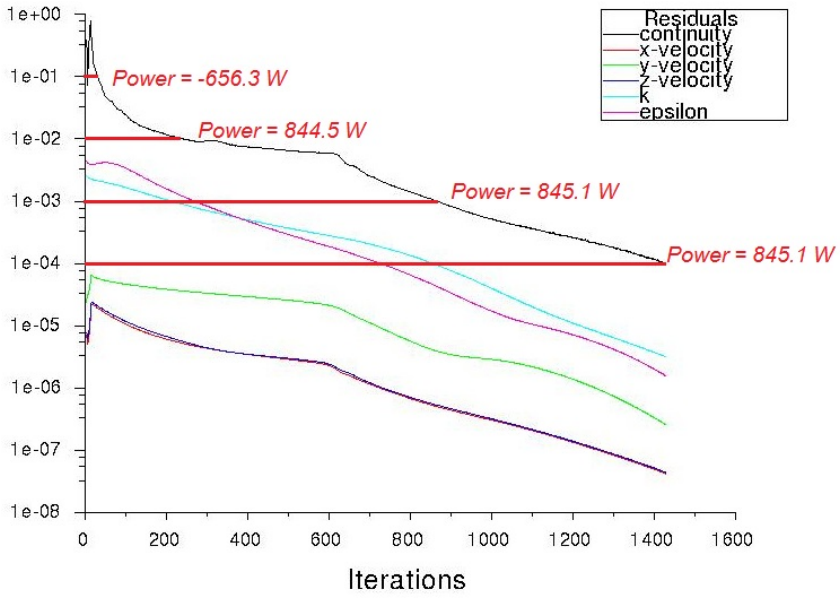

Figure 4.9: Convergence of power for a MHK turbine without a free surface

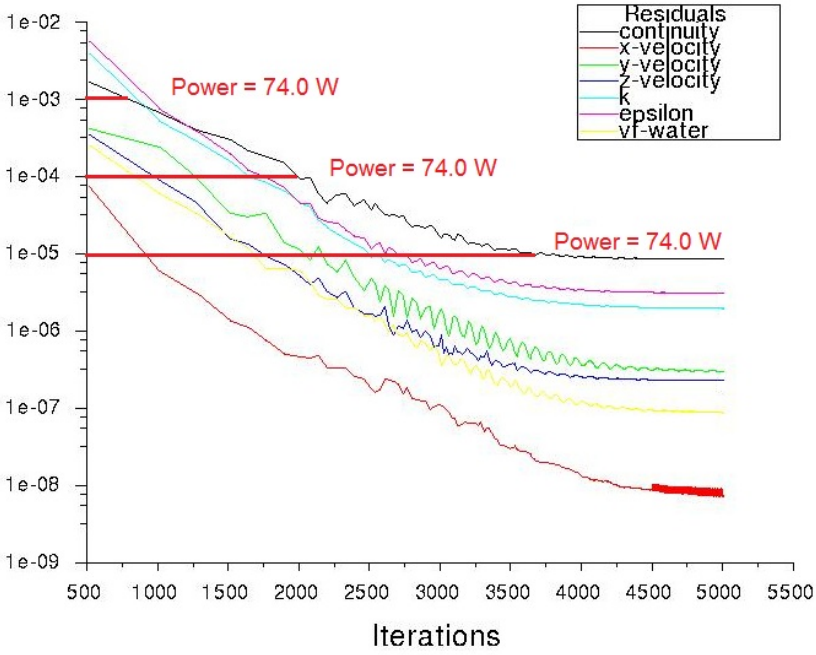

Figure 4.10: Convergence of power for a MHK turbine with a free surface

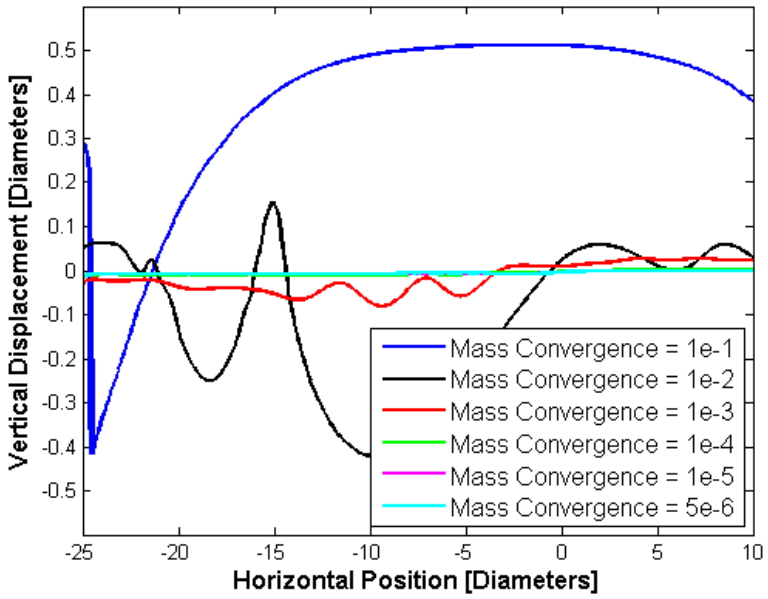

Figure 4.11: Convergence of the free surface for a MHK turbine

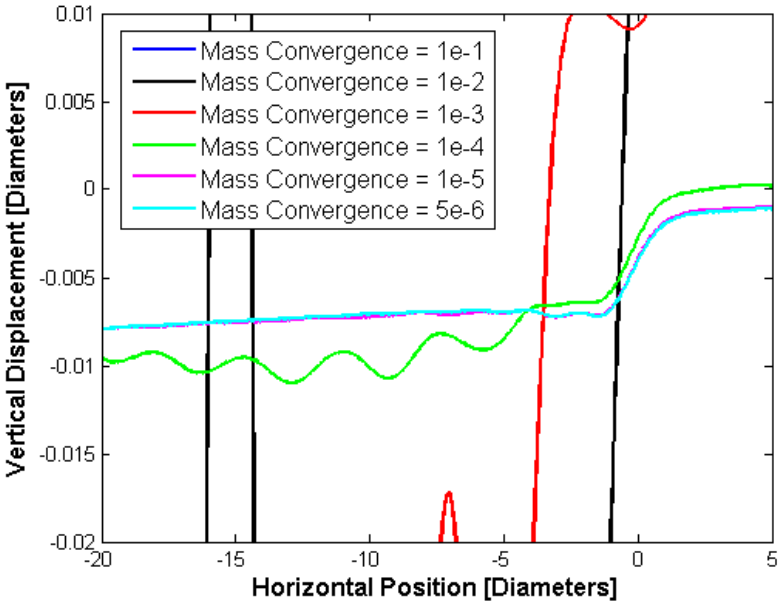

Figure 4.12: Zoomed in view of the convergence of the free surface for a MHK turbine

Chapter 5

RESULTS AND ANALYSIS

5.1 Interactions Between the Free Surface and a Horizontal Axis Turbine at Low Blockage Ratios

Five different simulations were performed in an open channel, 5 turbine diameter deep by 5 diameter wide by 35 diameter long. The depth of the turbine was measured from the center of the hub to the free surface varying over the five simulations to explore the hydrodynamics interactions between the MHK turbine flow and the free surface in a realistic range for confined configurations (flume testing or shallow water estuaries and rivers): 2.5D, 2D, 1.5D, 1D, and 0.75D. The simulations were performed with a 1m diameter (D) turbine and a free stream velocity of 1.25m/s in the negative y-direction. This produced a blockage ratio of 3.14%.

5.1.1 Free Surface Effects on the Wake of a Turbine

The dynamic pressure contours and the velocity profiles for three of the simulations can be seen in Figure 5.1. Dynamic pressure (q) is defined as:

$$q = \frac{1}{2}\rho v^2 \tag{5.1}$$

where ρ is the local density ($\phi \cdot \rho_{gas} + (1 - \phi) \cdot \rho_{lqiuid}$), and v is the local velocity. When using velocity contours it is challenging to distinguish between the two different fluids. Since the two fluids have very different densities and the densities are constant, the dynamic pressure can be used to both visualize the location of the free surface, distinguishing between the two phases, and to provide information about the velocity magnitude in the water flow.

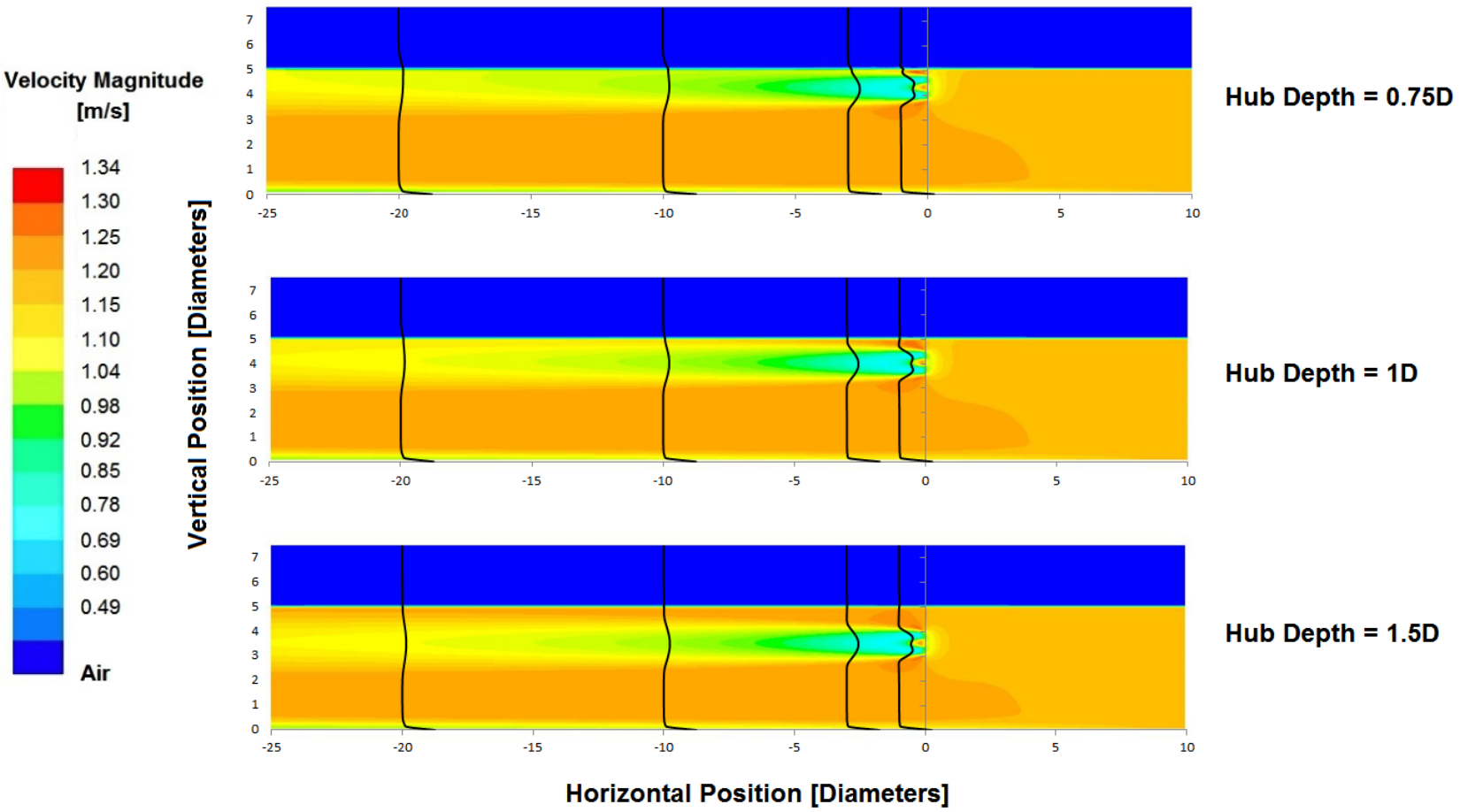

Figure 5.1: Contours of the dynamic pressure for different turbine depths. Velocity profiles at different locations downstream are also shown by the black solid lines. The scale shows the velocity magnitude for water that corresponds to the dynamic pressure contours. Flow is from right to left.

When the turbine hub depth is 1.5D (or higher) the wake appears symmetric, however, as the turbine is moved closer to the free surface the flow becomes asymmetric. The wake expansion at hub depths of 1D and 0.75D is vertically constrained by the free surface. This results in an asymmetric wake and an acceleration in the flow directly above the turbine.

Sun [18] suggests that when a turbine is in close proximity to the free surface the wake deficit recovery is accelerated, as shown in Figure 2.9. The centerline velocity was used, mistakenly, to show this trend. By examining Figure 5.2 we show that the minimum velocity for an asymmetric wake does not occur at the turbine's centerline as it does with an axi-symmetric wake. The wake centerline actually deflects towards the free surface. The minimum wake velocities 20D downstream of the turbine for the five different turbine depths can be seen in Table 5.1. At 20D downstream the minimum velocity decreases as the turbine depth decreases, showing that the wake deficit recovery is hindered, not accelerated, by the asymmetry induced by the free surface.

Table 5.1: Minimum Wake Velocities 20 Diameters Downstream of the Turbine and the Respective Decrease in Power Available in the Flow. The Power Available in the Flow was Based on the Minimum Velocity 20 Diameters Downstream, and the reference power used was based on the power available for a turbine at a hub depth of 2.5D

Turbine Depth	Minimum Velocity [m/s]	Percent Decrease in Available Power
0.075 D	1.0803	5.7
1 D	1.0999	0.5
1.5 D	1.1004	0.3
2 D	1.1016	0
2.5 D	1.1016	0

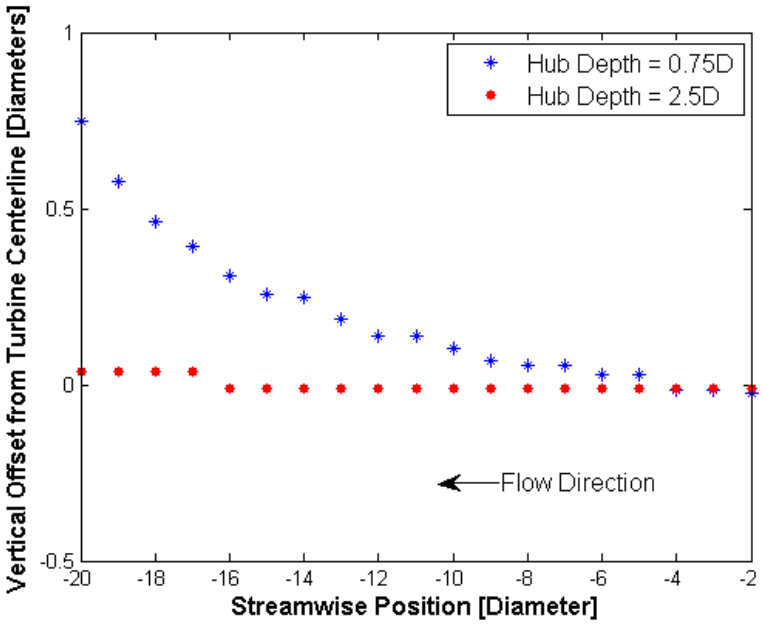

Figure 5.2: The vertical offset of the minimum wake velocity from the centerline of the turbine. For axi-symmetric flows the minimum wake velocity occurs at the centerline of the turbine as shown with the Hub Depth = 2.5D.

Figure 5.3 shows the wake deficit for two different hub depths, 0.75D and 2.5D. The results show the wake persists further downstream for a turbine closer to the free surface. In flows without a free surface the wake expands out uniformly. The higher momentum fluid surrounding the wake mixes with the lower momentum fluid in the wake resulting in an axi-symmetric recovery of the wake. The turbines 2D and 2.5D away from the free surface behave in this manner. When the turbine is closer to the free surface, the wake is constrained by the free surface directly above the turbine. As a result, the upper portion of the wake is not mixed with high momentum fluid at the same rate as the axi-symmetric wake and, thus, recovers slower than the bottom portion, with the velocity deficit persisting further downstream and

the wake becoming asymmetric. The change in power available in the flow based on the minimum wake velocity can be seen in Table 5.1.

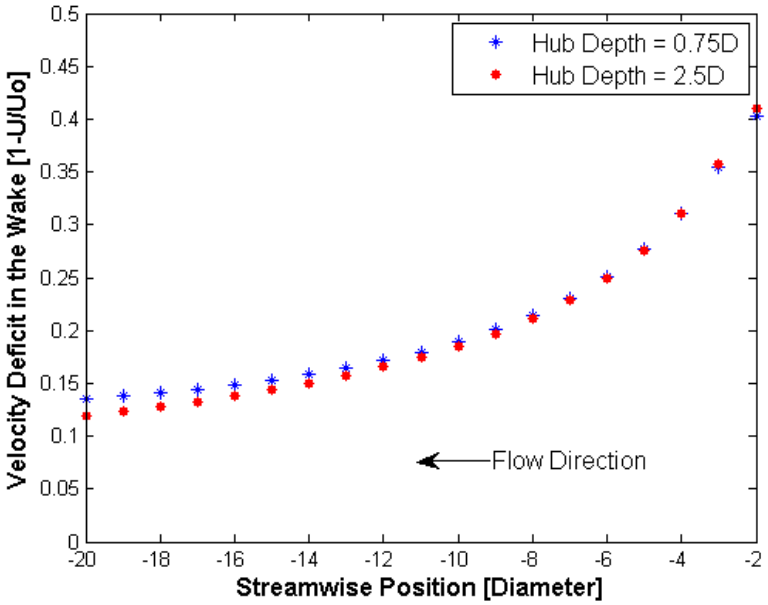

Figure 5.3: The decay of the velocity deficit downstream of the turbine

5.1.2 Free Surface Fluctuations

The fluctuations in the free surface height resulting from the turbine can be seen in Figures 5.4 and 5.5. The drop in the free surface height across the entire channel length remains constant regardless of the depth of the turbine. The total drop is the same because the power extracted by the turbine and the thrust force created by the turbine, solved for by the VBM, are approximately the same for each simulation, and the friction factor is the same for each simulation. The friction factor is constant because the channel dimensions and inlet velocity remain constant, as does the blockage ratio, as the turbine depth is varied. The conservation of momentum analysis performed in Section 3.4 shows that if the inlet conditions, friction factor, and thrust are the same,

the change in height across the channel will be the same.

The theoretical change in free surface height can be seen in Figure 5.4. This theoretical height drop was calculated using the conservation of momentum equation with the thrust force determined from the different simulations. The magnitude of the change in height modeled by the simulations and calculated by the theory is the same, suggesting the simulations behave in a physically sound manner. One reason the theory and simulations do not match up exactly is the boundary layer at the bottom of the channel. In the simulations, the boundary layer is not resolved so the velocity gradient at the bottom of the channel is not accurately modeled leading to a shear stress value that does not exactly match the friction factor expected for that Reynolds number flow and channel roughness.

The free surface deformation near the turbine changes for different turbine depths. Figure 5.4 shows that the amplitude of the fluctuations increase with the decrease in turbine depth. This is expected because the flow diverted vertically above the turbine will interact with the free surface. The turbine removes kinetic energy locally from the flow resulting in a slower fluid speed through the turbine. In order to conserve mass, some of the flow must be diverted around the turbine. When the turbine is close to the free surface, the free surface must raise directly upstream of the turbine to account for the fluid that has been diverted to the region above the turbine.

The turbine removes net potential energy globally from the flow causing a drop in the free surface directly above the turbine (at the horizontal position of zero). When the turbine is in close proximity to the free surface, stationary waves form downstream of the turbine and the waves decay in magnitude as the flow progresses downstream. It is important to relate the free surface fluctuations to a set of non-dimensional numbers that control the physics of the MHK turbine-free surface interactions.

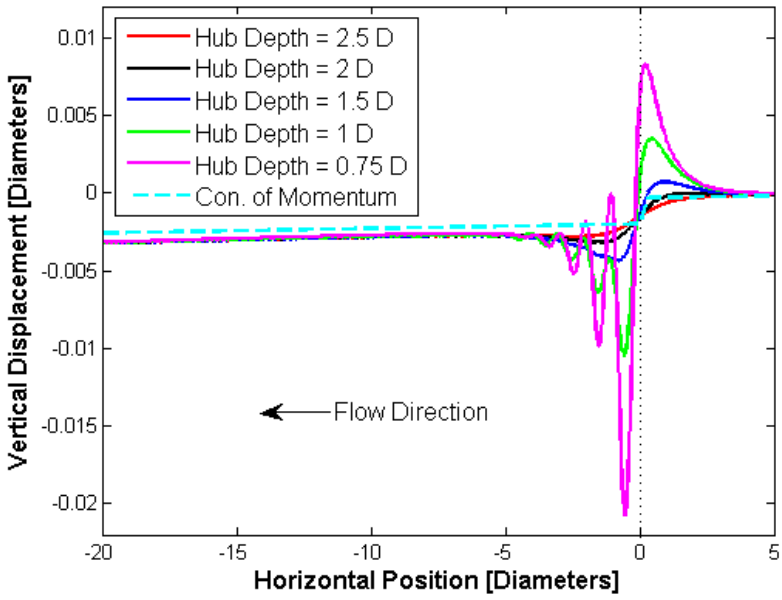

Figure 5.4: Vertical fluctuations in the free surface along the channel centerline. The turbine's horizontal position is represented by the dotted line.

5.2 Non-Dimensional Numbers used to Characterize the Effects of a MHK Turbine on the Free Surface

The non-dimensional number conventionally used to analyze free surface behavior is the Froude number, see Equation 1.2. The Froude number represents the balance between the free stream convective velocity and the speed of propagation of gravity waves at the interface between two fluids of different density, expressed in terms of the gravitational acceleration constant and a characteristic length scale of the flow (or more accurately of the wave amplitude). For typical open channel flow problems, the length scale is the channel depth [20]. However, since there is a turbine in the flow, several other length scales may be more appropriate, such as the turbine diameter, the distance from the free surface to the turbine's tip, or the distance from the free surface to the center of the hub, see Figure 5.6.

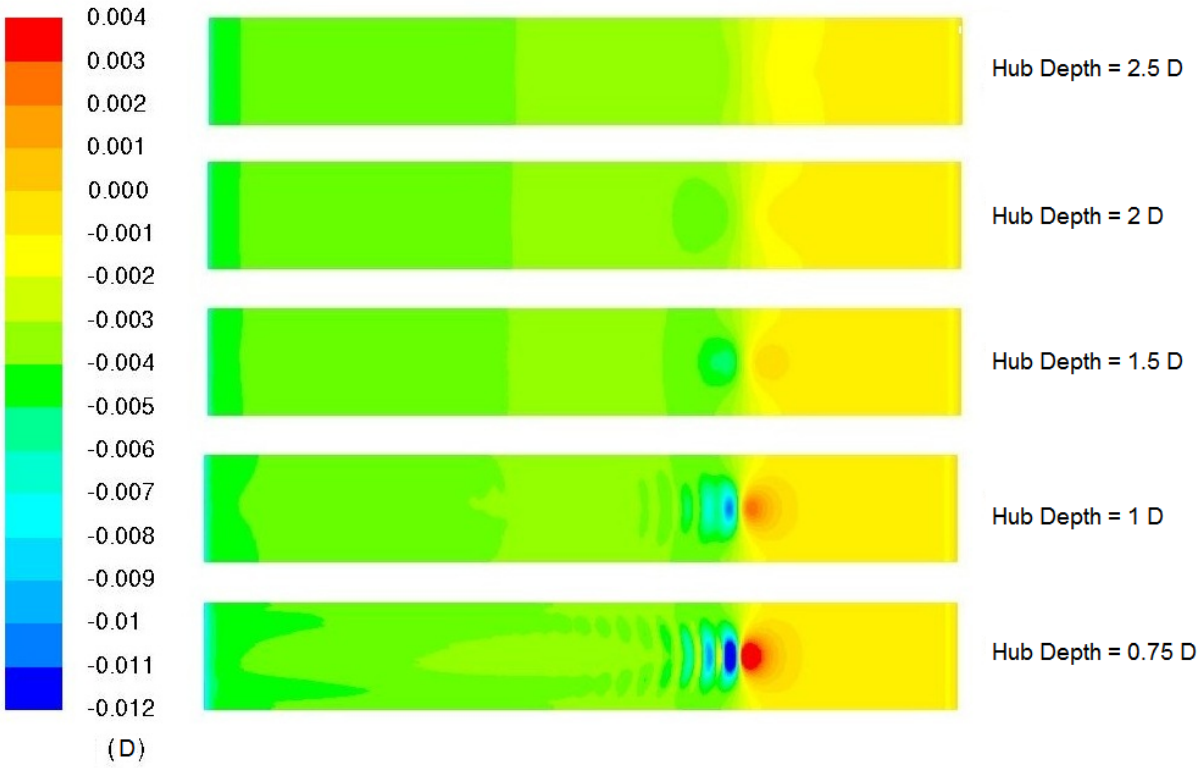

Figure 5.5: Contour representation of the vertical fluctuations in the free surface

Several sets of simulations were performed to determine the adequate characteristic length scale to use in formulating a Froude number in an open channel with a MHK Turbine. Table 5.2 shows the parameters that were varied for each simulation. The width of the channel was adjusted based on the channel height to maintain a constant blockage ratio of 0.0314 in every simulation. After all of the simulations were completed, each of the different length scales were applied to the Froude number and the free surface fluctuations were compared.

Figure 5.7 shows the free surface deformation resulting from turbines at different channel Froude numbers, that is where the length scale used is the channel depth. Since the Froude numbers are different, if the channel depth was the proper length

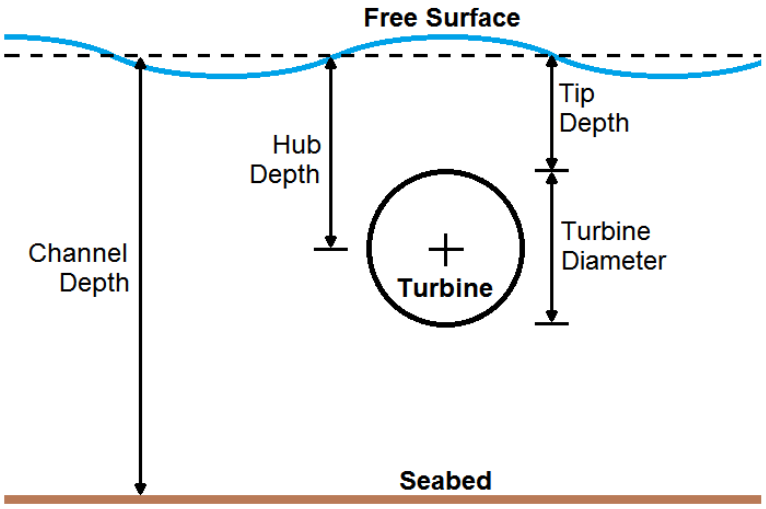

Figure 5.6: Possible characteristic length scales for a MHK turbine in a channel

Table 5.2: Simulation Parameters for Determining the Characteristic Length Scale of the Froude Number

Parameter	Values
Turbine Diameter [D]	1m, 0.5m
Hub depth	2.5 D, 2 D, 1.5 D, 1 D
Channel Depth	5 D, 4 D, 3 D

scale, the free surface fluctuations should be different. However, the fluctuations are the same. This demonstrates that the free surface fluctuations, at least for low blockage ratios, are independent of the channel depth. It should be noted that the Froude number based on channel depth is much less than one for locations were MHK turbines will be placed, so the channel depth is not expected to affect the flow. For example, taking the extremes for channel depth (low) and current speed (high) of 5m deep channel and 2.5m/s current speed, the Froude number is only 0.36, much below

the transition to supercritical. The values for channel depth and current speed were found in reference [49].

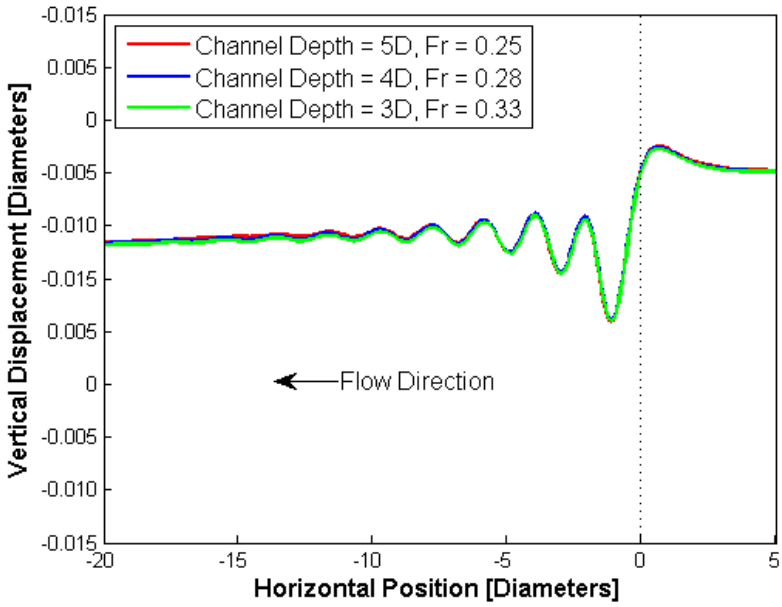

Figure 5.7: Free surface fluctuations for different Froude numbers based on channel depth, where the velocity is 1.25 m/s, the hub depth is 0.75m and the turbine diameter (D) is 0.5m

Figure 5.8 shows the free surface fluctuations for two different simulations with the same Froude number when the characteristic length is the tip depth. The fluctuations are shown in physical values and in non-dimensional form. If the Froude number based on the tip depth was the non-dimensional parameter governing the free surface deformations due to the interaction with the MHK turbine, the values presented for the free surface fluctuations in those two simulations with the same $Fr_{tip\ depth}$ would be the same, but they are not. Therefore, the tip depth is not a good candidate for the characteristic length scale in this problem.

Figure 5.9 shows the free surface fluctuations for two different simulations with the

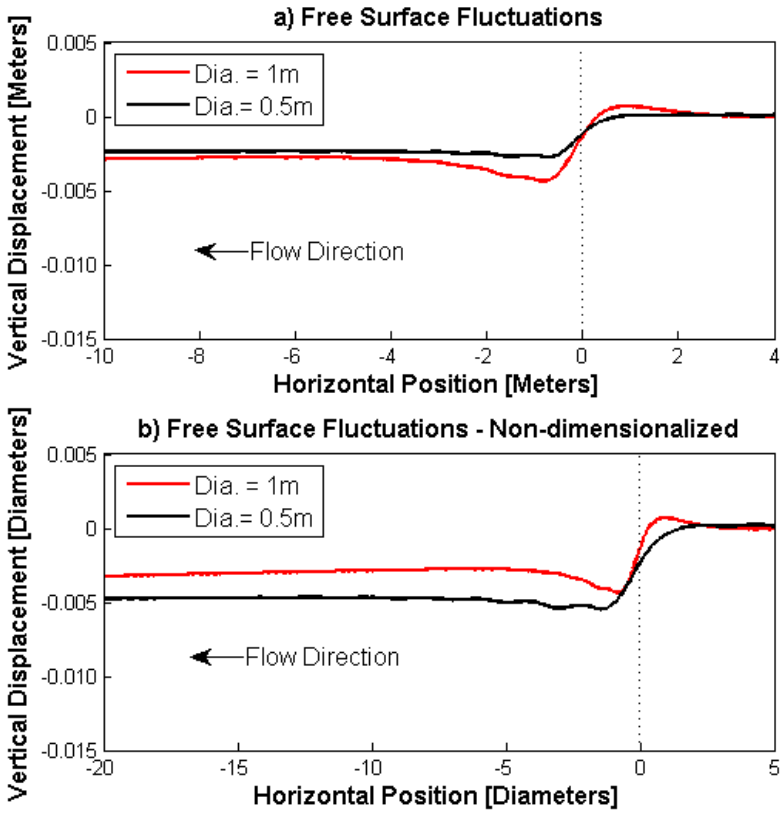

Figure 5.8: Free surface fluctuations for the same Froude number based on tip depth, where the velocity is 1.25 m/s and the tip depth is 1m

same Froude number using the hub depth as characteristic length. Both the physical values of the fluctuations and the non dimensional values compared to the turbine diameter are shown. If the characteristic length scale was the hub depth, the free surface fluctuations would be the same, but they are not. Therefore, the hub depth does not represent a viable characteristic length scale to form a Froude number in this problem.

None of the previously analyzed length scales; channel depth, tip depth, or hub depth, when applied to the Froude number, produced the free surface similarity that would

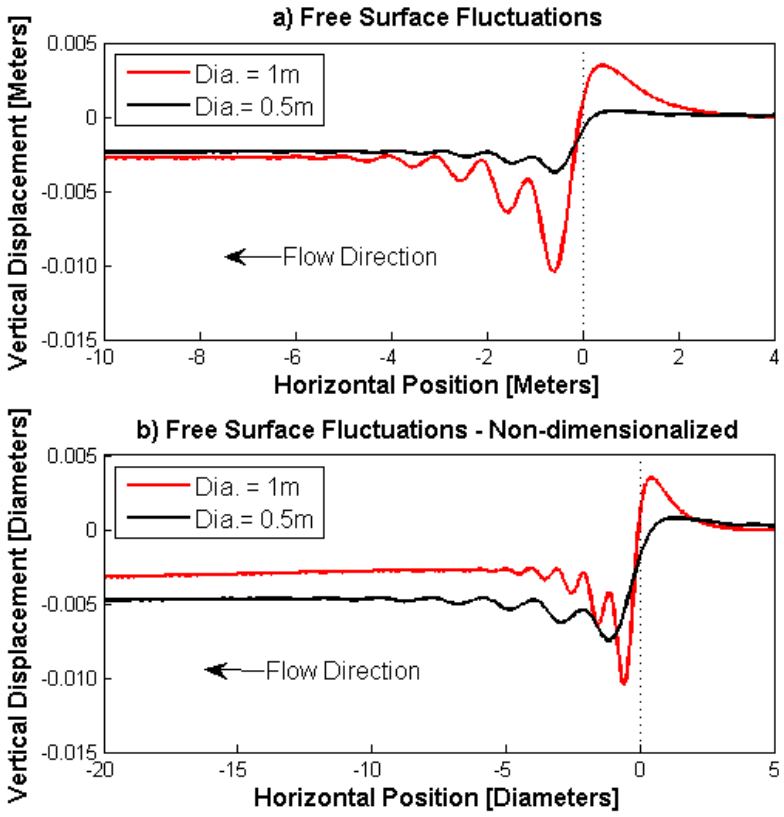

Figure 5.9: Free surface fluctuations for the same Froude number based on hub depth, where the velocity is 1.25 m/s and the hub depth is 1m

be expected if the Froude number was the only non-dimensional parameter describing the physics of MHK turbine-free surface interactions. One of the potential problems with trying to apply a depth as the characteristic length scale is that it does not account for the size of the turbine. For example, consider a small rock and a large rock in a river of constant depth, see Figure 5.10. In the figure, the change in the free surface resulting from a large rock in the center of the river is very noticeable, however, the fluctuations resulting from all the small rocks around the large rock are not. Now consider a small fish and a large fish the same distance below the free

surface. The large fish would be expected to produce a larger free surface deformation than the small fish. Therefore, using a characteristic length scale related to the size of the turbine might produce better results.

Figure 5.10: Free surface fluctuations resulting from a large rock [50]

For a submerged object, the characteristic length scale applied to the Froude number is the size of the object [51]. This would suggest that the diameter of the turbine should be used as the characteristic length scale. Figure 5.4 shows the free surface fluctuations for simulations with the same Froude number based on turbine diameter. It can be seen that the free surface fluctuations depend on turbine depth. According to Zhu [51], the free surface fluctuations due to a submerged object, do not just depend on the Froude number, they also depend on a non-dimensionalized depth of the object. Thus, if the diameter is the characteristic length scale for the Froude number another non-dimensional number is also needed to describe depth's effect on the fluctuations.

Figure 5.11 shows the free surface fluctuations for six different simulations. The simulations used the same Froude number that was based on turbine diameter, and the same non-dimensional depth (d_r), where d_r is the ratio between the hub depth and the turbine diameter. The simulations with a 0.5m diameter turbine were performed with an inlet velocity of 1.25m/s. In order to produce the same Froude number the

simulations with a 1m diameter turbine were performed with an inlet velocity of 1.77m/s. The angular velocity of the larger turbine was also adjusted to maintain the same Tip Speed Ratio. In Figure 5.11, it can be seen that the free surface fluctuations, including the amplitude and period of the stationary waves, of the six different simulations are the same, regardless of the channel depth. Therefore, we conclude that there are two non-dimensional parameters necessary to characterize fully the interactions of a MHK turbine with a free surface: the Froude number based on turbine diameter and the depth-to-diameter ratio.

$$Fr_D = \frac{U}{\sqrt{gD}} \tag{5.2}$$

$$d_r = \frac{Hub\ \ Depth}{Diameter}. \tag{5.3}$$

It is important to understand how each of these non-dimensional numbers affects the free surface. Decreasing d_r leads to an increase in the depth of the stationary waves downstream of the turbine with the first waves occurring closer to the turbine, see Figure 5.12. The distance between the trough of the first wave and the trough of the second wave, the wave length (λ), decreases with a decrease in d_r, see Figure 5.13 and Table 5.3.

As the Froude number decreases (decrease the free stream velocity or increase the turbine diameter), the wave depth decreases, and the first wave occurs closer to the turbine, see Figure 5.12. Furthermore, the wavelength between the first wave's trough and the second wave's trough decreases, see Figure 5.13 and Table 5.3.

It should be noted that the stationary waves that form as a result of the turbine are deep water waves because the channel height is greater than 0.28 times the wavelength [52]. The wavelength for each simulation can be seen in Table 5.3.

The value for d_r does not affect the total drop in elevation across the turbine. Figure 5.4 shows that at different hub depths the stationary waves change with the non-

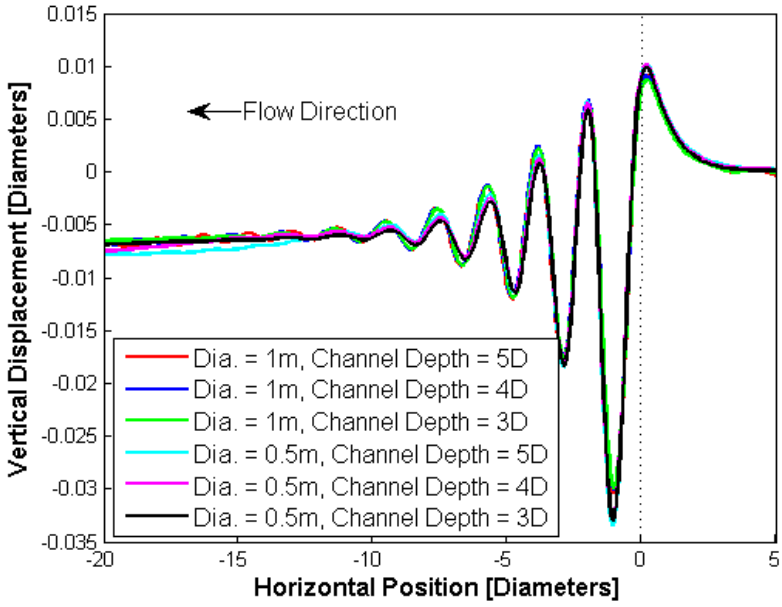

Figure 5.11: Free surface fluctuations for six cases with the same Froude number, based on the turbine diameter ($Fr = 0.565$) and the same non-dimensionalized depth ($d_r = 1$)

dimensionalized depth but the drop in free surface height across the turbine does not. The Froude number based on turbine diameter, however, does affect the drop in elevation across the turbine, see Figure 5.14. An increase in the Fr_D increases the drop in elevation across the turbine.

This section has shown that the free surface fluctuations are independent of the channel depth. One possible exception for this conclusion is MHK turbines operating at high blockage ratios. According to the theory of Whelan [3] and Polagye [8] C_p increases with the blockage ratio and the Froude number based on channel depth (channel Froude number). Section 5.3 shows C_p is not affect by the channel depth, and hence the channel Froude number at low blockage ratios. According to the one-dimensional flow theory, at very high blockage ratios, greater than 30%, the channel

Table 5.3: Free Surface Fluctuations, see Figure 5.13

Fr_D	d_r	Z_{min}	Y_{min}	λ
0.4	1.5	0.004	0.751	-
	1	0.011	0.569	0.973
	0.75	0.021	0.533	0.970
0.565	2	0.008	1.085	-
	1.5	0.013	0.9731	1.936
	1	0.030	0.936	1.890
	0.75	0.052	0.862	1.675

Froude number begins to have a significant effect on C_p, see Figure 2.2. However, very few MHK turbines, specially horizontal axis, will ever be operated at that high of a blockage ratio because the flow will be significantly altered by the turbine causing a multitude of environmental effects. The only real purpose for turbines operating at such high blockage ratios is to hydraulically control a channel. Therefore, for turbines operated in usual conditions, the Froude number based on channel depth has a negligible effect on the flow. This is discussed in detail in Section 5.5.

5.2.1 Slope Correction

The free surface elevation drop that balances the frictional force on the bottom of the channel is a function of the flow speed and the channel width, see Equation 3.46. In these simulations the blockage ratio was kept constant, so the width of the channel had to change when the channel depth was changed. Equations 3.48 and 3.47 show that an increase in channel width decreases the hydraulic diameter, which decreases the Reynolds number, and in turn increases the friction factor. This leads to a higher momentum loss due to friction that is balanced by a larger difference in free surface

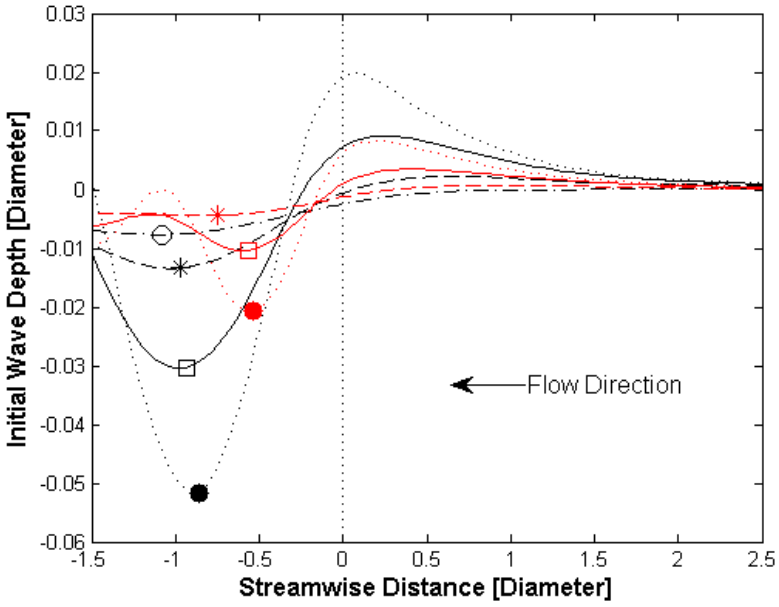

Figure 5.12: The depth and position of the stationary wave directly downstream of the turbine. Red is for a $Fr_D = 0.4$ and black is for a $Fr_D = 0.565$. The different lines represent the free surface fluctuations and the symbols represent the maximum wave depth. $--$ and $\circ$ represent a $d_r = 2$. $\cdot - \cdot$ and $*$ represent a $d_r = 1.5$. $-$ and $\square$ represent a $d_r = 1$. $\cdots$ and $\bullet$ represent a $d_r = 0.75$.

height across the channel. Table 5.4 shows the theoretical friction factors calculated for each channel and the friction factors produced by the numerical simulations for each channel. The trends and approximate magnitude of the friction factors produced in the simulations match those predicted by theory. The difference in the friction factors is the result of the simulations not accurately modeling the boundary layer near the bottom of the channel.

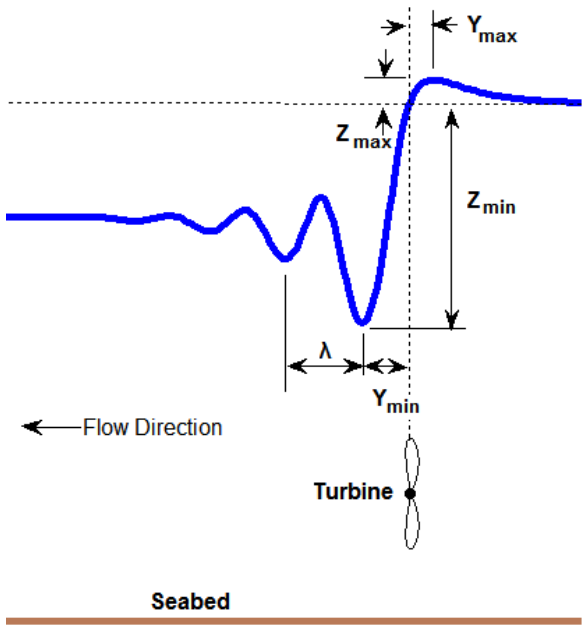

Figure 5.13: Explanation of the variables used in Tables 5.3 and 5.6. Z_{min} is the depth of the first wave, λ is the wave length between the first wave's trough and the second wave's trough, and Y_{min} is horizontal distance between the turbine and the first wave's trough. Z_{max} is the height of the deformation of the free surface directly upstream of the turbine and Y_{max} is the horizontal distance from the turbine to the peak of the deformation upstream of the turbine.

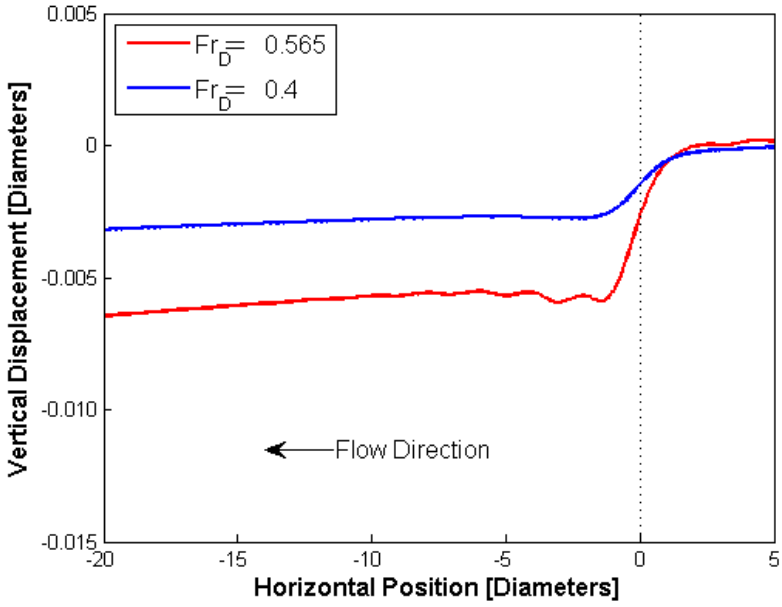

Figure 5.14: Free surface fluctuations for simulations with the same d_r but different Froude numbers

Table 5.4: Friction Factors for the different simulations

Turbine Diameter	Velocity	Channel Depth	Channel Width	Theoretical Friction Factor	Simulated Friction Factor
1m	1.77 m/s	5m	5m	0.0069	0.010
		4m	6.25m	0.0071	0.010
		3m	8.33m	0.0073	0.0106
1m	1.25 m/s	5m	5m	0.0072	0.0102
		4m	6.25m	0.0074	-
		3m	8.33m	0.0077	-
0.5m	1.25 m/s	2.5m	2.5m	0.0079	0.0125
		2m	3.125m	0.0081	0.0128
		1.5m	4.17m	0.0085	0.0138

The different free surface slopes related to the different friction factors made comparing the free surface fluctuations challenging. A slope correction was created to adjust the free surface slope to match the slope in the simulations performed with a 1m diameter turbine in a channel 5D deep. Figures 5.7, 5.8, 5.9, and 5.11 have had this slope correction applied. It is important to understand the slope correction is not scaling the free surface drop resulting from the turbine, it is only accounting for the free surface drop related to the bottom friction. Figure 5.15 shows a free surface before and after the slope correction was applied. The elevation drop resulting from the power extracted by the turbine does not change when the slope correction is applied nor does the magnitude and period of the stationary waves.

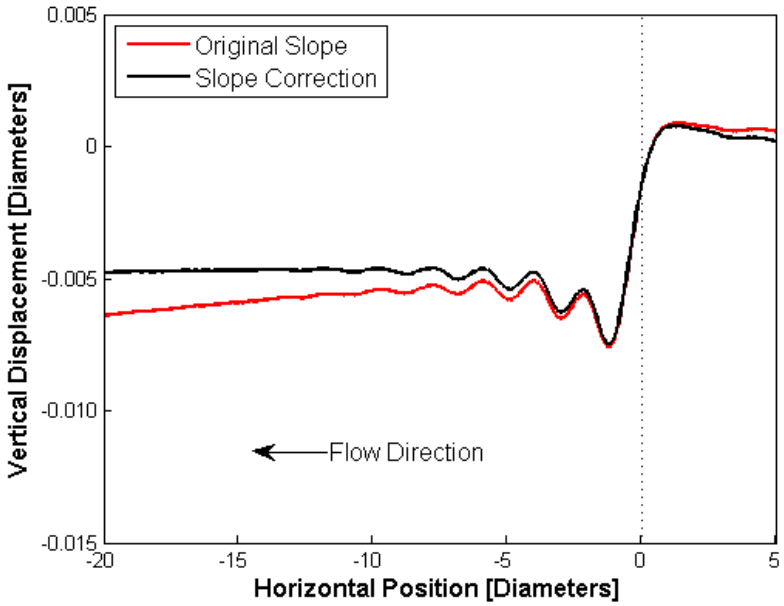

Figure 5.15: Free surface fluctuations with and without the slope correction

5.3 The Effects of the Free Surface on the Coefficient of Power at Low Blockage Ratios

The power extracted by the turbine in each simulation was noted and non-dimensionalized using the free stream velocity, to produce the turbine's coefficient of power, see Equation 2.1. The C_p values for simulations performed with a 0.5m diameter turbine can be seen in Figure 5.16. The C_p values for simulations performed with a 1m diameter turbine are shown in Figure 5.17.

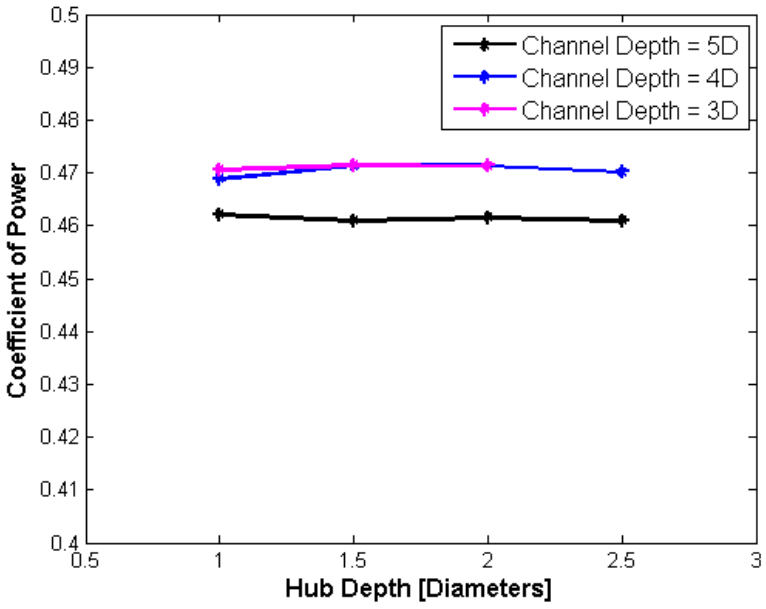

Figure 5.16: The coefficient of power for simulations performed with a 0.5m diameter turbine. The simulations were performed with different channel depths and hub depths.

The coefficients of power for the 0.5m diameter turbine are within ± 0.01 for every channel depth and turbine depth. This is also true for the 1m diameter turbine. There are no apparent trends between C_p and the channel depth or the hub depth. Thus, at this blockage ratio, C_p is either negligibly affected or not affected at all by channel

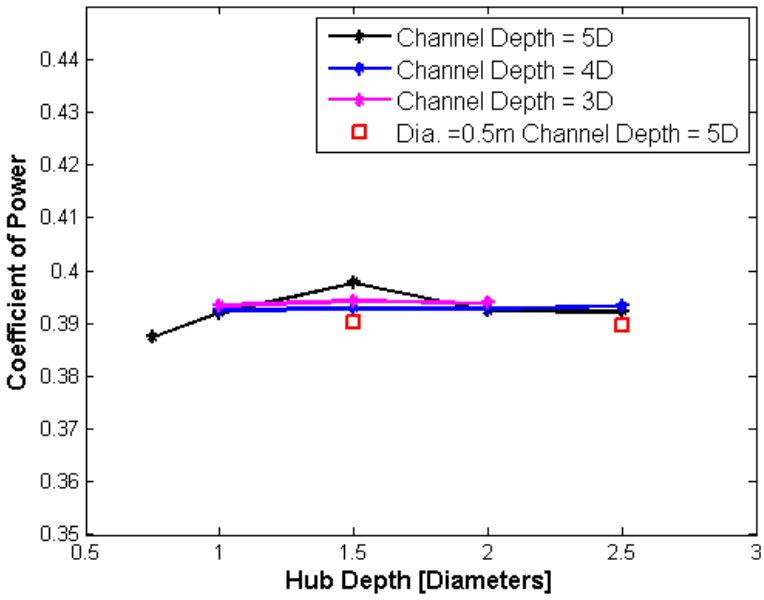

Figure 5.17: The coefficient of power for simulations performed with a 1m diameter turbine. The simulations were performed with different channel depths and hub depths. □ represents the coefficients of power for a 0.5m diameter turbine with the same number of mesh cells in the wake as the 1m diameter turbine.

depth or turbine depth. The average coefficient of power for the smaller turbine is 0.467 whereas the average C_p for the larger turbine is 0.393. Since these flows have all of the same non-dimensional numbers they should also have the same C_p.

Upon further examination the difference in C_p was determined to be a result of the mesh refinement in the turbine wake. Originally, the same mesh size was used in every simulation. This was to ensure the free surface behavior would be captured identically for all simulations. When the mesh for the smaller, 0.5m diameter turbine, was refined to have the same number of mesh elements as the larger turbine, the C_p values for the two different size turbines matched, however, the free surface fluctuations became slightly different.

For every simulation, it was determined that it was necessary to keep the number of mesh elements in the wake constant, while maintaining the size of the elements near the free surface. This was applied by setting the number of mesh elements on the outside of the rotor to 90 and fixing the mesh size near the free surface to 0.05m. This produced the same coefficients of power for the two different size turbines and the same free surface fluctuations for a certain Froude number and Depth-to-Diameter Ratio, Figure 5.18 and Figure 5.16.

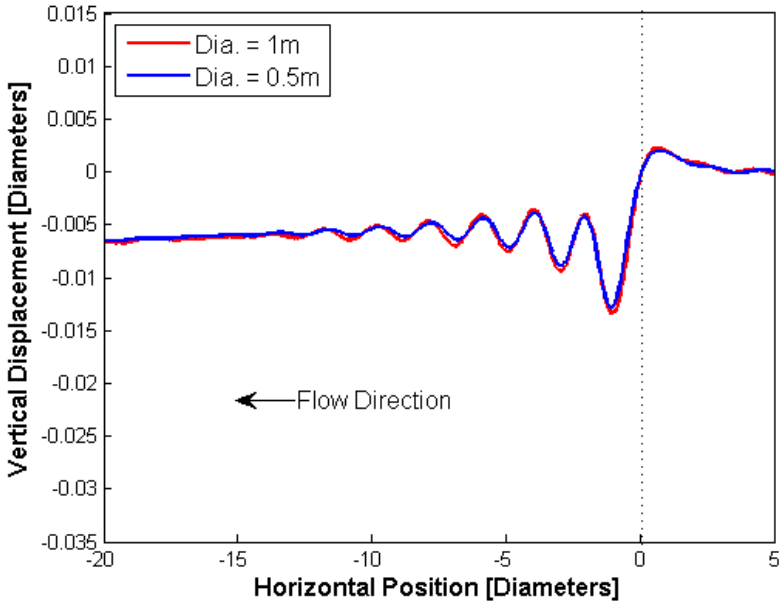

Figure 5.18: Free surface fluctuations for the same Froude number, $Fr = 0.565$, and same depth to diameter ratio, $d_r = 1.5$, where the number of mesh cells in the wake is constant and the size of the mesh cells at the free surface is constant.

5.4 Blockage Ratio Effects on MHK Turbine Performance

The previous sections are dedicated to the study of flows at a low blockage ratio, similar to what may be seen in the field. However, it is important to understand how

the blockage ratio may affect the power produced to ensure flume experiments, which have higher blockage ratios, are not misrepresenting the amount of power a MHK turbine can generate. This study is also relevant to turbines in rivers, channels, and estuaries, where high blockage ratios (and relatively high channel Froude numbers, Froude number based on channel depth) can be reached.

A preliminary set of simulations were performed at blockage ratios of 3.14%, 5.23%, and 12.5%. The simulations applied the same methodology seen in Section 4, but with differing channel sizes. Figure 5.19 shows the resulting free surface fluctuations for each case and Figure 5.20 shows the power extracted by the turbine in each case. These simulations were performed with an inlet velocity of 1.25 m/s.

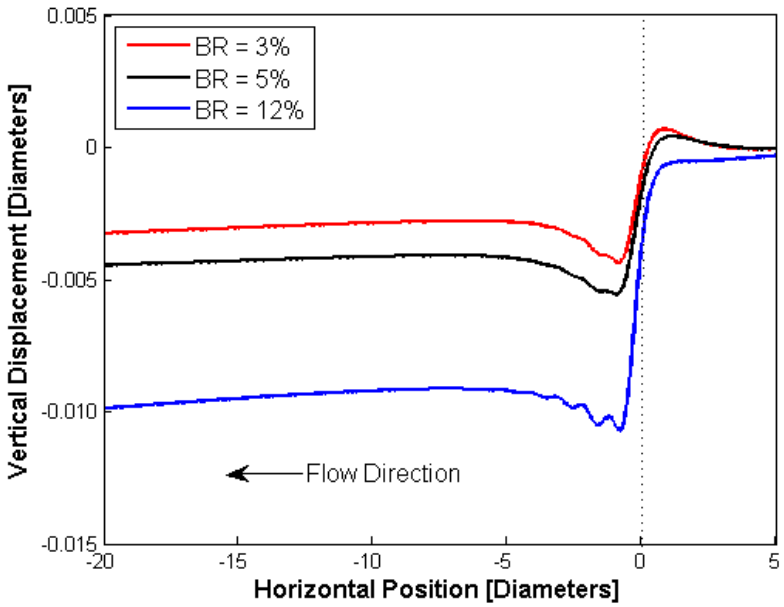

Figure 5.19: Free surface fluctuations for simulations with different blockage ratios.

Figure 5.19 shows increasing the blockage ratio results in an increase in the free surface drop across the turbine. According to the control volume analysis, the increased change in free surface height should mean that more power is extracted by the turbine,

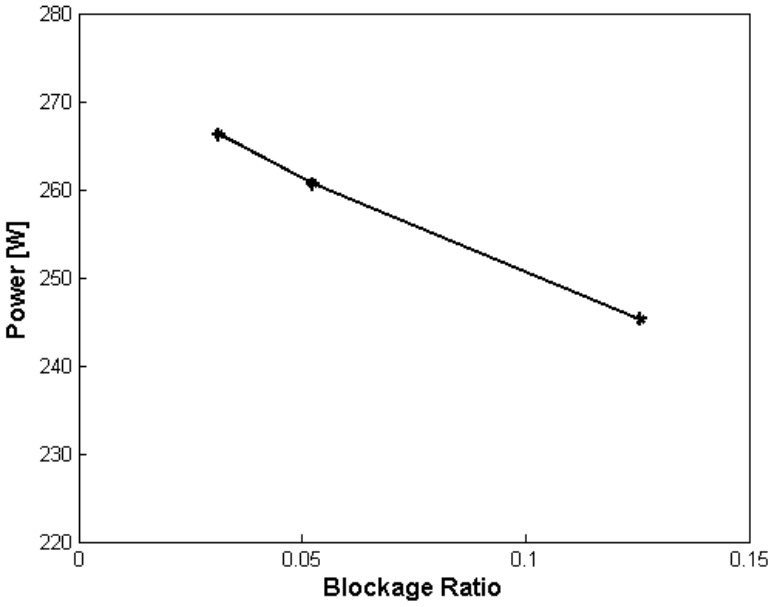

Figure 5.20: Power extracted by the turbine versus blockage ratio.

however, Figure 5.20 does not show that. After further examination of the entire simulation, two major problems were identify as the reasons for this discrepancy, a change in inlet velocity, and a change in the Tip Speed Ratio (TSR) that produces the maximum coefficient of power.

5.4.1 Changing Inlet Velocities

First, to address the change in inlet velocity it is important to point out that the inlet boundary condition used in the simulations was specially tailored by Fluent for open channel flow problems. The inlet boundary condition dialog box asks for the inlet velocity magnitude, and according to the Fluent User Manual [43], the user should enter the magnitude of the upstream inlet velocity. Thus, the inlet velocity of 1.25m/s was entered and assumed to be fixed. After studying the velocity contours at the inlet for each simulation it became apparent that the inlet velocity had changed

as the simulations converged. The amount the velocity changed was related to the blockage ratio. As the blockage ratio increased the amount of inlet velocity variations increased. The exact reason for this change is still unknown, however, it maybe a result of assigning a total pressure at the inlet. If the total pressure is fixed at the inlet and the static pressure increases due to a change in free surface height, the dynamic pressure must decrease to compensate, decreasing the velocity. The other inlet boundary condition found to perform well in Section 3.5.3 was the mass flow rate boundary condition. However, the same problem occurs with that boundary condition. When the free surface height rises at the inlet, the cross sectional area of the flow increases so the velocity must decrease to maintain the inlet mass flow rate of water.

The power extracted is related to the velocity cubed, so it was concluded that the change in inlet velocity was partially responsible for the inaccurate relationship between power and blockage ratio seen in Figure 5.20. To correct for this problem the coefficient of power was used, see Figure 5.21. C_p is the power non-dimensionalized by the velocity, so C_p is independent of the inlet velocity. Figure 5.21 shows that the C_p increased with the blockage ratio as expected.

5.4.2 TSR Versus Coefficient of Power

To address the problem of the change in TSR that produces the maximum power, note that C_p is related to the TSR in such a way that at low TSRs C_p increases as the TSR increase, but at some point the C_p reaches its maximum value and begins to decrease with any increase in TSR. To produce maximum power turbines are operated at the TSR that corresponds to the maximum C_p. The angular velocity of the turbine and the free stream velocity used in the simulations are set to produce the TSR that corresponds to the maximum C_p. The free stream velocity is used for calculating the TSR instead of the turbine's local velocity because the free stream velocity is known prior to starting the simulations. As the blockage ratio increases there is less area

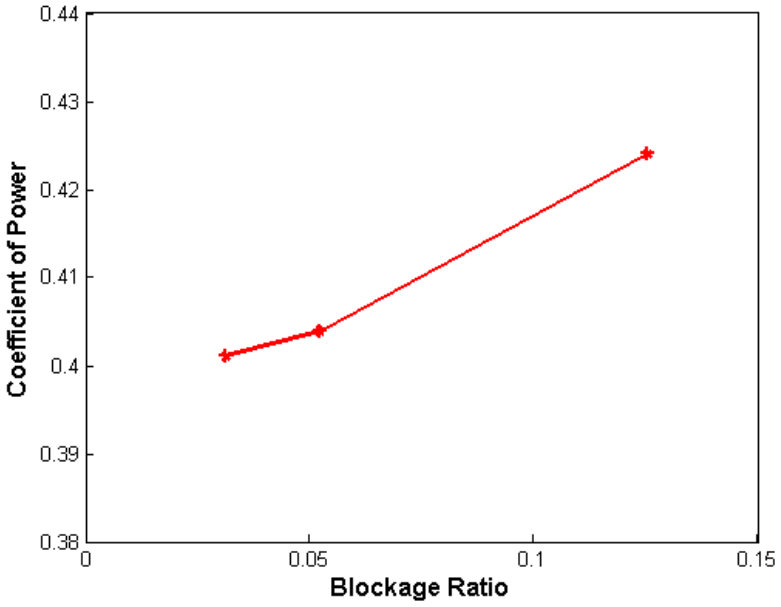

Figure 5.21: Coefficient of power versus blockage ratio

around the turbine for flow to be diverted leading to a higher velocity at the turbine, and a lower local TSR at the turbine. The coefficient of power depends on the local TSR. By changing the local TSR, the turbine is no longer operating at the peak C_p , see Figure 5.22.

To correct for this problem, new TSR versus C_P curves were created. The TSR was still based on the free stream velocity because the local velocity is unknown at the beginning of the simulation. These curves were created for blockage ratios of 4%, 9%, 20%, and 44%. The simulations were performed without a free surface to minimize computational time. Consul [37] showed using a rigid lid instead of a free surface had very minor effects on the simulation's results, therefore this is an acceptable simplification. The results can be seen in Figure 5.23. There are two primary trends that can be seen in Figure 5.23. First, in the region of TSR that produce the peak efficiencies, between 6 and 7, the C_p is higher for higher blockage ratios. Second, the

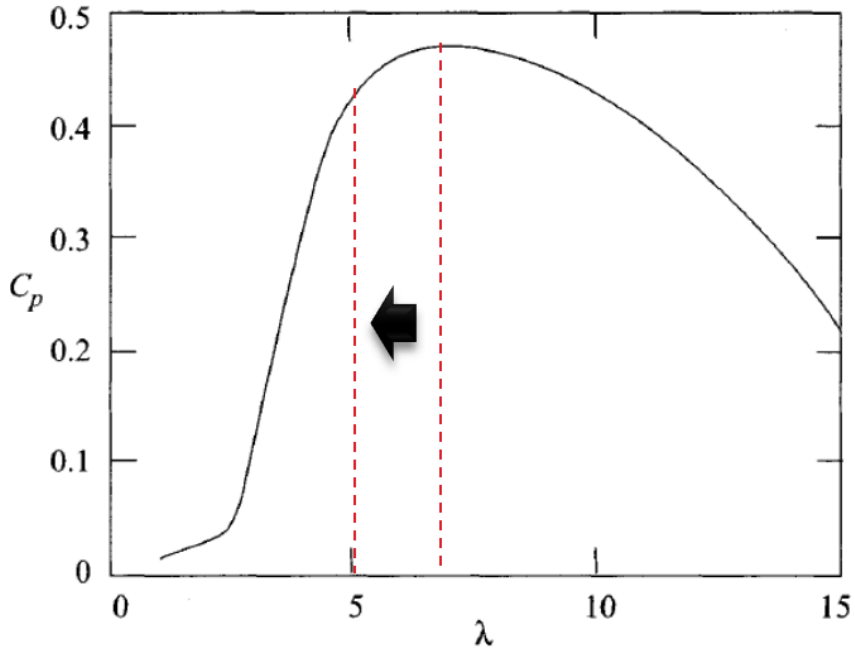

Figure 5.22: As the velocity through the turbine increases, the local tip speed ratio (λ) decreases moving down the λ versus C_p curve to a lower C_p [25]

TSR that produces the maximum C_p increases as the blockage ratio increases. This is to counteract the increase in local velocity at the turbine caused by the higher blockage ratios.

It is important to adjust the TSR for different blockage ratios to ensure the turbine is always operating at the maximum C_p. To demonstrate this point, Figure 5.24 shows the C_p for different blockage ratios when the TSR is 6.4, which is the TSR that produces the maximum C_p for a blockage ratio of 9%. It also shows the maximum C_p for the different blockage ratios. At the higher blockage ratios of 20% and 44% there is an appreciable increase between the C_p produced with a TSR of 6.4 and the maximum C_p that will not be realized unless the angular velocity of the turbine is adjusted to operate at a higher TSR.

Whelan [3] performed a set of experiments using the same rotor in a flume, which had

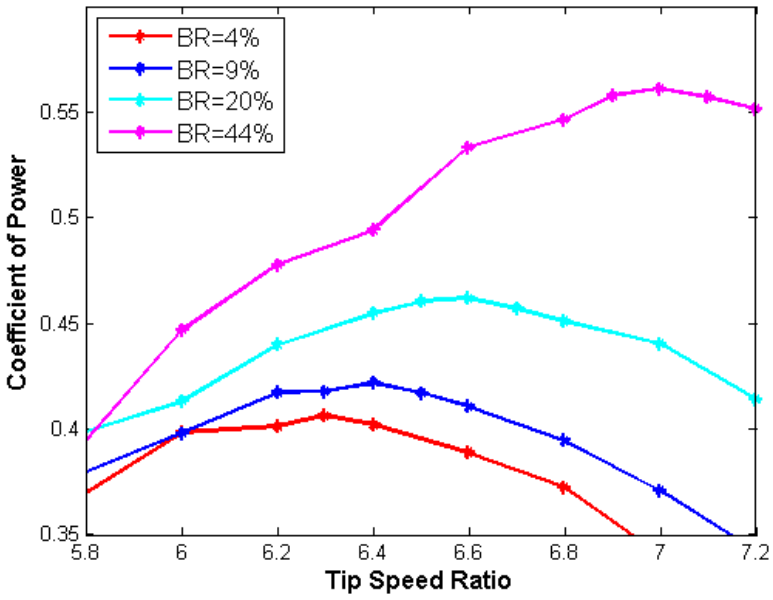

Figure 5.23: TSR versus C_p curves for different blockage ratios.

a blockage ratio of 64%, and in a wind tunnel, which had a blockage ratio of 5%. The rotor used for the experiments does not have the same airfoil as the turbine modeled in this thesis, therefore the simulation results cannot be validated using the experimental results. However, it is still useful to compare the TSR versus C_p curves obtained in the numerical simulations to experimental data to ensure the results produced are reasonable. Figure 5.25 shows Whelan's experimental results along with the results from this thesis.

The TSR that produces the maximum C_p was lower for the rotor used experimentally. This was expected because different rotors operate at different TSRs. The maximum C_p value found experimentally for a blockage ratio of 5% is approximately equal to the C_p found in the simulations for a blockage ratio of 4%. Also, in both the experiments and the numerical simulations, the TSR corresponding to the maximum C_p increased with an increase in blockage ratio. The C_p found in the numerical simulations appear

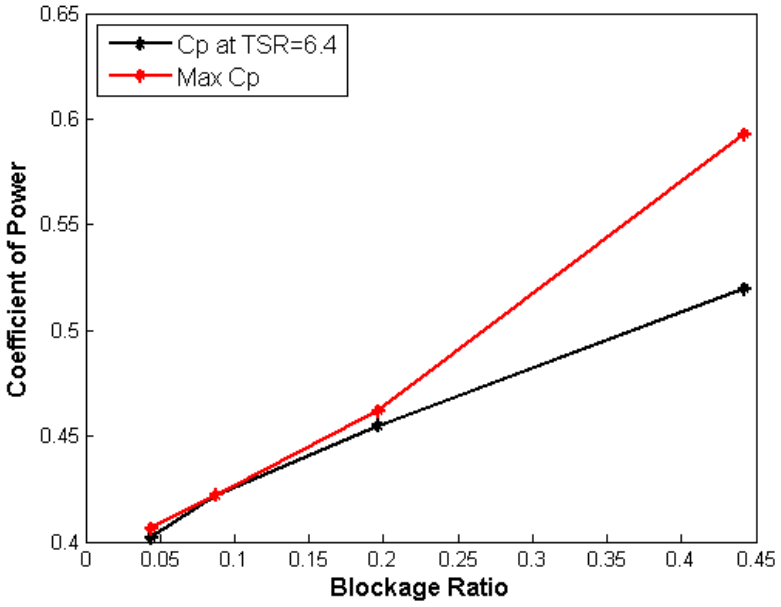

Figure 5.24: C_p values for a specific TSR compared with the maximum C_p at different blockage ratios

to lie in the appropriate range of C_p values found experimentally. Even though this does not validate the results of this thesis, it demonstrates the results are at least realistic and provides some confidence to the simulations.

5.5 Numerical Simulations of Experiments Performed with Scaled Turbines

At this time, there are several sets of MHK turbine experiments under way at the University of Washington. It is desirable to use the experimental data to validate the simulations presented in this thesis.

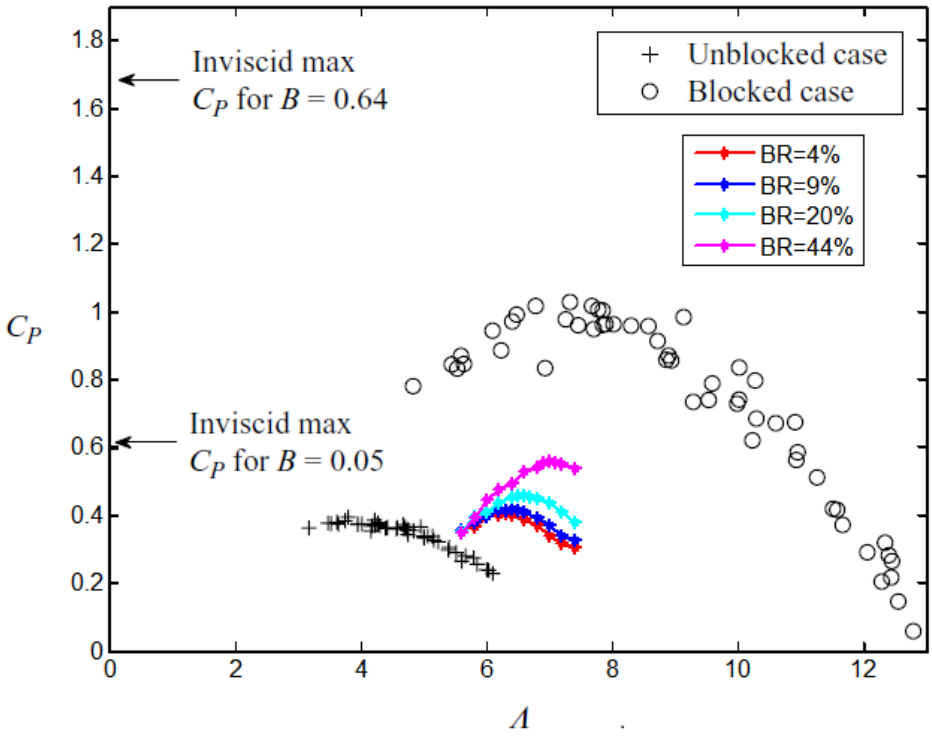

Figure 5.25: TSR versus C_p curves for different blockage ratios found numerically, compared to experimental data from Whelan[3]. The blocked case refers to experiments performed at a blockage ratio of 64%, and the unblocked case refers to experiments performed at a blockage ratio of 5%

5.5.1 Experiments at Low Reynolds Numbers

When performing experiments using scaled MHK turbines, it is challenging to maintain all of the important non-dimensional numbers from full scale turbines. Often the Reynolds number must be lowered to maintain other non-dimensional numbers [29]. It is generally considered acceptable to use a lower Reynolds number as long as it is still in the same asymptotic turbulent regime as the full scale turbine, because in turbulent flows the coefficients of lift and drag are considered independent

for large enough Reynolds number. However, if the chord length based Reynolds number approaches the transition between laminar flow and turbulence, C_L and C_D start to depend heavily on the Reynolds number [53]. This transition occurs around a Reynolds number of 7×10^4. The dependence of C_L and C_D on Reynolds number is suspected to be the result of the formation of Laminar Separation Bubbles (LSB) on the upper surface of the airfoil [54].

Several scaled experiments were performed in September 2012 using a flume at the Bamfield Marine Sciences Centre in British Columbia. The C_p values produced experimentally were much lower than the results predicted by Lawson [44] and Tessier [45]. One possible reason for the discrepancy in C_p values is the chord length based Reynolds number was about 7×10^4, so LSBs may have formed on the blade. The presence of a LSB on the blade reduces the C_L and subsequently the power produced. Figure 5.26 shows a numerical simulation of the turbine blade's airfoil performed using a Reynolds number of about 7×10^4. The simulation was performed using the Transitional SST turbulence model and near wall treatment. The transitional model was selected since the flow at the leading edge of the blade was assumed to be laminar and then transitioned to turbulent as it flowed along the airfoil. For an explanation of the Transitional SST model and the near wall treatment see reference [46]. Figure 5.26 shows reverse flow on the upper surface of the airfoil. The area of reverse flow is believed to be a laminar separation bubble since the flow re-attaches further downstream on the airfoil. This supports the hypothesis of LSB causing the lower C_p values seen experimentally.

In order to have the experimental data properly model the flow around a full size turbine, the turbine blade used in the experiments is going to be changed to an airfoil that operates better at low Reynolds numbers and produces the same C_p as the full size turbine. Since the experiments will have the same C_p as a full size turbine, the simulations in this section of the thesis can be performed using the same C_L and C_D look-up table used in the previous sections.

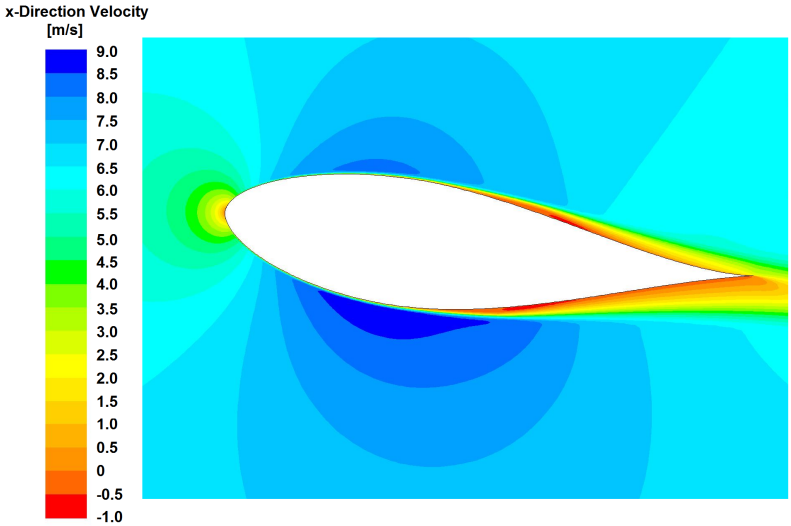

Figure 5.26: x-velocity contours for flow around an airfoil at a Reynolds number of 7×10^4 and an angle of attack of 8.7°.

5.5.2 Simulation Parameters

Table 5.5 shows the list of parameters for the experiments that are to be performed with the new airfoil. The experiments will be performed in two different water flumes, one at the University of Washington (UW) and the other at the Bamfield Marine Sciences Centre in British Columbia. The UW flume is about 0.6m deep and can operate at a velocity of 0.6 m/s. The Bamfield flume is about 0.9m deep and can operate at a velocity of either 0.6m/s or 1.2m/s. Two turbines of different diameters, 0.3m and 0.45m, have been constructed for the experiments.

It proved challenging to duplicate the experiments exactly using numerical simulations. Specifically, simulation runs with an inlet velocity less than 1m/s did not converge, so an alternative method was needed. The experimental parameters were non-dimensionalized into; the Tip Speed Ratio (TSR), Reynolds number (Re), channel Froude number (Fr_c), Froude number based on turbine diameter (Fr_D), Blockage

Table 5.5: Experimental Parameters

Turbine Diameter	Parameter	UW Flume	Bamfield Flume
0.305m	Velocity [m/s]	0.6	0.6, 1.2
	Channel Depth [m]	0.610	0.914
	d_r	0.75	0.75, 2.25
	Reynolds numbers (Re)	180000	180000, 370000
	Channel Froude number (Fr_c)	0.25	0.20, 0.40
	Froude number based on Diameter (Fr_D)	0.35	0.35, 0.69
	Blockage Ratio (BR)	0.20	0.09
0.457m	Velocity [m/s]	0.6	0.6, 1.2
	Channel Depth [m]	0.610	0.914
	d_r	0.56, 0.75	0.56, 0.75
	Reynolds numbers (Re)	270000	270000, 550000
	Channel Froude number (Fr_c)	0.25	0.20, 0.40
	Froude number based on Diameter (Fr_D)	0.28	0.28, 0.57
	Blockage Ratio (BR)	0.44	0.20

Ratio (BR), and the hub depth to diameter ratio (d_r). Simulations were then performed using the experiments' non-dimensional numbers. The simulations used a 1m diameter turbine with an inlet flow of 1.77m/s. The Reynolds number was maintained by adjusting the simulation's viscosity, and the Froude numbers were maintained by adjusting the gravitational acceleration in the simulation. By using a 1m diameter turbine, the same meshing strategy used previously in this thesis could be applied. The simulations were solved using an iterative approach since the inlet velocity has been shown to change as the solution converges, especially at higher blockage ratios.

First, 1.77m/s was set as the inlet velocity magnitude, and the solution was allowed to converge. The velocity magnitude supplied to the inlet was then increased by the difference between 1.77m/s and the velocity at the inlet of the converged solution. This was done until the converged inlet velocity was within ± 0.01m/s of 1.77m/s, ensuring the turbine was operating at the desired TSR, Re, Fr_c and Fr_D. The TSR used in each simulation was the TSR that provided the maximum C_p for the simulation's blockage ratio, see Figure 5.23.

5.5.3 Free Surface Fluctuation Results

Figure 5.27a shows the free surface fluctuations of three different simulations performed with the same blockage ratio and the same non-dimensionalized depth. Each simulation had different Froude numbers and a different Reynolds number. Since the free stream velocity and the turbine diameter were the same in every simulation, the Froude numbers and the Reynolds number were adjusted by changing the simulation's gravitational acceleration term and the simulation's viscosity term. By examining the equation for conservation of momentum for open channel flows with a turbine, Equation 3.50, it can be seen that viscosity only affects the change in free surface height related to the friction on the bottom of the channel. Therefore, the change in height resulting from the energy extracted by the turbine is affected by the gravitational acceleration term, and hence the Froude number. The difference in the Froude number for each simulation is also responsible for the difference in stationary waves downstream of the turbine.

In Section 5.2, Fr_c was proven to have a negligible effect on the free surface drop across the turbine, whereas Fr_D was shown to have a substantial effect on the drop in free surface elevation. The theoretical predictions for the change in free surface height related to bottom friction and the force of the turbine on the flow are shown in Figure 5.27b. The simulations and the theoretical predictions have the same magnitude of elevation change. This suggests that the simulations' free surface behavior is realistic.

It should also be noted that both the theory and the simulations show that the drop in the free surface height across the turbine increases as Fr_D increases.

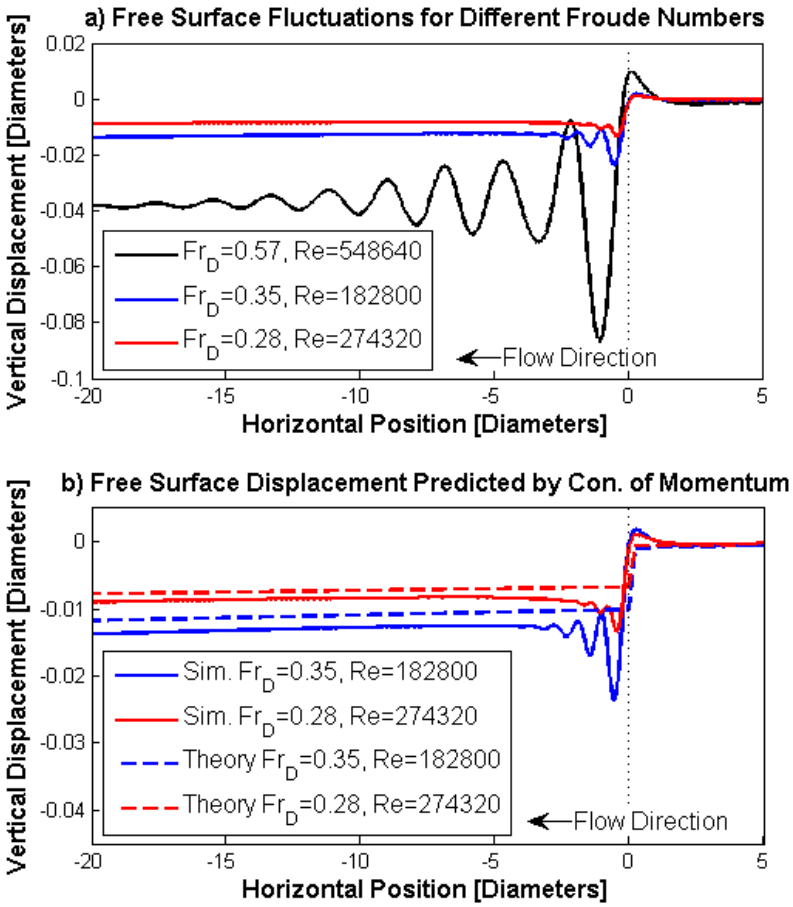

Figure 5.27: Free Surface Fluctuations for simulations with the same blockage ratio and depth to diameter ratio. The dashed lines represent the free surface fluctuations predicted using Equation 3.50.

Figure 5.28 shows the free surface fluctuations for three simulations with the same Fr_D and d_r, but different blockage ratios. The change in the free surface elevation across the turbine, shown in Figure 5.28, increases with an increase in blockage ratio

because more energy is extracted from the flow at higher blockage ratios.

The magnitude of the change in elevation across the turbine has been shown to depend on Fr_D, as well as the blockage ratio. The relative importance of each variable to the free surface elevation change can be seen by examining Figures 5.27 and 5.28. In Figure 5.27 the free surface fluctuations for the same blockage ratio are shown, and it can be seen that by doubling Fr_D the drop in free surface height quadruples. In Figure 5.28 the free surface fluctuations for a constant Fr_D are shown, and it can be seen that by doubling the blockage ratio the free surface drop approximately doubles. Therefore, Fr_D has more of an effect on the free surface drop across the turbine than the blockage ratio.

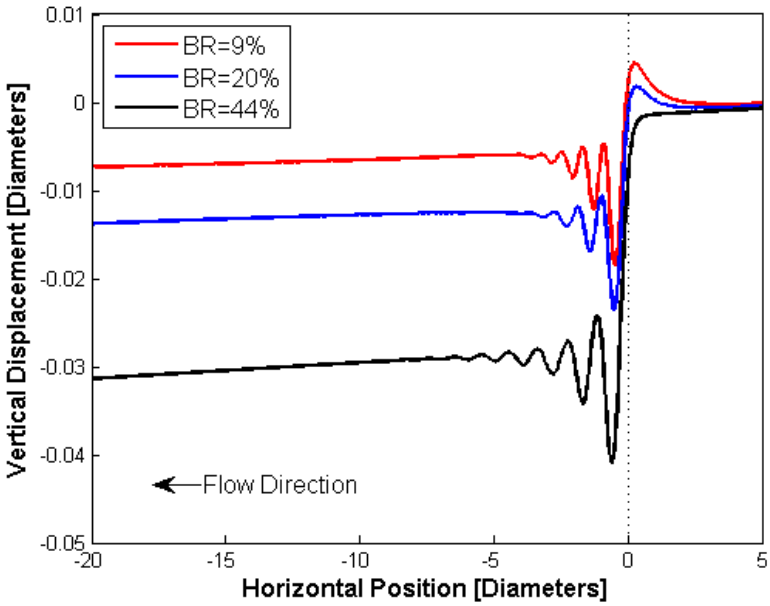

Figure 5.28: Free surface fluctuations for three simulations with the same Froude number, based on turbine diameter ($Fr_D = 0.35$), and the same non-dimensional turbine depth ($d_r = 0.75$)

The free surface fluctuations near the turbine for simulations with a d_r of 0.75 can be seen in Figure 5.29. The positions of both the first standing wave and the deformation in the free surface directly upstream of the turbine can be seen in Table 5.6. The following are general conclusions based on these results (d_r is held constant in these results):

- The deformation of the free surface directly upstream of the turbine increases with Fr_D.
- The horizontal location of the maximum height of the free surface deformation, upstream of the turbine, moves closer to the turbine's location as Fr_D increase.
- The depth of the standing wave downstream of the turbine increases with Fr_D.
- The horizontal position of the stationary wave moves further downstream from the turbine as Fr_D is increased.
- The wavelength between the trough of the first two waves increases with an increase in Fr_D.

The blockage ratio's effects on the stationary waves can be seen by comparing the simulations performed with a Fr_D of 0.35, see Figure 5.28. The free surface fluctuations from the three cases look very similar because they have the same Fr_D and the same d_r. However, since the free surface fluctuations are not identical it is reasonable to conclude that the blockage ratio also affects the free surface fluctuations near the turbine. The blockage ratio appears to have the following effects on the stationary waves downstream of the turbine:

- The first stationary wave increases in depth with the blockage ratio.

Table 5.6: Free Surface Fluctuations for a d_r of 0.75, see Figure 5.13

Fr_D	BR	Z_{min}	Y_{min}	λ	Z_{max}	Y_{max}
0.28	20	0.013	0.387	0.682	0.001	0.388
0.28	44	0.023	0.421	0.742	-	-
0.35	9	0.019	0.461	0.775	0.005	0.286
0.35	20	0.024	0.494	0.868	0.002	0.353
0.35	44	0.041	0.562	1.063	-	-
0.57	20	0.087	1.010	2.236	0.009	0.177
0.69	9	0.095	1.274	2.757	0.029	0

- The distance of the first wave trough from the turbine increases with the blockage ratio.

- The wavelength between the first wave and the second wave increases with the blockage ratio.

The blockage ratio also affects the deformation of the free surface directly upstream of the turbine such that higher blockage ratios result in smaller deformations upstream of the turbine. This is because the presence of the turbine in the channel results in a local Froude number based on an effective channel depth (the distance from the free surface to the tip of the turbine). The local Froude number increases with the blockage ratio because the flow speed around the turbine increases with the blockage ratio. At higher local Froude numbers, waves are unable to propagate upstream which is the reason why there is no free surface deformation upstream of the turbine for a blockage ratio of 44%, see Figure 5.28. The free surface deformation upstream of the turbine has also been shown to be affected by Fr_D such that the deformation increases as Fr_D increases. The simulation with a blockage ratio of 9%, a $Fr_D = 0.69$, and

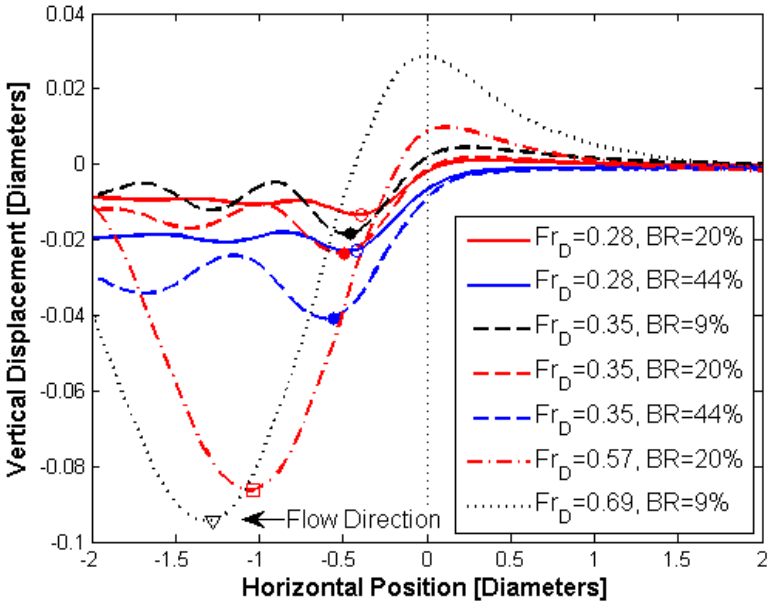

Figure 5.29: The position of the standing waves for simulations with a d_r of 0.75. The symbols represent the location of the maximum wave depth. - and $\circ$ represent a $Fr_D = 0.28$, - - and $\bullet$ represent a Fr_D of 0.35, $\cdot - \cdot$ and $\square$ represent a $Fr_D = 0.57$, and $\cdots$ and $\bigtriangledown$ represent a $Fr_D = 0.69$. The color black represents a blockage ratio of 9%, the color red represents a blockage ratio of 20%, and the color blue represents a blockage ratio of 44%.

a $d_r = 0.75$ has the highest local Froude number for all of the simulations (almost twice the local Froude number for the blockage ratio of 44%). Despite the high local Froude number there is a free surface deformation upstream of the turbine because Fr_D is very high counteracting the effects of the high local Froude number.

The relative importance of the blockage ratio's effects on the free surface fluctuations near the turbine are small when compared to Fr_D's effects, see Figure 5.29. For example, doubling the Fr_D increases the maximum wave depth by a factor of five, whereas doubling the blockage ratio does not even increase the depth by a factor of

two. Thus the Fr_D is more important to the free surface fluctuations near the turbine.

5.5.4 Coefficient of Power Results

Figures 5.30 and 5.31 show the C_p values for the different simulations performed in this section. The conclusions described below have been reached using the data from these figures, but it should be noted that the C_p may depend on multiple different parameters (e.g. Blockage Ratio, TSR, Fr_D, d_r, and Fr_c), thus analyzing the effects of parameters graphically is difficult especially since there have been a limited number of simulations preformed.

As predicted by theory, the coefficient of power increases with the increase in blockage ratio [1] [3]. All of the simulations performed with a blockage ratio of 9% produce approximately the same C_p, which in some cases is slightly higher than the C_p produced in the simulations without a free surface (the simulations used to obtain the TSR vs. C_p curves were performed without a free surface to save computational time). For the two simulations performed with a blockage ratio of 9% and a $Fr_D = 0.69$, the one with a d_r of 0.75 produced less power than the one with a d_r of 2.25. One possible explanation for the lower C_p value, is the increase in the free surface height just upstream of the turbine that occurs when the turbine is in close proximity to the free surface. This produces a larger cross sectional area near the turbine, which slightly decreases the velocity at the turbine leading to less power produced. The coefficients of power are calculated using the free stream velocity and do not account for the slower speed seen at the turbine in the case with a d_r of 0.75.

The coefficient of power is approximately the same for all simulations with a blockage ratio of 9%, and for all simulations with a blockage ratio of 20%, leading to the conclusion that for blockage ratios less than 20%, C_p is independent of Fr_D and Fr_c, see Figure 5.30 and Figure 5.31. Several theories predict that at higher blockage ratios C_p will increase with an increase in the channel Froude number [3]. Figure 5.31 does not show an increase in C_p related to the channel Froude number, for simulations

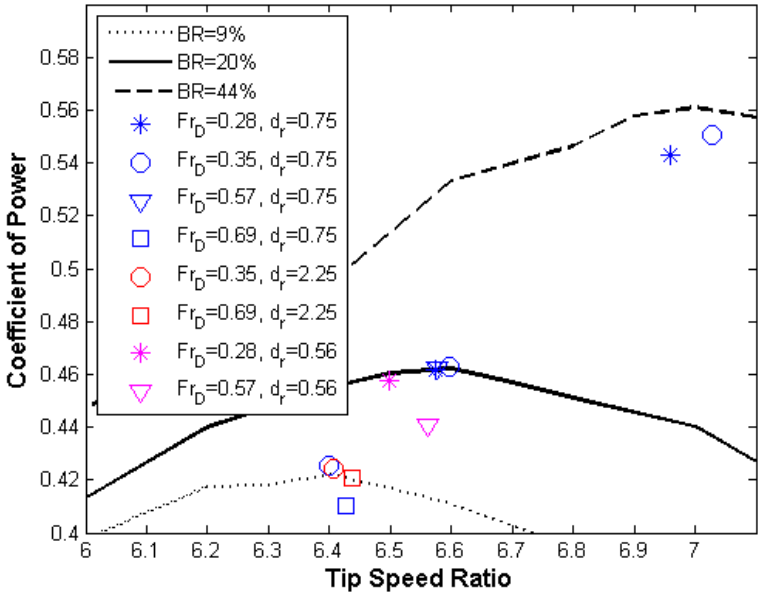

Figure 5.30: Coefficient of power for different blockage ratios and Froude numbers compared to TSR versus C_p curves. The color blue represents a d_r of 0.75, the color magenta represents a d_r of 0.56, and the color red represents a d_r of 2.25.

with a blockage ratio of 20%. However, for simulations performed with a blockage ratio of 44%, the C_p does appear to increase with an increase in Fr_D (and Fr_c), as predicted by the unidirectional flow theory. There are two potential reasons for the simulations with a blockage ratio of 20% not aligning with the theory. First, the free surface deformation upstream of the turbine affects C_p, and second, a change in the free surface height at the inlet slightly changes the blockage ratio, and hence the C_p. Neither of these reasons, however, are expected to have significant effects on the power produced.

As Fr_D increases for a given blockage ratio, the deformation in the free surface directly upstream of the turbine also increases. This results in an increase in the cross sectional area of the flow at the turbine, decreasing the average velocity at the turbine. Since

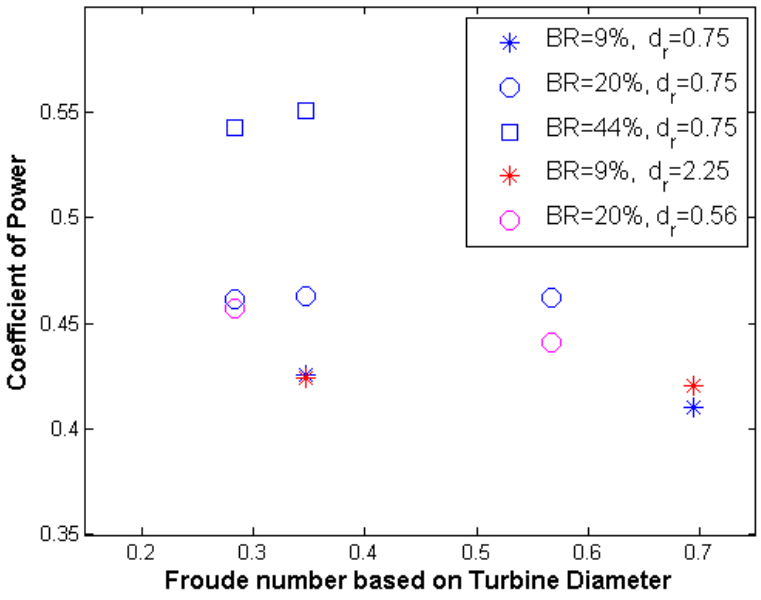

Figure 5.31: Coefficient of power for different blockage ratios and Froude numbers. The color blue represents a d_r of 0.75, the color magenta represents a d_r of 0.56, and the color red represents a d_r of 2.25.

the amount of power available in the flow is related to the velocity cubed, even a minimal change in velocity can result in a substantial decrease in power available. This results in a decrease in the power extracted from the flow and a decrease in C_p. Thus, some of the increase in C_p, related to Fr_c (predicted by Whelan's theory), is counteracted by the decrease in C_p, related to the free surface deformation upstream of the turbine.

At higher blockage ratios, such as 44%, the decrease in C_p related to the free surface deformation does not occur. The free surface deformation upstream of the turbine was shown to decrease as the blockage ratio increased. As a result, at higher blockage ratios (greater than 20%), the increase in C_p resulting from Fr_c cannot be counteracted by the increase in the free surface deformation upstream of the turbine. Thus

C_p becomes more dependent on Fr_c as the blockage ratio increases.

The fact that the C_p did not increase with Fr_D or Fr_c at lower blockage ratios also may be attributed to a change in the blockage ratio, however, it can be proven that this effect is very small. The blockage ratio is defined in Whelan's paper [3] as the area of the turbine divided by the upstream cross sectional area of the flow. In this thesis, the downstream cross sectional area was used because the downstream area was fixed by the simulation's boundary conditions and the upstream area was not, i.e. the inlet height was allowed to fluctuate but the outlet height was fixed. Since the free surface drop across the turbine increases as Fr_D increases, the height of the free surface at the inlet also had to increase, resulting in a decrease in the blockage ratio according to Whelan's definition. This results in a decrease in the C_p because C_p increases with the blockage ratio.

For smaller blockage ratios, the difference in the two definitions for the blockage ratio is very small or even negligible. Consider the simulations performed with a blockage ratio approximately equal to 20%. Using the downstream cross sectional area to compute the blockage ratios, the blockage ratios are 19.63% for simulations performed with $Fr_D = 0.57$ and $Fr_D = 0.28$. Using Whelan's definition, the blockage ratio for the simulation with a $Fr_D = 0.57$ is 19.25% and the blockage ratio for the simulation with a $Fr_D = 0.28$ is 19.54%. The difference in maximum C_p values related to the difference in these blockage ratios is very small. Therefore, for blockage ratios of approximately 20% or less, the change in the blockage ratio resulting from the increase in free surface height at the inlet caused by Fr_D is assumed to be negligible, but may have slightly decreased the C_p for the large values of Fr_D.

For higher blockage ratios, the increase in free surface height at the inlet has a more significant effect on the blockage ratio. For example, for simulations performed with a blockage ratio of approximately 44% and $Fr_D = 0.35$, the blockage ratio calculated using the downstream area is 43.74%, whereas the blockage ratio calculated using the upstream cross sectional area is 42.78%. Figure 5.32 shows the change in C_p related

to changing the blockage ratio from 43.74% to 42.78%, in simulations without a free surface. The difference in blockage ratio produced a measurable but insignificant difference in C_p. Figure 5.30 shows that for blockage ratios of 44% the C_p values found in simulations with a free surface are less than simulations without a free surface (the TSR versus C_p curve). The change in the blockage ratio caused by the increase in inlet height is partially responsible for this difference.

The other reason the C_p is lower than the TSR versus C_p curve is that the curve was created with the turbine centered in the channel (the hub was approximately 0.67D away from the channel bottom), whereas to obtain a $d_r = 0.75$ in the simulations with a free surface the turbine had to be moved closer to the channel floor (the hub was approximately 0.59D away from the channel floor). The no slip boundary condition applied to the channel bottom causes a velocity gradient in the lower portion of the channel. As a result, since the turbine was closer to the bottom in the simulations with a free surface, the flow speeds through the turbine were lower, so the power produced and the C_p values were lower, see Figure 5.32.

The velocity profile near the bottom of the channel is affected by the Reynolds number. This results in turbines at the same hub depth being exposed to different velocities depending on the Reynolds number. Thus, for turbines in close proximity to the bottom of the channel, the C_p is also affected by the Reynolds number, which is part of the reason why the simulation with $Fr_D = 0.35$ has a higher C_p than the simulation with $Fr_D = 0.28$. Figure 5.32 shows for a constant blockage ratio and a constant turbine depth, C_p changes depending on the Reynolds number.

Figure 5.33 shows the C_p values predicted by Whelan's theory [3] for the different experiments in Table 5.5, as well as the C_p values predicted by Garrett's theory [1]. The increase in C_p related to the blockage ratio can be seen in both of the theories and the numerical simulation results. However, the magnitude of C_p and the amount C_p increases due to blockage ratio is substantially smaller for the numerical simulations. At higher blockage ratios, like 44%, the simulations showed that the C_p increased

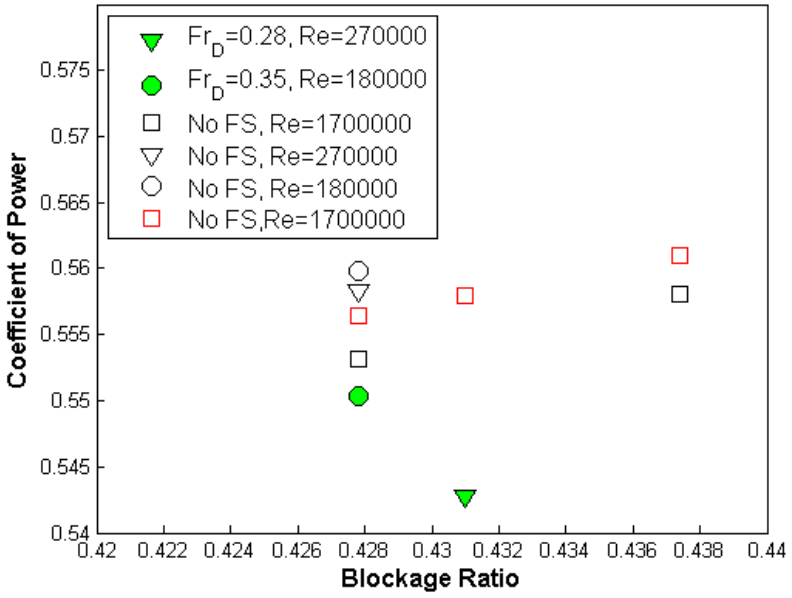

Figure 5.32: Coefficient of power for different blockage ratios. Symbols shaded green represent simulations with a free surface, symbols shaded white represent simulations without a free surface, the color black represents a non-dimensional hub depth (d_r) of 0.75D, and the color red represents a non-dimensional hub depth (d_r) of 0.67D.

with Fr_c as predicted by theory, but not to the extent predicted.

One of the reasons the C_p from the simulations does not match the C_p predicted by Garrett's and Whelan's theory is the turbines in the theory are operating with a different axial induction factor than the turbines in the simulations. The theoretical C_p values shown in Figure 5.33 were computed using the optimum axial induction factor. The optimum axial induction factor is the axial induction factor that corresponds to the maximum possible coefficient of power. For a turbine operating in a channel with a blockage ratio of 0, the optimum axial induction factor is 1/3 with C_p equaling the Betz's limit. Figure 2.1 shows that as the blockage ratio increases the optimum axial induction factor also increases. Figure 5.34 shows the axial induction factor of

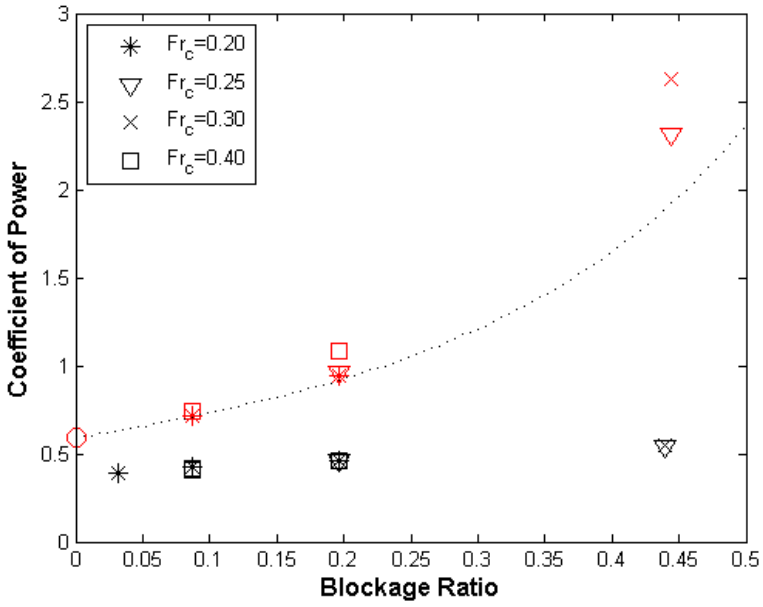

Figure 5.33: Coefficient of power for different blockage ratios and channel Froude numbers. The color black represents the C_p from the numerical simulations. The color red represents the C_p predicted by Whelan's Theory [3]. The dashed line represents the C_p calculated using Garrett's Theory [1]. ∘ represents the Betz limit.

the turbines in the simulations and their respective C_p values. It is obvious that the simulations are not operating at the optimum axial induction factor for their specific blockage ratios because all of the axial induction factors are less than 0.2. In fact, for the simulations, the axial induction factor decreased as the blockage ratios increased. This is because at high blockage ratios there is less area around the turbine for flow to be diverted leading to a larger flow rate through the turbine and a lower axial induction factor.

Figure 5.34 shows the axial induction factor versus C_p curves predicted by Whelan's theory. By comparing the theory's predicted values for C_p at the axial induction factors found for the turbines in this thesis's simulations, instead of the optimum

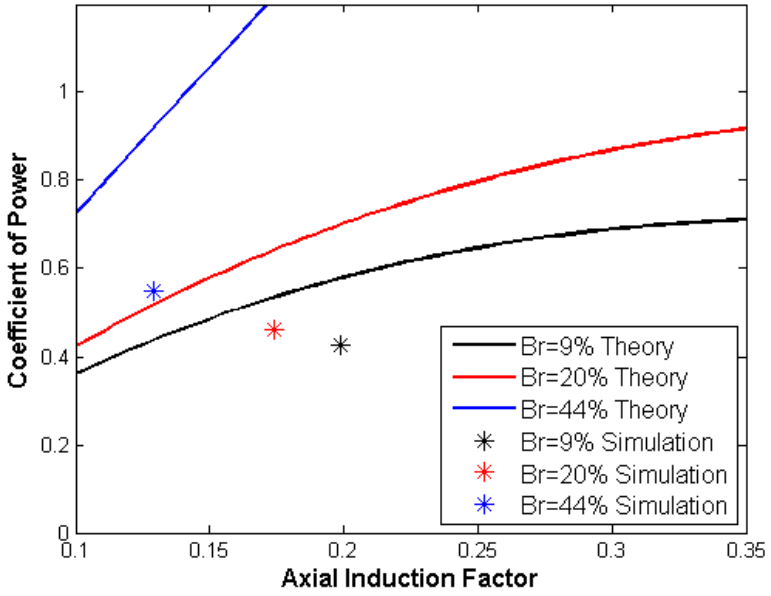

Figure 5.34: Coefficient of power versus axial induction factor for different blockage ratios with a $Fr_D = 0.35$ and $d_r = 0.75$.

axial induction factors, it can be seen that the simulations' C_p values are about 70% of the value predicted using Whelan's theory. When Whelan compared the theory to two sets of experiments, the experimental C_p values were about 60% of the C_p values predicted by theory [3]. Therefore it appears that the simulations of this thesis are producing reasonable results.

For a blockage ratio of 44%, the numerical simulation's C_p values were only 60% of the theoretical C_p values. One issue that maybe enhancing the difference between simulated and theoretical C_p values at high blockage ratios is the theory assumes subcritical flow [26]. The simulations show that for the blockage ratio of 44%, the flow is supercritical near the turbine, so the theory may not be accurately representing the flow, leading to inaccurate predictions of C_p. Furthermore, the theory is developed assuming the flow is only in the streamwise direction, but at high blockage ratios the

flow becomes more three-dimensional deviating from the assumptions of the theory. These issues explain the larger difference in C_p values for the blockage ratio of 44%. The maximum C_p values predicted by Garrett's and Whelan's theory for the optimum axial induction factor are significantly higher than the C_p values found in the numerical simulations, see Figure 5.33. The simulations were performed using the TSR that produced the maximum coefficient of power because the TSR is one of the operating parameter used by real turbines to adjust power, not the axial induction factor. By changing the blade's pitch and twist, the optimal TSR can be increased helping MHK turbines to reach higher axial induction factors and possibly increase their maximum C_p values. Furthermore, increasing the number of turbine blades can help increase the axial induction factor of the turbine such that it could have a higher maximum C_p. However, both of these suggestions involve designing turbines specifically for certain flows instead of designing a turbine that can be applied universally.

It is important to understand that real turbines typically do not operate with the ideal parameters used by theory to predict the maximum C_p, so real turbines will not produce the same C_p. Therefore, caution must be used when applying theory because it can significantly over predict C_p when unrealistic, yet ideal, conditions are used, giving a false understanding of the amount of power that can be produced in reality.

Chapter 6

SUMMARY, CONCLUSIONS, AND FUTURE WORK

MHK turbines are a promising new technology for energy production that relies on converting energy from tidal currents into electricity. Wind turbines and MHK turbines have numerous similarities and as such many of the same models and theories that have been applied for decades to wind energy can now be applied to tidal energy. However, there are a few key differences between wind energy and tidal energy that can affect the operating characteristics of a turbine. This thesis specifically examines one of these key differences: the effect of the presence of a free surface on the operating characteristics of a horizontal axis MHK turbine. Associated with the presence of a free surface, although independent from it, is the concept of blockage ratio: the ratio of cross sectional area swept by the turbine rotor to the total cross sectional area in the channel; this is another key parameter for MHK turbines that is studied in depth in this thesis.

The presence of a free surface creates higher blockage ratios for MHK turbines than for wind turbines. In many cases this negates the application of the Betz limit because the Betz limit assumes negligible blockage ratio. According to theoretical analyses performed by Garrett [1], Whelan [3], and Polagye [26] increasing the blockage ratio increases the maximum possible coefficient of power for a turbine. These are simple one-dimensional models, therefore, it is important to determine, from fully three dimensional turbulent flow with a realistic representation of the MHK turbine, the extend of the effect that blockage ratio has on the power produced by a turbine.

Another effect the free surface has on MHK turbines is it constrains the turbine's wake expansion creating an asymmetric wake. Since in turbine arrays the wake of

one turbine is the inflow conditions for another turbine it is important to understand the affects of the free surface on the wake, to ensure optimal turbine array designs.

6.1 Summary of Numerical Methodology

The computational simulation of MHK turbines in an open channel requires a number of sophisticated models for the turbulent flow, the turbine implementation and the tracking of the free surface. Additionally, it is important to carefully construct the computational mesh to treat every aspect of the simulation with accuracy and stability. Finally, the selection of adequate boundary conditions is not trivial and can significantly affect the results.

In the simulations included in this thesis that study the flow around an MHK turbine in the presence of a free surface, the mesh had to be refined near the air-water interface in order to capture the free surface height and fluctuations. The mesh also had to be refined in the wake region to ensure the evolution of the wake was properly modeled. An unstructured mesh was used to transition from critical regions in the domain, where a fine mesh was necessary, to regions with low gradients, near the inlet and towards the sides and outlet of the domain, where a coarse mesh was acceptable, in order to minimize the number of mesh elements.

The Virtual Blade Model (VBM) was used in the numerical simulations to implement the presence of the turbine rotor blades in the equations of motion. VBM was selected because it models the time-averaged aerodynamic effect of rotating blades using values for the coefficients of lift and drag developed by a higher accuracy model, while not requiring the blade geometry to be meshed. This saves computational time, because VBM requires less mesh elements than moving reference frame or moving mesh simulations that model the actual blade geometry, and the solution is steady state since the effect of the blades is time-averaged.

The Volume of Fluid (VOF) model was used in the numerical simulations to model the two fluids, water and air, and to track the free surface. VOF was used because

it is less computationally expensive than other multiphase models and more stable in cases that do not require a sharp interface to be tracked. VOF requires the solution of a continuity equation for each fluid and a single momentum equation. A series of simulations were performed to determine the correct boundary conditions to use in this problem. Results from different boundary conditions (mass flow rate, fixed pressure, fixed free surface height) at the inlet and outlet were compared to the free surface profile predicted by theory. Typical boundary conditions were applied at the channel side walls: no slip for the bottom, symmetry for the top and sides. Pressure Inlet with the Open Channel Flow Option for the inlet, and Pressure Outlet with the Open Channel Flow Option for the outlet produced the most accurate free surface profile and was used in all the numerical simulations in this thesis. The pressure specification method applied to the outlet was a user-prescribed free surface height and bottom height.

6.2 Summary of the Interactions Between the Free Surface and a Horizontal Axis Turbine at Low Blockage Ratios

When a turbine is in close proximity to the free surface, the wake will expand to interact with the surface. It was previously believed [18] that the wake of a turbine close to the free surface will recover in a shorter distance than the wake of a turbine far away from the free surface. This incorrect statement was arrived at by examining the downstream centerline velocity measurements. However, the velocity minimum in the wake of a turbine close to the free surface does not occur at the turbine's centerline. By examining the minimum velocity in the turbine's wake, we found that the wake actually recovers slower for turbines close to the free surface. The recovery is slower because the wake is not exposed to the same mixing with high momentum fluid and the current's high momentum fluid surrounding the wake is responsible for wake recovery.

It was also observed that the total drop in free surface height across a channel re-

mained constant for simulations performed in the same channel with the same turbine, regardless of the turbine's vertical position. This was because the power extracted by the turbine and the friction factor were independent of the vertical position of the turbine. The free surface fluctuations near the location of the turbine rotor, however, did depend strongly on the depth of the turbine.

6.3 Summary of the Non-Dimensional Numbers used to Characterize the Effects of a MHK Turbine on the Free Surface

The Froude number is the non-dimensional number most often used to analyze flows with a free surface. For open channel flows without a MHK turbine the characteristic length scale used in the Froude number is the channel depth. By comparing the free surface fluctuations from simulations with different channel depths (and associated different channel Froude number values), it was concluded that the free surface fluctuations do not depend on channel depth, for values of Fr below 0.5 and blockage ratios below 0.2. Therefore, for open channel flows with a MHK turbine, the channel Froude number is irrelevant to the flow and the MHK turbine performance for realistic values away from the most extreme conditions for shallow channel depth and blockage ratios.

Several other length scales were examined as critical parameters for controlling the behavior of the flow. Two relevant length scales are the turbine's tip depth and the turbine's hub depth. Neither length scale provided the a complete characterization of the free surface fluctuations (through the depth-based Froude number) because neither scale accounted for the size of the turbine. The turbine diameter was then applied as the length scale, but the free surface fluctuation appeared to also depend on the turbine's depth. The application of two non-dimensional numbers was the solution. One non-dimensional number was the Froude number with a characteristic length of the turbine diameter (Fr_D), and the other was a non-dimensional depth equal to the hub depth divided by the turbine diameter (d_r). When simulations had

the same Froude number based on turbine diameter and the same depth ratio, the free surface shape downstream of the turbine was identical.

The free surface waves may affect objects downstream of the turbine so it is important to understand how waves respond to changes in the flow non-dimensional parameters: waves increased in magnitude as Fr_D increased and as d_r decreased; the distance downstream to the first wave trough (wavelength) increased with increases in Fr_D but decreased with increases in d_r.

6.4 Summary of the Effects of the Free Surface on the Coefficient of Power at Low Blockage Ratios

The coefficient of power (C_p) at low blockage ratios was not affected by the vertical position of the turbine or by the channel depth. The wake resolution, however, affected the power extracted by the turbine so it was important to use an adequate mesh in the turbine wake when comparing different size turbines. Special care was taken to use the same size mesh cells near the free surface regardless of the turbine diameter because the resolution of the free surface fluctuations required sufficient resolution in the mesh near the free surface.

6.5 Summary of the Blockage Ratio Effects on MHK Turbine Performance

Preliminary simulations performed at different blockage ratios showed C_p increased with the blockage ratio. It was also proven that as the blockage ratio increased the value of TSR ratio for optimum C_p increased. Higher blockage ratios lead to a higher velocity through the turbine, which decreases the actual TSR subsequently decreasing C_p since C_p is related to the actual TSR. The actual TSR is the TSR based on the velocity at the turbine rotor plane (rather than based on the free stream velocity as it is usually defined). New TSR versus C_P curves were created to determine the TSR based on the free stream velocity that produced the maximum C_p for each blockage

ratio. The free stream velocity was used to calculate the TSR-case-label because it is known prior to the performance of the simulation.

6.6 Summary of the Numerical Simulations of Experiments Performed with Scaled Turbines

A set of simulations were performed to model experiments of scaled MHK turbines. The experiments will be performed using two different flumes to provide different blockage ratios. The simulations will be compared against the experimental data, to provide experimental validation for the conclusions of this thesis.

The simulations were performed using a 1m diameter turbine used in the other simulations of this thesis. This allowed us to leverage the computational simulation effort developed in the first part of the thesis, without the need to repeat the mesh creation for different domains. All the simulations were performed matching the non-dimensional numbers in the experiments. The gravitational acceleration and the fluid viscosity were changed to explore the relevant range of non-dimensional parameters with the different simulations.

The drop in the free surface height across the turbine was determined to be related to the blockage ratio as well as the Turbine Froude number (Fr_D). If either the blockage ratio or Fr_D was increased, the drop in free surface height across the turbine would increase but for different reasons. At higher blockage ratios the drop increased because more power was extracted from the flow, whereas, an increase in Fr_D lowered the effective gravity (lowering gravity is equivalent to increasing the Fr_D since all simulations were performed with the same diameter turbine at the same flow speed) which increased the elevation change across the turbine as predicted by theory.

The free surface waves downstream of the turbine were also shown to be affected by the blockage ratio and Fr_D. For larger blockage ratios the first wave trough moved further downstream from the turbine and the wave depth increased. The effects of Fr_D on the surface waves, found for low blockage ratios, were verified at higher

blockage ratios: increasing Fr_D increased the wave depth, the wave length, and the distance downstream where the first wave trough occurred.

The free surface deformation upstream of the turbine was shown to be dependent on Fr_D, d_r and the blockage ratio. The deformation increased for larger turbine rotor diameter (Fr_D), and decreased with an increase in blockage ratio and turbine depth (d_r). The free surface deformation decreased with blockage ratio because at higher blockage ratios there is less area around the turbine for the flow to be diverted resulting in a higher velocity around the turbine than that seen at low blockage ratios. When high blockage ratio values, such as 44%, the flow near the turbine becomes locally supercritical and free surface gravity waves cannot travel upstream of the turbine. Thus, the free surface upstream of the turbine is not deformed.

The rise in the free surface directly upstream of the turbine related to Fr_D and d_r had a small effect on the power extraction (C_p). The free surface deformation resulted in a larger cross sectional area of the flow at the turbine which slightly decreased the velocity through the turbine. Since the power available in the flow is proportional to the velocity cubed, even a slight change in the velocity at the rotor disk can result in a appreciable change in the power extracted. Therefore, less power was extracted from flows with a large free surface rise just upstream of the turbine.

Several papers have suggested that, at high blockage ratios, increasing the channel Froude number (Fr_c) will increase C_p. The results of this thesis, however, do not support that conclusion for blockage ratios less than 20%. Any increase in C_p related to an increase in Fr_c was counteracted by the decrease in C_p related to the rise in the free surface directly upstream of the turbine. At higher blockage ratios, such as 44%, there was no deformation upstream of the turbine so C_p did increase slightly with Fr_c. However, the increase in C_p due to Fr_c was much less pronounced than predicted by theory.

6.7 General Conclusions

The purpose of this thesis was to determine under which conditions it is necessary to include the free surface in numerical simulations of MHK turbines. There are generally two reasons for simulating MHK turbines: one is to examine the turbine's wake and the second is to examine the coefficient of power. Since the presence of a free surface affects each differently, the analysis of the free surface in MHK turbine simulations will be discussed based on the goal of the simulation.

The free surface was shown to affect the wake evolution downstream of the turbine when the turbine had a hub depth to diameter ratio of less than 1.5. Therefore, if the wake characteristics are the focus of a study, such as for array optimization, including the free surface in the numerical simulations will improve the physical representation of the flow and the validity of the results. This will ensure more realistic inflow conditions for downstream turbines in the array. The free surface fluctuations may also play an important role in turbine array design. As Fr_D is increased or d_r is decreased, the depth of the free surface waves downstream of the turbines increases. The wave depth increased to as much as 0.1 rotor diameters for the case of $Fr_D = 0.69$ and $d_r = 0.75$. Since the waves extend downstream of the turbine, any turbine placed downstream of the first rows of turbines in an array may experience the effects of the free surface fluctuations. This could affect the downstream turbine's wake as well as it's coefficient of power and increase the variable loading on the downstream turbines. Therefore, when studying turbine arrays where the turbines are in close proximity to the free surface, the free surface should be included in the simulations.

For single turbines (not in an array), the coefficient of power for blockage ratios of 20% or less have been shown to be independent of or negligibly dependent on Fr_D, Fr_c, and d_r. For blockage ratios greater than 20% the coefficient of power was shown to vary only slightly with the channel Froude number, and the increase in C_p may be neglected in most cases.

The coefficient of power was shown to be heavily dependent on the blockage ratio. Therefore, when simulations are performed to study the coefficient of power, it is not necessary to include the free surface as long as the simulations are performed with the correct blockage ratio. The only exception to this conclusion is for turbines used to hydraulically control a channel, because the range of blockage ratios and Froude numbers used in those cases are very extreme, and outside the conditions studied in this thesis [55].

Performing simulations without a free surface represent significantly reduced computational requirements. Simulations without a free surface require less mesh elements, converge at lower number of iterations, and the inlet boundary condition's are easier to establish. Thus, simulations without a free surface have a much shorter computational time, require less memory allocation and less operator time in meshing and setting up the simulations. A simulation was performed with and without a free surface to determine the computational expense of including a free surface. The simulation with a free surface took nine times longer to converge than the simulation without the free surface. Therefore, simulations should only be performed with a free surface when it is essential to closely represent the free surface effects in the problem under study, such as when information is required about the details of the wake or when the free surface height may affect other turbines or topography in the vicinity.

6.8 Future Work

The numerical simulations of MHK turbine experiments must be validated using experimental data, to ensure the coefficient of power as well as free surface fluctuations found numerically are accurate. Once the simulations are validated, the same methodology used in this thesis can be applied to the study of an array of horizontal axis turbines in order to determine if the free surface fluctuations from an upstream turbine will significantly affect the operating characteristics of downstream turbines. For any continuing research on the free surface effects on MHK turbines at high

blockage ratios it would be beneficial to develop a new set of boundary conditions. The new inlet boundary condition should allow the user to fix the inlet velocity of the water and fix the inlet free surface height. Since the inlet height is fixed, the new outlet boundary condition must allow the outlet height to fluctuate, in order to account for the energy extracted by the turbine and the energy loss due to the friction on the bottom of the channel. New boundary conditions similar to these will ensure the numerical model is describing the desired flow, i.e. has the correct inlet velocity and the correct blockage ratio.

BIBLIOGRAPHY

[1] C. Garrett and P. Cummins. The efficiency of a turbine in a tidal channel. *J. Fluid Mechanics*, 588:243–251, 2007.

[2] M. R. Ruith. Unstructured, multiplex rotor source model with thrust and moment trimming- fluent's vbm model. Technical report, Fluent Inc., 2005.

[3] J. I. Whelan, J. M. R. Graham, and J. Perio. A free-surface and blockage correction for tidal turbines. *J. Fluid Mechanics*, 624:281–291, 2009.

[4] 2009 energy enpenditure per person, 2012. URL http://energy.gov/maps/2009-energy-expenditure-person.

[5] United States Census Bureau. The 2012 statistical abstract: Energy and utilities, 2012. URL http://www.census.gov/prod/2011pubs/12statab/energy.pdf.

[6] Energy Information Administration. Annual energy review 2011, September 2012 2012. URL http://www.eia.gov/totalenergy/data/annual/pdf/aer.pdf.

[7] S. E. Ben Elghali, M. E. H. Bendouzid, and J. F. Charpentier. Marine tidal current electric power generation technology: State of the art and current status. *Electric Machines & Drives Conference*, 2:1407–1412, 2007.

[8] B. Polagye, B. Van Cleve, A. Copping, and K. Kirkendall, editors. *Environmental Effects of Tidal Energy Development*, number NMFS F/SPO-116, 186 p. in U.S. Dept. Commerce, NOAA Tech. Memo., 2010.

[9] T. J. Hall. Numerical simulation of a cross flow marine hydrokinetic turbine. Master's thesis, University of Washington, 2012.

[10] G. Hagerman, B. Polagye, R. Bedard, and M. Previsic. Methodology for estimating tidal current energy resources and power production by tidal in-stream energy conversion (tisec) devices. Technical report, Electric Power Research Institute Inc. (EPRI), 2006.

[11] I. G Bryden, S. J Couch, A. Owen, and G. Melville. Tidal current resource assessment. *Proceedings of the Institution of Mechanical Engineers. Part A, Journal of Power and Energy*, 221:125–135, 2007.

[12] S. Antheaume, T. Maitre, and J. Achard. Hydraulic darrieus turbines effieciency for free fluid flow conditions versus power farms conditions. *Renewable Energy*, 33:2186–2198, 2008.

[13] Marine current turbines. URL http://www.marineturbines.com/.

[14] F. O Rourke, F. Boyle, and A. Reynolds. Tidal energy update 2009. *Applied Energy*, 87:398–409, 2010.

[15] Open hydro tidal technology. URL http://www.openhydro.com/company.html.

[16] Andritz hydro hammerfest. URL http://www.hammerfeststrom.com/.

[17] Ocean renewable power company. URL http://www.orpc.co/default.aspx.

[18] X. Sun. *Numerical and Experimental Investigation of Tidal Current Energy Extraction*. PhD thesis, The University of Edinburgh, 2008.

[19] X. Sun, J. P. Chick, and I. G. Bryden. Laboratory-scale simulation of energy extraction from tidal currents. *Renewable Energy*, 33:1267–1274, 2008.

[20] F. M. White. *Fluid Mechanics*. McGraw-Hill, 7th edition, 2011.

[21] L. E. Myers, A. S. Bahaj, R. I. Rawlinson-Smith, and Thomson M. The effect of boundary proximity upon the wake structure of horizontal axis marine current turbines. In *Proceeding of the 27th International Conference on Offshore Mechanics and Artic Engineering*, 2008.

[22] A. S. Bahaj, L. E. Myers, R. I. Rawlinson-Smith, and M. Thomson. The effects of boundary proximity upon the wake structure of horizontal axis marine current turbines. *Journal of Offshore Mechanics and Arctic Engineering*, 134:021104:1–8, 2012.

[23] L. E. Myers and A. S. Bahaj. Experimental analysis of the flow field around horizontal axis tidal turbines by use of scale mesh disk rotor simulators. *Ocean Engineering*, 37:218–227, 2010.

[24] A. Betz. Das maximum der theoretisch moglichen ausnutzung des wiwind durch windmortoren. *Z. Gesante Turbinenwesen*, 26:307–309, 1920.

[25] T. Burton, D. Sharpe, N. Jenkins, and E. Bossanyi. *Wind Energy Handbook*. John Wiley & Sons, Ltd, 2001.

[26] B. Polagye. *Hydrodynamic Effects of Kinetic Power Extraction by In-Stream Tidal Turbines*. PhD thesis, University of Washington, 2009.

[27] T Javaherchi. Numerical modeling of tidal turbines: Methodology development and potential physical environmental effects. Master's thesis, University of Washington, 2010.

[28] M. E. Harrison, W. M. J. Batten, L. E. Myers, and A. S. Bahaj. A comparison between cfd simulations and experiments for predicting the far wake of horizontal axis tidal turbine. In *Proceeding of the 8th European Wave and Tidal Energy Conference*, 2009.

[29] M. E. Harrison, W. M. J. Batten, L. E. Myers, and A. S. Bahaj. Comparison between cfd simulations and experiments for predicting the far wake of horizontal axis tidal turbines. *IET Renewable Power Generation*, 4-6:613–627, 2010.

[30] *ANSYS FLUENT 14.0 User's Guide, Chapter 7 Cell Zone and Boundary Conditions, Section 7.2.3, Porous Media Conditions and Section 7.3.2. Using Flow Boundary Conditions*, 2011.

[31] A. S. Bahaj, W. M. J. Batten, and G. McCann. Experimental verifications of numberical predictions for the hydrodynamic performance of horizontal axis marine current turbines. *Renewable Energy*, 32:2479–2490, 2007.

[32] S. R. Turnock, A. B. Phillips, J. Banks, and R. Nicholls-Lee. Modelling tidal current turbine wakes using a coupled rans-bemt approach as a tool for analysing power capture of arrays of turbines. *Ocean Engineering*, 38:1300–1307, 2011.

[33] W. M. J. Batten, A. S. Bahaj, A. F. Molland, and J. R. Chaplin. Experimental validated numerical method for the hydrodynamic design of horizontal axis tidal turbines. *Ocean Engineering*, 34:1013–1020, 2007.

[34] A. S. Bahaj, A. F. Molland, J. R. Chaplin, and W. M. J. Batten. Power and thrust measurements of marine current turbines under various hydrodynamic flow conditions in a cavitation tunnel and a towing tank. *Renewable Energy*, 32: 407–426, 2007.

[35] A. S. Bahaj, Thomson M. Myers, L. E., and N. Jorge. Characterising the wake of horizontal axis marine current turbines. In *Proceedings of the 7th European Wave and Tidal Energy Conference Porto, Portugal*, 2007.

[36] A. J. Macleod, S. Barnes, K. G. Rados, and I. G. Bryden. Wake effects in tidal current farms. In *Proceedings of the international conference on marine renewable energy, Newcastle upon Tyne, UK*, 2002.

[37] C. A. Consul, H. J. Wilden, and S. C. McIntosh. Blockage effects on the hydrodynamic performance of a marine cross-flow turbine. *Philosophical Transactions of the Royal Society A*, 371:1–16, 2013.

[38] H. K. Versteeg and W Malalasekera. *An Introduction to Computational Fluid Dynamics- The Finite Volume Method*. Pearson Education Limited, 2007.

[39] S. B. Pope. *Turbulent Flows*. Cambridge University Press, 2000.

[40] A. Gosset and G. Flouriot. Optimization of power extraction in an array of marine hydrokinetic turbines. Technical report, French Naval Academy, 2008.

[41] *ANSYS FLUENT Theory Guide Release 14.0, Chapter 17, Section 17.3*, November 2011.

[42] C. W. Hirt and B. D. Nichols. Volume of fluid (vof) method for the dynamics of free boundaries. *Journal of Computational Physics*, 39:201–225, 1981.

[43] *ANSYS FLUENT 14.0 User's Guide, Chapter 26, Modeling Multiphase Flows*, 2011.

[44] M. J. Lawson, Y. Li, and D. C. Sale. Development and verification of a computational fluid dynamics model of a horizontal-axis tidal current turbine. In *Proceedings of the 30th International Conference on Ocean, Offshore and Arctic Engineering*, 2011.

[45] M. Tessier and N. Tomasini. Numerical study of horizontal axis hydrokinetic turbines: Performance analysis and array optimization. Technical report, French Naval Academy in Collaboration with University of Washington, 2012.

[46] *ANSYS FLUENT Theory Guide Release 14.0, Chapter 4, Turbulence*, November 2011.

[47] J. Thomson, B. Polagye, V. Durgesh, and M. Richmond. Measurements of turbulence at two tidal energy sites in puget sound, wa. *IEEE Journal of Oceanic Engineering*, 37:363–374, 2012.

[48] *ANSYS FLUENT 14.0 User's Guide, Chapter 29, Modeling Using the Solver*, 2011.

[49] K. A. Haas, H. M. Fritz, S. P. French, B. T. Smith, and V. Neary. Assessment of energy production potential from tidal streams in the united states. Technical report, Georgia Tech Research Corporation, 2011.

[50] News lincoln county: Toledo man resues woman from car after it plunged into yaquina river off highway 20, December 2012. URL http://www.newslincolncounty.com/?cat=63.

[51] Q. Zhu, Y. Liu, and D. K. P. Yue. Numerical investigation of free-surface signatures generated by submerged objects. 2006.

[52] P. K Kundu and I. M. Cohen. *Fluid Mechanics*. Academic Press, 2008.

[53] J. I. Whelan and T. Stallard. Arguments for modifying the geometry of a scale model rotor. In *9th European Wave and Tidal Energy Conference*, 2011.

[54] E. J. Schroeder. Low reynolds number flow validation using computational fluid dynamcis with application to micro air vehcles. Master's thesis, University of Maryland, 2005.

[55] A. Hoseyni Chime. Analysis of hydrokinetic turbines in open channel flows. Master's thesis, University of Washington, 2013.

[56] Energy Information Administration. Greenhouse gases, climate change, and energy, April 2004. URL http://www.eia.gov/oiaf/1605/ggccebro/chapter1.html.